UNIVERSITAT
ROVIRA I VIRGILI

Universitat Rovira i Virgili
Departament d'Enginyeria Electrтnica, Elиctrica i Automatica
Av. Paпsos Catalans 26, 43007 Tarragona, Spain

Analysis and Design of Metallo-Dielectric Photonic Crystals

Thesis presented for the qualification of Ph.D.
by
M.A. Ustyantsev

Director:

Dr. Lluís F. Marsal

Tarragona 2007

Contents

4

Acknowledgements

This thesis would not have been possible without collaborations, the help and the work of a number of people.

Here, I would like to express my gratitude to all of them.

My heartfelt gratitude goes to my advisor and supervisor Dr. Lluís F. Marsal, for offering me the chance to carry out this work in his research group, for his invaluable guidance, helpful suggestions and endless support. The experience that I have gained by working in his group will be of invaluable importance.

Very special thanks to Dr. Josep Ferré-Borrull from whom I learnt a lot, including the importance of the careful work. His invaluable comments and suggestions concerning this work kept me always standing.

I would like to acknowledge the help and fruitful discussions I had have with Dr. Josep Pallarés.

I also thanks to Generalitat de Catalunya for providing the financial support which made the work in this thesis possible.

I am thankful to members of DEEEA-URV for all kind of help I have always got when I needed it and for the friendly working atmosphere.

I would like to thank to my colleagues and friends – Trifon and Mariana, for their priceless help during my first year at the URV. Special thanks go to Trifon, who helped me to understand the "magic" world of the photonic crystals.

I wish to thanks "post-soviet" community: A. Chabanenko, V. Khatko, I. Maksymov, R. Pavelko, and A. Vasiliev for their support and the friendship. Also I would like to thank to my colleagues from the NePhos group: Elisabet, Hamdy, Faruk and Ivaldo, Abel, Lukas, Zdenek, Pilar, Raquel and Joaquin.

I would like to express my gratitude to all my teachers and colleagues from the Kharkov National University of Radio Electronics.

Finally, I am grateful for the love and support that I am receiving from family. My father and early gone mom tried their best to cheer me on. Thank you a lot!

M.A. Ustyantsev

Tarragona, January 2007

Preface

The focus of the work presented in this thesis was the study and analysis of the optical properties of the metallo-dielectric photonic crystals. The main goal of this work was to show that metallic scatters embedded into dielectric host can lead to different behaviour of such structures.

The correctness of the results obtained in this thesis is confirmed by comparing with results obtained by other groups. The results of the present thesis were presented at national and international conferences and published in international journals.

The thesis is organized as follows:

The first chapter gives the short introduction to basic optical properties of the photonic crystals. Possible areas of applications as well as the main fabrication processes are also given. The brief introduction to basics optical properties of metals is also described. After that, the theoretical concepts of the metallo-dielectric photonic crystals are provided in conjunction with some areas of application. The basic steps of the fabrication of the metallo-dielectric photonic crystals are shortly reviewed.

Chapter 2 gives the brief introduction into the optics of the metals. It also describes the possible modification of Drude and Drude-Lorentz models of the dielectric functions used in the theoretical calculations of the optical properties of metals to achieve the realistic behaviour.

Chapter 3 described the numerical methods for calculations of the photonic band structures used in this work with description of the plane-wave expansion method (PWEM). Possible modification of this method in order to include the frequency-dependent dielectric constants is also outlined. After that, the finite-difference time-domain method (FDTD) is introduced. The basics of this method along with stability, initial and boundary conditions are presented. The advantages and disadvantages are also reviewed. The modifications of the FDTD method for including Drude model of metals are presented. The two different approaches for calculation of the photonic band gaps by the FDTD method are given. The brief reviews of other methods used for photonic band structure analysis conclude this chapter.

In chapter 4 it is reported that metallo-dielectric photonic crystals embedded into dielectric host with dielectric constant different from the air can essentially modify the optical properties of such structures. In particular, changing the dielectric constant of the background leads to augmentation of the existing band gaps and also to the creation of the new one. A numerical examples is given for a two-dimensional square lattice of metallic circular cylinders and triangular lattice of rods with square cross-section embedded into the dielectric matrix.

Chapter 5 describes the influence of the dielectric background on the quality factors of the metallo-dielectric photonic crystals with defect introduced in it. The obtained results revealed that changing the dielectric constant of background and/or the radius of the defect rod can greatly enhance the quality

factors of the "defective" structure. Moreover, the results show that optimal value of the quality factor exists for some range of the radiuses of the defect.

Chapter 6 presents an approach to calculate the quality factors of real metals under realistic conditions. When parameters that properly describe the metal are taking into account it was shown that quality factors are drastically reduced from values when lossless model is used.

The summary, the discussions and the future work are given in the chapter 7, which completes the thesis.

Chapter 1

Fundamentals of Photonic Crystals

The photonic crystals are artificially created materials that can do to photons what an ordinary semiconductor does to electrons: they can exhibit a band gap in which photons with certain energies cannot propagate inside the crystal, regardless of polarization and propagation direction.

Photonic crystals are characterized by three parameters: the lattice topology, the spatial period and the dielectric constants of the constituent materials. By suitable selection of these parameters, a gap in the electromagnetic dispersion relation can be created, within which the linear propagation of electromagnetic waves is forbidden. This forbidden frequency range is called the *photonic bandgap.* It is said that a photonic bandgap is *complete,* if a forbidden gap exists for all polarizations and all propagation directions. It is common to distinguish one-, two- and three-dimensional photonic crystals by the number of dimensions within which the periodicity

has been introduced into the structure. Examples of one-, two- and three-dimensional photonic crystals are given in Figure 1.1. Necessary but not sufficient conditions to obtain a *complete photonic bandgap* are a periodicity in the three spatial directions and a large difference in the dielectric constants of the constituent materials.

In 1987 E. Yablonovitch [4] proposed to use a three-dimensional periodic medium, which he called a *photonic crystal,* to inhibit the spontaneous emission and to realize localized defect modes and consequently to enhance the spontaneous emission. In the same years, S. John [5] proposed the use of a disordered three-dimensional periodic medium to localize electromagnetic waves. Many interesting quantum optical phenomena such as the bound state of photons and non-exponential decay of the spontaneous emission were predicted. These ideas actively stimulated research area [6-10], which lead both to various unexpected results in the fundamental understanding of light-matter interaction and to various new optoelectronics and photonics applications.
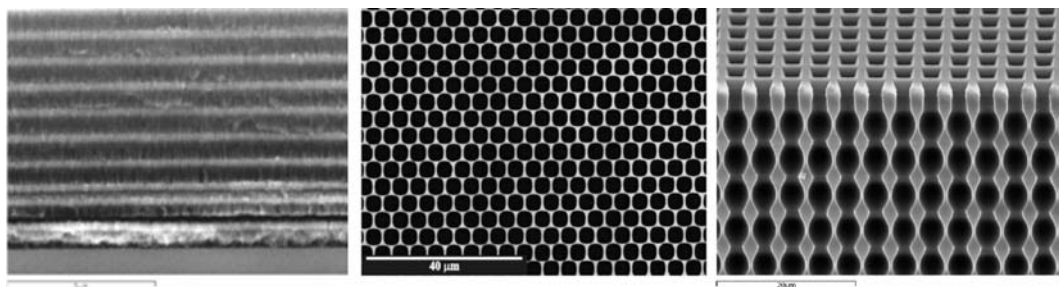
Figure 1.1. *Examples of one-, two- and three-dimensional photonic crystals. Left: SEM image of the cross section of a 1D all-silicon photonic crystal (after Xifre et. al. [1]). Center: SEM image of a 2D structure (after Trifonov et. al. [2]). Right: SEM image of a 3D structure (after Cheylan et. al. [3]).*

1.1 The Origin of the Photonic Bandgap

In conventional electromagnetic gratings such as periodic waveguides, distributed feedback lasers, holography, and x-ray diffraction, the gratings consist of weak perturbations about a mean refractive index. The theoretical treatment of these weak gratings is based on a perturbation approach that leads to coupled mode equations for a finite set of plane waves in the grating. Not all conventional periodic structures have weak gratings. In multilayer dielectric stacks used for high reflection and antireflection coatings on optical components, large one-dimensional PBGs are present.

Here one can take advantage of the simplicity of the one-dimensional systems to explain the physical origin of the PBG.

A one-dimensional photonic crystal is made of layers with alternating dielectric constant [6], as shown in Figure 1.2. This system repeats in the z-direction with period a, which will be of the order wavelength of the light. A plane wave travelling in the z-direction, along the line of periodicity, will be scattered at the interface between two medias. This gives rise to forward and backward propagating waves within the structures. These waves will interfere to form standing waves.

The dispersion for light in an isotropic dielectric material is given by the equation:

$$\omega(k) = \frac{ck}{\sqrt{\varepsilon}},$$

(1.1)
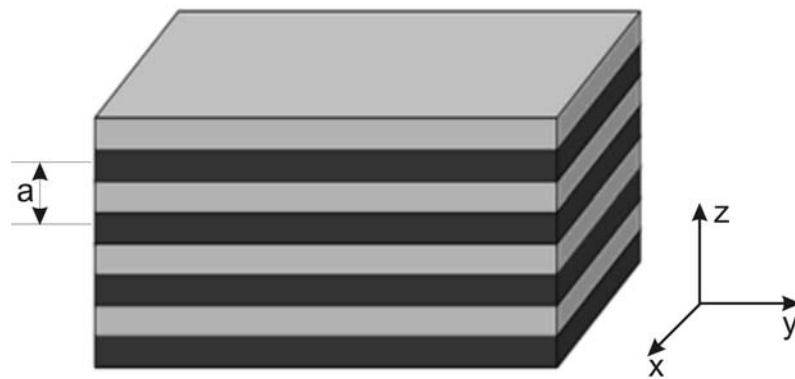
Figure 1.2. *A one dimensional photonic crystal with periodicity a. It consists of alternating layers with different dielectric constants. (After [6]).*

where c is the speed of light, k is a wavevector and ε is a dielectric constant, given by the properties of the dielectric medium. This equation shows that the energy of light varies linearly with momentum, with zero momentum corresponding to zero energy. Figure 1.3 plots the dispersion relation of the previous structure

In Figure 1.3 (a), both dielectric layers have the same dielectric constant, forming a single slab of material assigned an artificial periodicity. Figure 1.3 (b), and (c) show the dispersion of light propagating through a dielectric stack where the different layers have a difference in dielectric constant. Many aspects of this graph are similar to that of the Figure 1.3 (a), except now there is a region of frequency space where no photonic mode exists; this is known as a photonic bandgap. This bandgap arises from the difference in field energy location.

a)

b)

c)
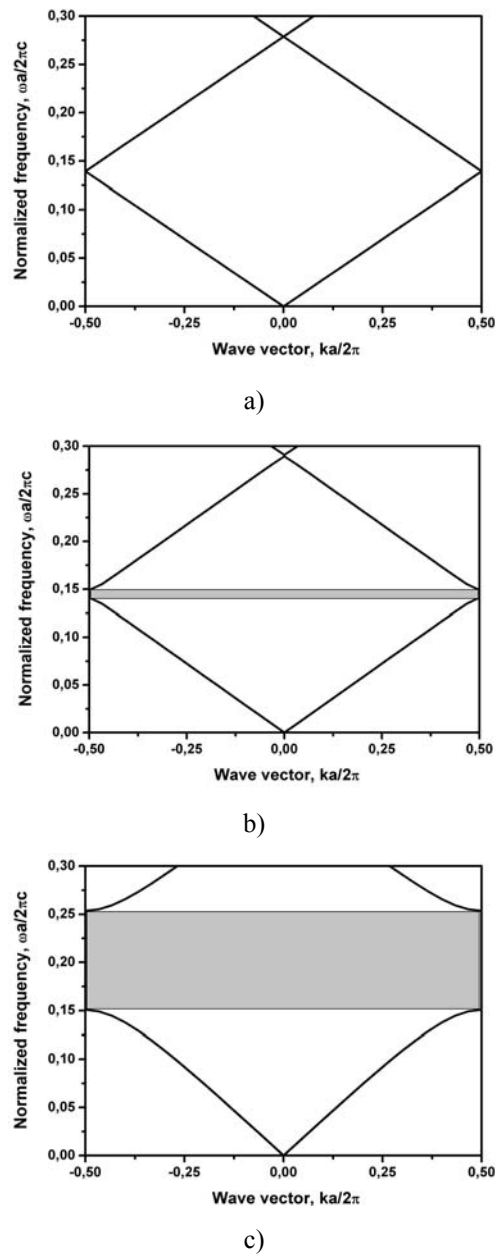
Figure 1.3. *The photonic band structures shown for three different multilayer films, all of which have layers of width 0.5a. a)each layer has the same dielectric constant ε = 13; b) layers alternates between ε = 13 and ε = 12; c) layers alternates between ε = 13 and ε = 1. The photonic band gaps are shown by shaded areas. (After [6]).*

For a physical insight into this bandgap formation it is useful to return to real space and consider the electric field directly above and below the gap, where $k = \pi/a$. Here, the modes are standing waves with wavelengths equal to $2a$. These modes have only two possible configurations within the structure (Figure 1.4 (a), (b).), their nodes positioned within either the high or low dielectric constant layers. Any other configuration violates the symmetry of the system, and hence is forbidden. It now becomes clear that while both modes have the same wavelength, the mode concentrated in the high index material will experience a shorter effective distance, and hence a lower frequency, than the mode concentrated in the low index material. This difference in frequency provides the energy gap in the photonic dispersion relation analogous to the energy gap between the valence and conduction bands in a semiconductor material. It is common to call the lower frequency band as "dielectric band" and the higher frequency band as "air band". Indeed, the two systems are almost completely analogous, allowing the photonic system to be written in 'Bloch form', consisting of a plane wave modulated by a function arising from the periodicity of the lattice. This approach becomes particularly useful when considering the coupling of light into two and three dimensional photonic crystals.

"Dielectric" band frequency

a)   High index   Low index

"Air" band frequency

b)   a
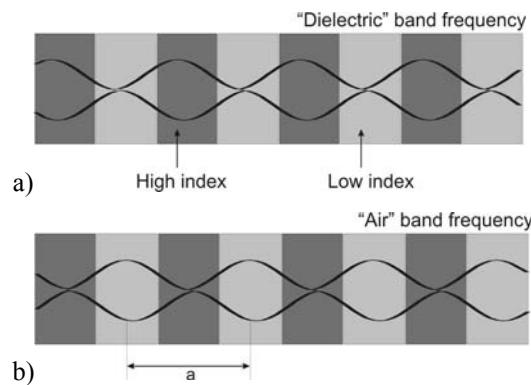
Figure 1.4. Schematic illustration of the modes associated with lowest band gap of Figure1.3 (c) Electric field of the band 1.(b) Electric field of the band 2. (After [6]).

1.2 Properties of Photonic Crystals

1.2.1 Polarization

In the two-dimensional case, all derivatives with respect to z coordinate vanish and the study is restricted to the propagation along the cross-section plane of the crystal, i.e. the xy plane. This crucial property opens the possibility of separately studying the problems corresponding to the fundamental cases of polarisation. These polarisation modes are referred to as TM and TE [11] polarisations (Figure1.5). In the case of the TM polarization the components of magnetic field are parallel to the xy plane and $E_z \neq 0$. For the TE case the $H_z \neq 0$ and electric field components lie in the xy plane.
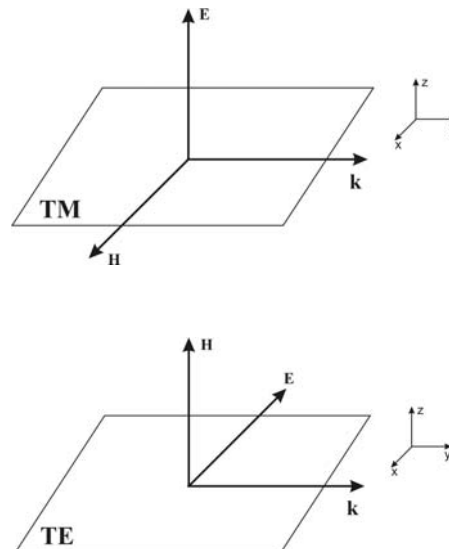
Figure 1.5. *The polarization definition. a) TM polarization the components of magnetic field are parallel to the* xy *plane and* $E_z \neq 0$ *.bB)For the TE case the* $H_z \neq 0$ *and electric field components lie in the* xy *plane.*

1.2.2 Lattice

A photonic crystal is built of a basic block (unit cell) repeated infinitely and periodically in space. The spatial arrangement of the unit cell is a lattice. Each lattice is spanned by direct lattice vectors [12]. For each direct lattice the reciprocal lattice is existed. With given set $\vec{a}_1$, $\vec{a}_2$, $\vec{a}_3$ of direct lattice vectors, the corresponding set $\vec{b}_1$, $\vec{b}_2$, $\vec{b}_3$ of reciprocal vectors is defined by the expression:

$$\vec{a}_i \cdot \vec{b}_j = 2\pi\delta_{ij}, \qquad \delta_{ij} = \begin{cases} 1, & i = j \\ 0, & i \neq j \end{cases}. \qquad (1.2)$$

The reciprocal vectors can be generated by the following equations that are given by:

$$\vec{b}_1 = 2\pi\frac{\vec{a}_2 \times \vec{a}_3}{V_c}, \qquad \vec{b}_2 = 2\pi\frac{\vec{a}_3 \times \vec{a}_1}{V_c}, \qquad \vec{b}_3 = 2\pi\frac{\vec{a}_1 \times \vec{a}_2}{V_c} \qquad (1.3)$$

where $V_c = \vec{a}_1(\vec{a}_2 \times \vec{a}_3)$ is the volume of the primitive unit cell of the crystal lattice. The primitive cell of the reciprocal space has a volume $V_c' = \vec{b}_1(\vec{b}_2 \times \vec{b}_3)$ that is related to V_c by:

$$V_c' = \frac{8\pi^3}{V_c}, \qquad (1.4)$$
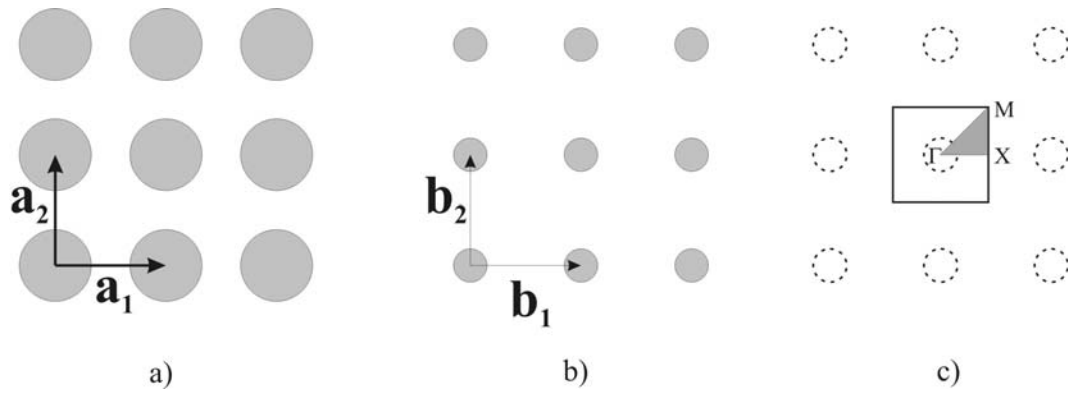
Figure 1.6. *Square lattice. (a) Direct lattice generated by the basis vectors $\vec{a}_1$, and $\vec{a}_2$. (b) The corresponding reciprocal lattice and reciprocal vectors $\vec{b}_1$, and $\vec{b}_2$. (c) First Brillouin zone and the irreducible region (dark triangle).*

From their definition we see that crystal lattice and reciprocal lattices are inverses of each other: lattice vectors have dimension of the length, while reciprocal vectors have dimension of the inverse length.

In the two dimensions $\vec{a}_3$ can be chosen arbitrarily and the most studies geometries are the square and triangular lattices. Figure 1.6, shows a square lattice in both real and reciprocal space along with the basis vectors. In Figure 1.6 (c) the irreducible first Brillouin zone with the high symmetry points is shown by the dark triangle.

The direct vectors of square lattice are

$$\vec{a}_1 = a(1,0), \quad \vec{a}_2 = a(0,1) \ , \tag{1.5}$$

where a is the lattice constant.

The reciprocal vectors are:

$$\vec{b}_1 = \frac{2\pi}{a}(1,0), \quad \vec{b}_2 = \frac{2\pi}{a}(0,1) \ . \tag{1.6}$$

The high symmetry points of the first Brillouin zone have coordinates: $\Gamma = (0, 0)$, $X = (\pi /a, 0)$, $M = (\pi /a, \pi/a)$.

Figure 1.7, shows a triangular lattice in both real and reciprocal space along with basis vectors. In Figure 1.7 (c) the irreducible first Brillouin zone with the high symmetry points is shown by the dark triangle.

Direct vectors of triangular lattice are

$$\vec{a}_1 = a\left(\frac{1}{2}, \frac{\sqrt{3}}{2}\right), \quad \vec{a}_2 = a\left(\frac{1}{2}, -\frac{\sqrt{3}}{2}\right) \ . \tag{1.7}$$

a)   b)   c)
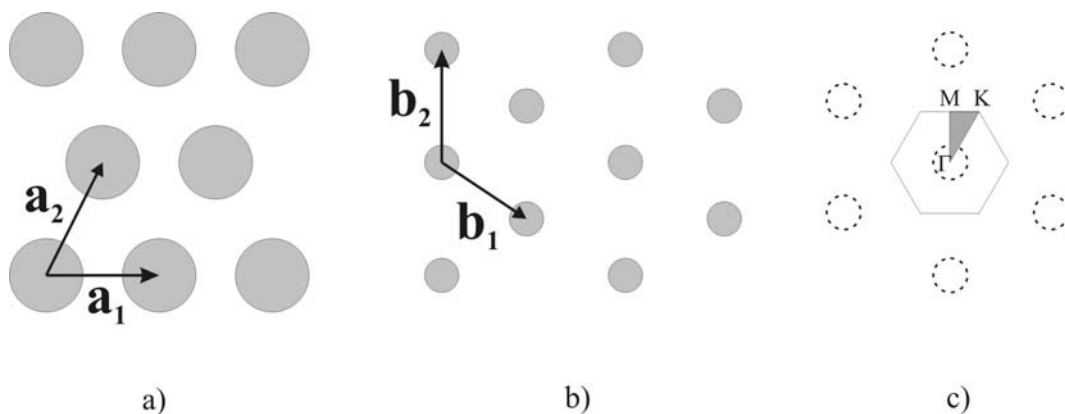
Figure 1.7. Triangular lattice. (a) Direct lattice generated by the basis vectors $\vec{a}_1$, and $\vec{a}_2$. (b) The corresponding reciprocal lattice and reciprocal vectors $\vec{b}_1$, and $\vec{b}_2$. (c) First Brillouin zone and the irreducible region (dark triangle).

The corresponding reciprocal vectors are:

$$\vec{b_1} = \frac{2\pi}{a}\left(\frac{\sqrt{3}}{2}, \frac{1}{2}\right), \quad \vec{b_2} = \frac{2\pi}{a}\left(\frac{\sqrt{3}}{2}, -\frac{1}{2}\right). \tag{1.8}$$

The high symmetry points of the first Brillouin zone of the triangular lattice have coordinates: $\Gamma = (0, 0)$, $K = (2\pi/3a, 2\pi/\sqrt{3}a)$, $M = (0, 2\pi/\sqrt{3}a)$.

1.2.3 Density of States

The photonic density of states (DOS) plays an important role in understanding the optical properties of a photonic crystal because it describes the integral availability of allowed states in a certain frequency range regardless of band-index n or wavevector $\vec{k}$. The calculation of the DOS provides a cross-check for the existence of a photonic band gap. The total DOS is defined as in Ref. [13] :

$$\rho(\omega) = \sum_n \int_{1BZ} d^3k \cdot \delta\left(\omega - \omega_n(\vec{k})\right), \tag{1.9}$$

where the k-space integration covers the whole first Brillouin zone (1BZ) and $\omega_n(\vec{k})$ is the eigenvalue for band-index n and wavevector. δ is the Dirac delta function. In the homogeneous media $\rho(\omega)$ is proportional to ω^2. A vanishing DOS is the commensurate condition for a complete photonic bandgap.

1.2.4 Group Velocity

The group velocity of the radiation modes has very important role in the light propagation and optical response in the photonic crystal. The group velocity of the eigenmodes is defined as the gradient of the dispersion curves that is the derivative of the angular frequency ω with respect to the wavevector $\vec{k}$:

$$\vec{v}_g = \frac{\partial \omega_n}{\partial \vec{k}} \tag{1.10}$$

Usually, in the calculations, the derivative in the equation (1.10) can be replaced by numerical differentiation:

$$\vec{v}_g = \lim_{\Delta \vec{k} \to 0} \frac{\omega_{\vec{k}+\Delta \vec{k},n} - \omega_{\vec{k},n}}{\Delta \vec{k}} \tag{1.11}$$

Another method to calculate the group velocity is by using the Hellman-Feynman theorem [8]. This procedure gives more precisely results but also is much more complicated.

1.2.5 Example of Band Diagram, DOS, and Group Velocity

In order to illustrate the quantities mentioned above we have computed the photonic band structure for TM-polarization (Figure 1.8 (a)) and TE-polarization (Figure 1.8 (b)) in a two-dimensional photonic crystal consisting of square lattice (with lattice constant a) of cylindrical air pores ($r_{pore} = 0.475a$) in a silicon matrix

with dielectric permittivity $\varepsilon_{Si} = 12$. This structure exhibits two photonic bandgaps for TM polarization. The larger bandgap extends between $\omega_1 = 0.238$ x $2\pi c/a$ to $\omega_2 = 0.292$ x $2\pi c/a$ and the smaller one extends from $\omega_1 = 0.422$ x $2\pi c/a$ to $\omega_2 = 0.464$ x $2\pi c/a$. Also, we can define the width of the PBG as $\Delta\omega = \omega_2 - \omega_1$ and the center frequency as $\omega_g = (\omega_2 + \omega_1) / 2$. Usually, the PBG is normalized as $(\Delta\omega / \omega_g)$ and expressed in percentage. For this example we have for first PBG $\Delta\omega / \omega_g = 20.4\%$ and for second PBG the ratio $\Delta\omega / \omega_g$ is equal to 9.5%. For TE polarization only one band gap between $\omega_1 = 0.45$ x $2\pi c/a$ to $\omega_2 = 0.5$ x $2\pi c/a$ exists with the ratio $\Delta\omega / \omega_g$ equal to 10.5%.
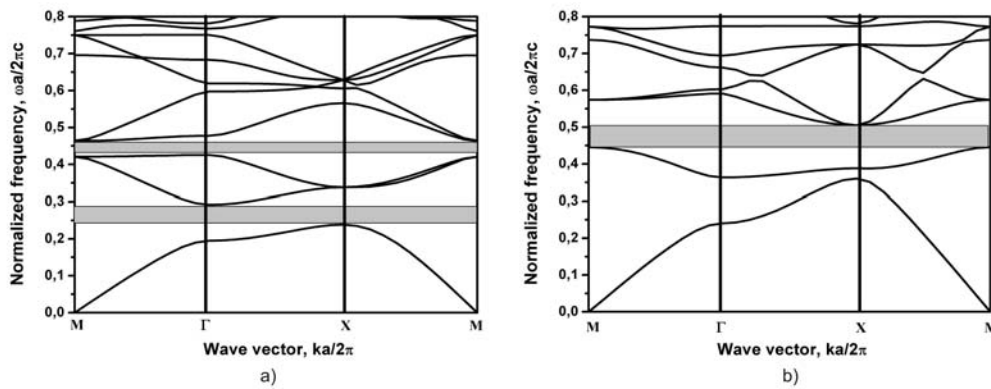
Figure 1.8. *Example of band diagram for two dimensional photonic crystal made of cylindrical air pores with radius $r_{pore} = 0.475a$ in a square lattice. The material of background is silicon ($\varepsilon_{Si} = 12$). The photonic band gaps are shown by shaded areas. a) TM polarization; b) TE polarization.*

To cross-check our results we also computed the DOS (Figure 1.9) of the given photonic crystal. We see that regions of zero DOS are photonic band gaps and these regions correspond to photonic band gaps of Figure 1.8.
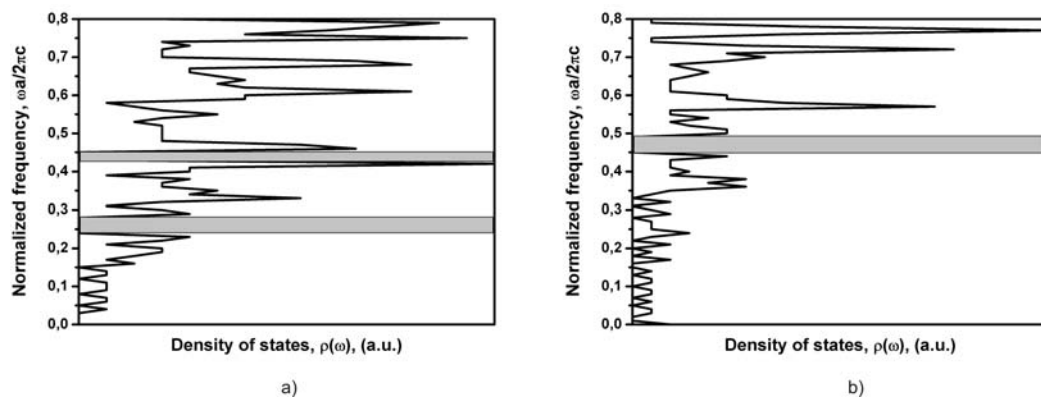
Figure 1.9. *Density of states for the structure shown in the Fig.1. The photonic band gaps are shown by shaded areas. a) TM polarization; b) TE polarization.*

In order to understand the wave propagation in a photonic crystal, it is necessary to obtain group velocities from the photonic band structure. In Figure 1.10 we show the variation of the group velocities along the high-symmetry lines of the first Brillouin zone associated with bands 1, 3, and 5 of our model system. As expected from the corresponding band structure in Figure 1.8, the higher bands exhibit rather low values of the group velocity. In particular, the values of group velocity for band 3 along the Γ-X direction are about an order of magnitude smaller than the group velocity in band 1. A low group velocity increases a field amplitude and also cause a long interaction time between an electromagnetic field and a matter.
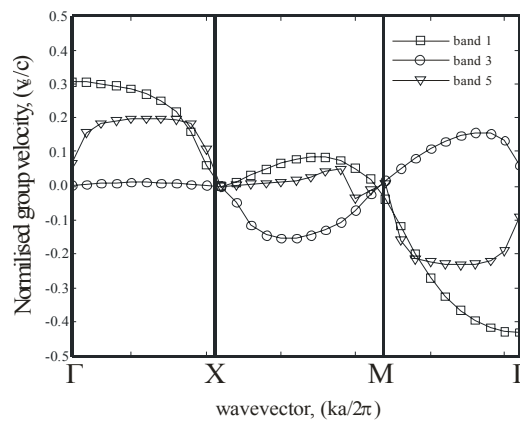
Figure 1.10. *Group velocities for bands 1, 3, and 5 corresponding to the band structure in Figure 1.8 (a). The group velocities of these bands exhibit extreme variations which may have numerous applications.*

1.3 Devices Based on the Photonic Crystals

With the demonstration the physics of the photonic band gap formation, focus turned to the engineering of devices utilizing the photonic band structure.

Waveguides

Guiding light using waveguides is a one of fundamental properties of optics that enables a range of all-optical devices to be created. Waveguides not only transfer light from one part of a circuit to another, but also are used in many applications such as junctions, couplers and lasers. Although three dimensional photonic crystals would be preferred since they control light propagation in all three directions, they are difficult to fabricate. A more suitable approach is the use of two-dimensional photonic crystal waveguides [14-17], which are based on planar structures.

The planar photonic crystal waveguide consists of a guiding layer with a high refractive index and a lower and upper cladding layers, with a lower

refractive index. The width of the guided mode depends on the thickness of the core layer and the difference of the refractive index between core and cladding.

The feature to guide light through low-loss sharp bends in photonic crystals (Figure 1.11) has attracted a lot of attention. High-efficiency bends have been demonstrated in many different photonic crystal geometries [18].
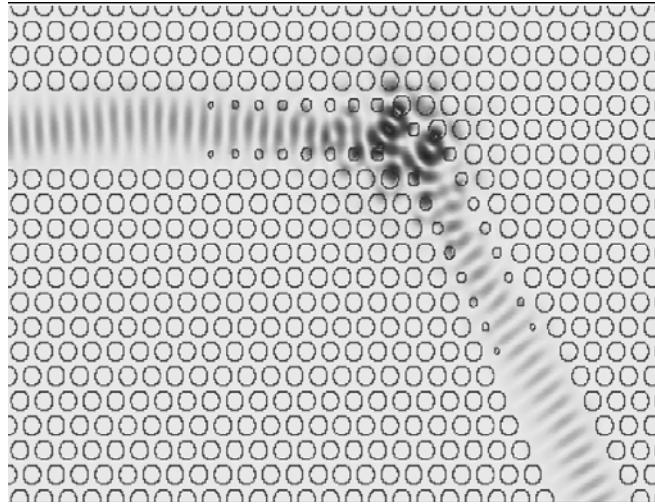
Figure 1.11. *Electric field distribution in a sharp bend photonic crystal waveguide. (After [18]).*

Microcavities

Any defect surrounded by a photonic crystal with a band gap defines a cavity. Microcavities provide both sharp spectral responses and large field enhancement within the microcavity. The former can be used for narrow bandwidth filters and wavelength selective filters. High field intensities due to the light being confined in a small microcavity can enhance light-matter interaction, making them ideal for photonic applications such as lasers.

In 2001 Vuckovic et al. reported a theoretical study of various microcavity designs [19]. Microcavities with quality factor > 10000 were achieved by varying the radius and shape of the cylinders in the area surrounding defect. Recently, in 2005 group by Noda reported the measured quality factor ≈ 1000000. This huge value was achieved by shifting the position of the neighbour holes surrounding the microcavity (Figure 1.12) [20].
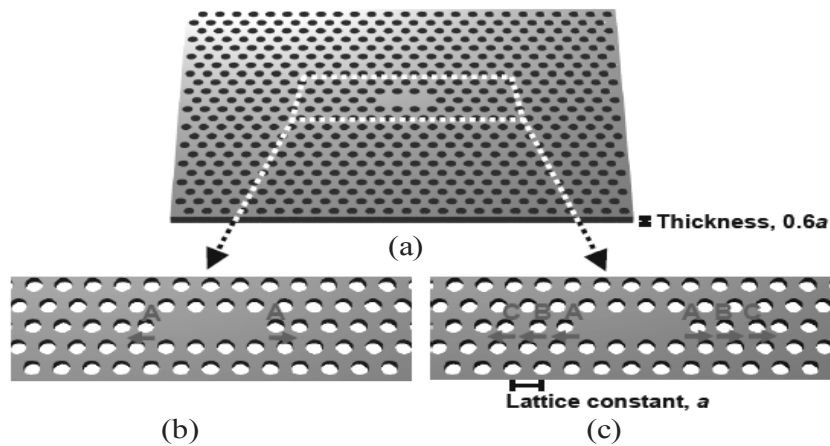
Figure 1.12. *(a) Schematic of the point-defect nanocavity in a 2D photonic crystal l slab. The base cavity structure is composed of three missing air holes in a line. The photonic crystal structure has a triangular lattice of air holes with lattice constant a. The thickness of the slab and the radius of the air holes are 0.6a and 0.29a, respectively. (b) The designed cavity structure created by displacing two air holes at both edges in order to obtain high-quality factor. (c) The designed cavity structure created by fine-tuning the positions of six air holes near both edges to obtain an even higher quality factor. (After [20]).*

Photonic Crystal Fibers

Photonic-crystal fiber (PCF) [21, 22], is a new class of optical fiber based on the properties of photonic crystals (Figure 1.13 (a), (b)). Because of its ability to confine light in hollow cores or with confinement characteristics not possible in conventional optical fibers, PCF is now finding applications in optical

communications, fiber lasers, nonlinear devices, high-power transmission, highly sensitive gas sensors (etc.), and other areas.

More specific categories of PCF include photonic-bandgap fiber (PCFs that confine light by band gap effects), holey fiber (PCFs using air holes in their cross-sections), hole-assisted fiber (PCFs guiding light by a conventional higher-index core modified by the presence of air holes), and Bragg fiber (photonic-bandgap fiber formed by concentric rings of multilayer film).Photonic crystal fibers can be divided into two modes of operation, according to their mechanism for confinement.

(a)   (b)
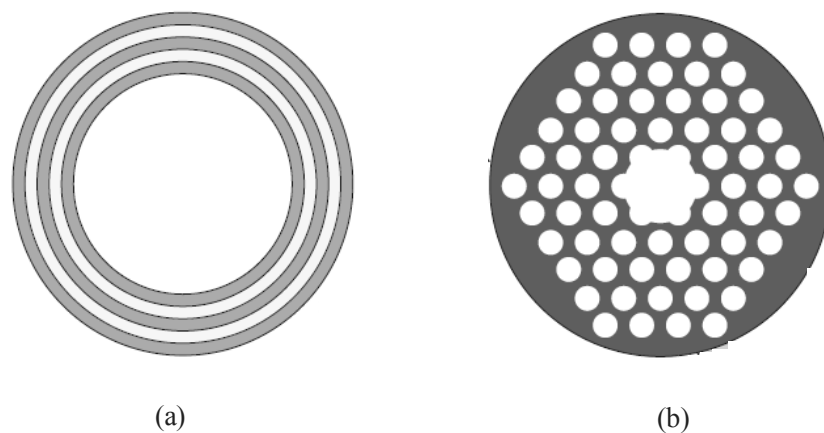
Figure 1.13. *Photonic crystal fibers. (a) Brag fiber, utilizing one-dimensional photonic crystal. (b) Photonic crystal fiber, utilizing concept of two-dimensional photonic crystal.*

Those with a solid core, or a core with a higher average index than the microstructured cladding, can operate on the same index-guiding principle as conventional optical fiber — however, they can have a much higher effective-index contrast between core and cladding, and therefore can have much stronger confinement for applications in nonlinear optical devices, polarization-maintaining fibers, etc. (or they can also be made with much lower effective index contrast). Alternatively, one can create a "photonic bandgap" fiber, in which the

light is confined by a photonic bandgap created by the microstructured cladding - such a bandgap, properly designed, can confine light in a lower-index core and even a hollow (air) core. Bandgap fibers with hollow cores can potentially circumvent limits imposed by available materials, for example to create fibers that guide light in wavelengths for which transparent materials are not available (because the light is primarily in the air, not in the solid materials). Another potential advantage of a hollow core is that one can dynamically introduce materials into the core, such as a gas that is to be analyzed for the presence of some substance.

1.4 Fabrication Methods

A wide variety of methods have been used to fabricate photonic crystals. Some of them are more suitable for the fabrication of 1D and 2D photonic crystals, while others are useful when one needs to localize photons in three dimensions.

Self-assembly methods. Colloidal self-assembly methods seems to be the most efficient method for fabrication of 3D photonic crystals. In this method, predesigned building blocks (usually monodispersed silica or polystyrene nanospheres) spontaneously organise themselves into a stable structure [23].
A number of techniques are available for colloidal fabrication. A widely used technique for creating colloidal crystals is gravity sedimentation. Sedimentation is a process whereby particles, suspended in a solution, settle to the bottom of the container, as the solvent evaporates. Another self-assembling technique is called cell method [24]. In this method an aqueous dispersion of spherical particles is injected into a cell formed by two glass substrates and a frame of photoresist

placed on the surface of the bottom substrate. One side of the frame has channels that can retain the particles, while allowing the solvent to flow through. The particles settle down in the cell to form an ordered structure (usually fcc structure).

Lithography. Generally, lithography is used to pattern the substrate for 2D photonic crystals. Considering the small size of the lattice (periodicity between 0.2 and 0.7 µm, with sub-0.1 nm control of feature size desirable) for a PBG in optical range, standard photolithography techniques cannot be used. The most poplar alternative is *electron beam lithography*. Electron beam lithography is a method that enables to create various photonic crystals with extremely high resolution. In this method, the sample (wafer) is covered with an electron-sensitive material called resist. The material, used as resist, undergoes a substantial change in its chemical or physical properties, when it is exposed to an electron beam [25]. The beam position and intensity are computer-controlled, and electrons are delivered only to a certain areas to get the desired pattern. After exposition, a part of the resist is dissolved away and the sample can be further processed with etching procedures to get the final structure. Although its resolution is high, electron beam lithography is very expensive method.

Etching methods. These methods are more suitable for the fabrication of 2D photonic crystals. These methods utilize marking of a planar pattern of unwanted areas on the surface of a semiconductor, using a lithographic technique. There are two different etchings:

Dry etching. An example is reactive-ion etching (RIE), which utilizes reactive ions generated by plasma discharge in a chloride-based ($SiCl_4$ and Cl_2) or fluorine-based (CHF_3, CF_4, CF_6, and SF_6) reactive gas. These ions are accelerated toward the sample surface under an electric field. This dry etching provides a

good control over the hole size, but has a limited maximum etching depth. The method has been used for many semiconductors, such as GaAs, AlGaAs, and Si.

Wet etching. An example is electrochemical etching that has also been used for many semiconductors. Electrochemical etching of Si to produce macroporous silicon photonic crystal is an example. In this case, a pre-pattern with etch pits was first created on the front of a silicon wafer by using lithographic patterning and subsequent alkaline chemical etching using KOH or TMAH solutions. The wafer was then mounted in an electrochemical cell and electrochemically etched using an HF solution. The pre-etched pits form nucleation centres for electrochemical etching. The advantage provided by an electrochemical etching method is that high aspect ratio can be easily produced.

Another approach to produce 2D photonic crystal using an electrochemical method is provided by anodic oxidation of aluminum in acidic solutions, which is known to produce highly ordered porous structure in the resulting alumina (Al_2O_3) that consists of a closely packed array of columnar cells [26, 27]. The pore size and density of the pores in alumina can be precisely controlled by selecting the anodization condition (choice of acid, applied voltage) and pre-texturing of the aluminium surface with an array of nanoidentation using a SiC mold [28]. This porous Al_2O_3 can be used as a template to form other photonic media that can be grown in the pores, and Al_2O_3 can subsequently be etched out. Filling of a polymer in the pores can produce a negative replica that can subsequently be used for growth of other periodic structures [29].

Holographic methods. These methods, which utilize interference between two or more coherent light waves to produce a periodic intensity pattern [30], have been used to produce a periodic photoproduced photonic structure in a resin (photoresist). This method has been in practice for a long time. Recent

developments use photopolymerizable (or photocrosslinkable) medium containing inorganic nanoparticles (as TiO_2, metallic nanoparticles) or liquid crystal nanodroplets.

The holographic method can also be used to fabricate an electrically switchable polymer-dispersed liquid crystal photonic bandgap material [31]

1.5 Metallic Photonic Crystals

1.5.1 Basics

To achieve the band gap, the system must have the high contrast in the refractive index, while at same time have negligible absorption of light. These conditions have severely restricted the set of dielectrics that exhibit a photonic bandgap. One suggestion is to use metallic scatterers rather than dielectric one. The huge value of the metallic dielectric function means that a fewer number of periods would be enough to achieve photonic bandgap effect [32, 33]. However, care must be taken, since metals are very absorptive, especially at optical frequencies. That is why the most early proposed metallic photonic crystals operated at microwave frequencies where the absorption is smaller [34-40]. However, there are some situations where the redistribution of the photon wave field, due to the periodicity, prevents the metal from absorbing the light. [41]. Another interesting field that attracted a lot of attention is called surface plasmon optics. Surface plasmons are characterized as surface bound waves that propagate at the interface between metal and dielectrics.

In 1994 Kuzmiak et al. [42] studied the two-dimensional case of an array consisting of infinitely long metallic cylinders arranged in square and triangular lattices embedded in air. Their results showed a qualitative difference in the band structure of the two different polarizations.

For TE polarization (Figure 1.14), the obtained results show that the band structure is very similar to that of free space with exception of number superimposed flat bands. For TM polarization (Figure 1.15) the situation was different. No flat bands were founded, but a finite cut-off frequency was observed, below which no propagating modes exist. This was explained that TM modes can couple to longitudinal oscillations of charge along the length of the cylinders. In the TE polarization case the existence of flat bands was explained by discrete excitations associated with isolated cylinders. Later, in 2001 Sakoda proved that these flat bands are due to the presence of the surface plasmon polaritons [43].
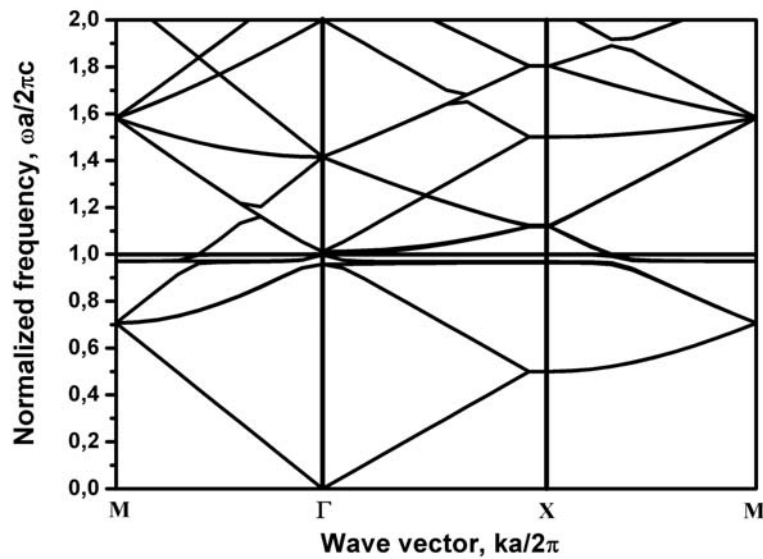
Figure 1.14. *The photonic band structure of a square lattice of metallic cylinders in air with r = 0.0178a. TE polarization.*
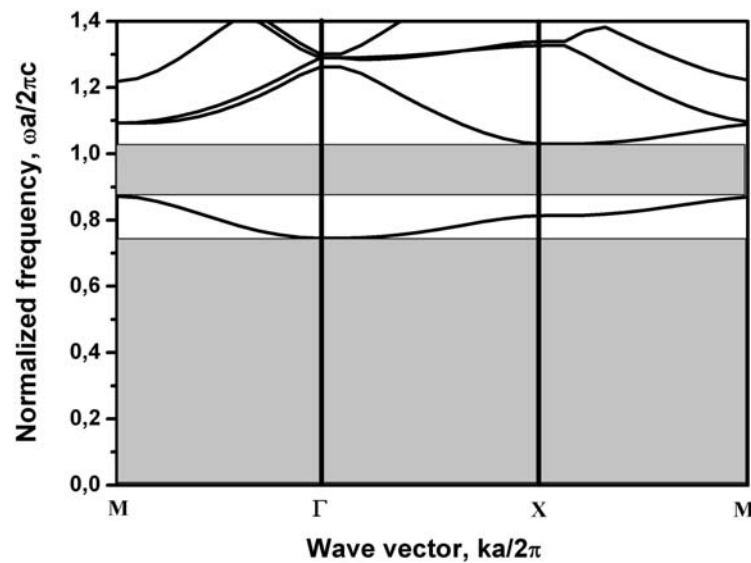
Figure 1.15. The photonic band structure of a square lattice of metallic cylinders in air with r = 0.472a. TM polarization.

First three-dimensional metallic photonic crystal was proposed by group of Yablonovitch [44]. This structure was made from metal wires based on diamond lattice with centimetre lattice spacing. The forbidden band bellow a cut-off frequency in GHz frequency range was demonstrated. Another group [45] proposed a more simple structure based on metallic square mesh separated by dielectric. Their results were in qualitative agreement with the Yablonovitch structure, identifying a finite cut-off frequency below which no modes could propagate.

In 1999 A. Moroz [46] suggested that it is possible to avoid constraint on the dielectric constant by using metallic spheres coated by dielectric layer. The results showed that the gap width can increase up to 50% as compared to the same

crystal made from simple dielectric spheres. He proposed to incorporate metals into a photonic crystal that has gap in a certain frequency window, in which metal behaves as conventional, but also highly dispersive, dielectrics. In this frequency window the absorption can be neglected. For example in a system of metal spheres in dielectric background with $\varepsilon_b = 1$, if the periodicity is chosen such that the stop band opens in the frequency range that $\varepsilon_{sphere} < 1 < \varepsilon_b$, then this system acts as an air sphere type structure and the plasma frequency, $\varepsilon_{sphere} (\omega_p) = 0$, the dielectric contrast becomes extremely large. The first property is necessary for opening a complete photonic band gap, and the second ensures opening of the maximum width band gap for this structure.

1.5.2 Examples of Applications

Although, that metallic photonic crystals have received far less attention than dielectric photonic crystals, it has been suggested that periodic metallic structures have important applications, such as cavities [47], waveguides [48], and antennas [49, 50]. Furthermore, metallic photonic crystals, with careful design, have robust photonic band gaps. Chan *et al.* [51, 52] have designed a three-dimensional photonic crystal constructed by metallic 'photonic atoms', which are spheres with a dielectric core, a metal coating, and an outer insulating layer (a system made up of nontouching solid metal spheres will have qualitatively similar behavior). As long as the sphere filling ratio exceeds a threshold, robust photonic band gap exist in any periodic structure, such as face-centered cubic (FCC), body-centered cubic (BCC), the diamond structure, and even simple cubic (SC).

The other interesting is that metals offer exciting phenomena that can be usefully applied to light emitting devices. Surface plasmons, for example, the quanta of electron oscillations at metal-dielectric interfaces, have been used to explain the "supertransmission" effect observed recently [53], where a transmission of around 4% was measured through a thin metal film perforated with holes of 2% area fill-factor and size well below cut-off (150 nm diameter holes at 1.55 μm wavelength). The best explanation put forward so far is that the incoming light excites the plasmon on one surface, which then couples to the plasmon on the other side of the metal film. This second plasmon subsequently couples to radiation modes, which makes the whole process appear as if the incoming light had been transmitted directly through the metal film. These surface plasmons are a form of surface wave that occurs at dielectric-metal interfaces, and are closely related to waveguide modes. When the metal film is corrugated, the surface plasmon experiences band gaps [54] in the same way as a mode does in a corrugated waveguide. Surface plasmons are usually associated with thin films, but they can also be observed in small metal spheres [55]. Recent works, where resonances in small metal particles have been studied, have shown that the detection efficiency of thin-film photodectors can be increased by over an order of magnitude (in a limited wavelength range) if the surface is covered with metal islands [56]. The explanation that the authors propose is that the incoming radiation couples to the metallic resonance and then to the waveguide mode of the thin absorbing film. This mechanism increases the interaction length between the incident light and the film, and thereby greatly enhances the detection efficiency.

1.5.3 Fabrication of Metallic Photonic Crystals

One of the widely used approaches to fabricate metal rods is based on various templates. One of the commonly used templates is anodic porous alumina. The pores in the template are formed by anodizing aluminum films in an acidic electrolyte. The individual pores in the alumina can be ordered into a close-packed honeycomb structure. The diameter of each pore and the separation between two adjacent pores can be controlled by changing the anodization conditions. The fabrication method of anodic porous alumina can be traced back to the work done in the 1950's, which involves a one-step anodization process. This original one-step anodization method is still used to fabricate most commercial alumina membranes.

Using the alumina membrane templates, wires of various metals, semiconductors can be fabricated. These structures can be deposited into the pores by the electrochemical deposition method. Electrodeposition is one of the most widely used methods to fill conducting materials into the pores to form continuous rods with large aspect ratios [57-60]. One of the great advantages of the electrodeposition method is the ability to create highly conductive rods. This is because electrodeposition relies on electron transfer, which is the fastest along the highest conductive path. The electrodeposition method is not limited to wires of pure elements. It can fabricate rods of metal alloys. Another important advantage of the electrodeposition method is the ability to control the aspect ratio of the metal rods by monitoring the total amount of passed charge. This is important for many applications. For example, the optical properties of the rods are critically dependant on the aspect ratio.
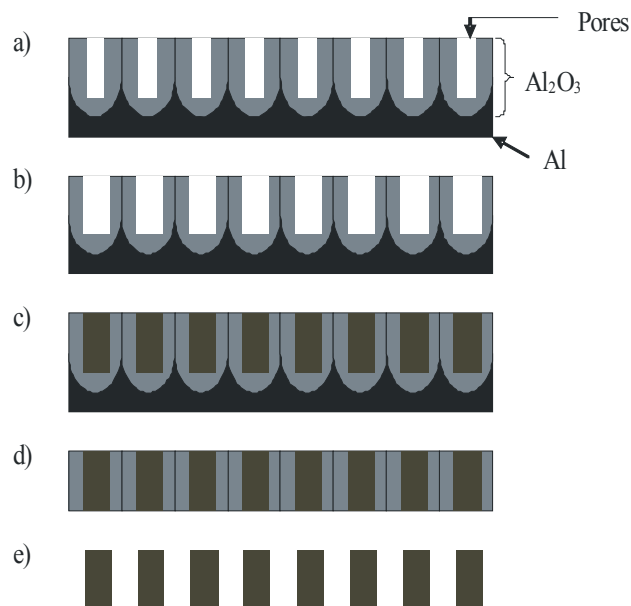
Figure 1.16. *Preparation steps for ordered array of metallic rods embedded in an alumina matrix.*

The fabrication of two-dimensional metallic photonic crystal will require five steps (Figure 1.16). First, is anodization of alumina membranes to obtain ordered pore array with straight pores from top to bottom (Figure 1.16a). Second step involved process of pores widening to thinning barrier layer which help to decrease the potential barrier for electrons to tunnel through barrier layer, when metal is deposited at the pore tips (Figure 1.16b). Third step is electrodeposition of metal from aqueous electrolyte (Figure 1.16c). The forth step includes removing of Al and barrier layer (Figure. 1.16d). The fifth step, when freely standing rods are desired, it is necessary to remove the template hosts after forming the rods in the templates (Figure 1.16e).

This task is usually accomplished by dissolving away the template materials in a suitable solvent, for example NaOH.

References

[1] E. Xifré Pérez, J. Pallarès, J. Ferré-Borrull, T. Trifonov, and L.F. Marsal, "Low refractive index porous silicon multilayer with a high reflection band", **DOI** 10.1002/pssc.200300000.

[2] T. Trifonov, L. F. Marsal, A. Rodríguez, J. Pallarès, R. Alcubilla, "Fabrication of two- and three-dimensional photonic crystals by electrochemical etching of silicon", Phys. Stat. Sol., vol. **2**, 3104, (2005).

[3] S. Cheylan, T. Trifonov, A. Rodriguez, L.F. Marsal, J. Pallares, R. Alcubilla and G. Badenes, "Visible light emission from macroporous Si," Opt. Materials, vol. **29**, 262, (2006).

[4] E. Yablonovich, "Inhibited Spontaneous Emission in Solid-State Physics and Electronics", Phys. Rev. Lett. **58**, 2059 (1987).

[5] S. John, "Strong localization of photons in certain disordered dielectric superlattices", Phys. Rev. Lett. **58**, 2486 (1987).

[6] J. D. Joannopoulos, R.D. Meade and J.N. Winn, *Photonic crystals. Molding the flow of Light* (Princeton University Press, New Jersey, 1995).

[7] K. Busch, S. Lolkes, R.B. Wehrspohn and H. Foll, *Photonic crystals. Advances in design, fabrication and characterization* (Wiley, 2004).

[8] K. Sakoda, *Optical properties of photonic crystals* (Springer Verlag, Berlin, 2004).

[9] J.-M. Lourtioz, H. Benisty, V. Berger and J.M. Gerard, *Photonic crystals. Towards nanoscale photonic devices* (Springer, Berlin, 2005).

[10] A. Bjarklev, J. Broeng, and A. S. Bjarklev, *Photonic crystal fibres* (Kluwer Academic Publishers, Boston, MA, 2003).

[11] J. D. Jackson, *Classical Electrodynamics* (John Wiley, New York, 1975).

[12] C. Kittel, *Solid State Physics* (John Wiley and Sons, New York, 1986).

[13] K. Busch and S. John, "Photonic band gap formation in certain self-organizing systems", Phys. Rev. E **58**, 3896, (1998).

[14] A. Mekis, J.C. Chen, I. Kurland, S. Fan, P.R. Villeneuve and J.D. Joannopoulos, "High transmission through sharp bends in photonic crystal waveguides", Phys. Rev. Lett. **77**, 3787 (1996).

[15] S. Fan, P.R. Villeneuve and J.D. Joannopoulos, "Channel drop tunneling through localized states", Phys. Rev. Lett. **80**, 960 (1998).

[16] S.G. Johnson, C. Manalatou, S. Fan, P.R. Villeneuve, J.D. Joannopoulos and H.A. Haus, "Elimination of cross talk in waveguide intersections." Opt. Lett. **23**, 1855 (1998).

[17] S.H. Fan, S.G. Johnson, J.D. Joannopoulos, C. Manalatou and H.A. Haus, "Waveguide branches in photonic crystals." J. Opt. Soc. Am. B **18**, 162 (2001).

[18] A. Talneau, Ph. Lalalnne, M. Agio and C.M. Soukoulis, "Low reflection photonic crystal taper for efficient coupling between guide sections of arbitrary widths", Opt. Lett. **27**, 1522 (2002)

[19] J. Vuckovic, M. Loncar, H. Mabuchi and A. Scherer, "Design of photonic crystal microcavities for cavity QED," Phys. Rev. E **65**, 016608 (2001).

[20] Y. Akahane, T. Asano, B.-S. Song and S. Noda, "Fine-tuned high-Q photonic-crystal nanocavity," Opt. Express **13**, 1202 (2005)

[21] J. C. Knight, J. Broeng, T.A. Birks and P. St. J. Russell, "Photonic band gap guidance in optical fibers," Science **282**, 1476 (1998).

[22] P. St. J. Russell, "Photonic crystal fibers", Science **299**, 358 (2003).

[23] Y.A. Vlasov, X.-Z. Bo, J.C. Sturm and D.J. Norris, "On-chip Natural Assembly of Silicon Photonic Band Gap Crystals", Nature (London) **414**, 289, (2001)

[24] S.H. Park and Y. Xia, "Assembly of Mesoscale Particles over Large Areas and Its Application in Fabricating Tunable Optical Filters", Langmuir **15**, 266 (1999)

[25] J.C. Knight, T.A. Birks, P. St. J. Russell and D.M. Atkin, "All-Silica Single-Mode Fiber with Photonic Crystal Cladding", Opt. Lett. **21**, 1547 (1996)

[26] D. Almalawi, K.A. Bosnick, A. Osika and M. Moskovits, "Fabrication of Nanometer-Scale Patterns by Ion-Milling with Porous Anodic Alumina Masks", Adv. Mater. **12**, 1252 (2000)

[27] H. Masuda and K. Fukuda, "Ordered Metal Nanohole Arrays Made by a Two-Step Replication of Honeycomb Structures of Anodic Alumina", Science, **268**, 1466 (1995)

[28] H. Masuda, M. Ohya, K. Nishio, H. Asoh, M. Nakao, M. Nohtomi, A. Yokoo and Toshiaki Tamamura, "Photonic Band Gap in Anodic Porous Alumina with Extremely High Aspect Ration Formed in Phosphoric Acid Solution", Jpn. J. Appl. Phys. **39**, L1039(2000)

[29] P. Hoyer, N. Baba and H. Masuda, "Small Quantum-Sized CdS Particles Assembled to Form a Regularly Nanostructured Porous Film", Appl. Phys. Lett. **66**, 2700 (1995)

[30] S. Shoji, and S. Kawata, "Photofabrication of Three-Dimensional Photonic Crystals by Multibeam Laser Interference into a Photopolymerizable Resin", Appl. Phys. Lett. **76**, 2668 (2000)

[31] R. Jakubiak, T.J. Bunning, R.A. Vaia, L.V. Natarajan and V.P. Tondiglia, "Electrically Switchable, One-dimensional Polymeric Resonators from Holographic Photopolymerization: A New Approach for Active Photonic Bandgap Materials", Adv. Mater. **15**, 241 (2003)

[32] M. M. Sigalas, C.T. Chan, K.M. Ho and C.M. Soukoulis, "Metallic photonic band-gap materials", Phys. Rev. B **52**, 11744, (1995)

[33] S. Fan, P.R. Villeneuve and J.D. Joannopoulos, "Large omnidirectional band gaps in metallodielectric photonic crystals", Phys. Rev. B **54**, 11245, (1994)

[34] E. R. Brown and O. B. McMahon, "Large electromagnetic stop bands in metallodielectric photonic crystals", Appl. Phys. Lett. **67**, 2138 (1995)

[35] D. F. Sievenpiper, M.E. Sickmiller and E. Yablonovitch, "3D Wire Mesh Photonic Crystals", Phys. Rev. Lett. **76**, 2480, (1996)

[36] J. S. McCalmont, M.M. Sigalas, G.Tuttle, K.M. Ho and C.M. Soukoulis, "A layer-by-layer metallic photonic band-gap structure", Appl. Phys. Lett. **68**, 2759 (1996)

[37] E. Özbay, B. Temelkuran, M. Sigalas, G.Tuttle, C.M. Soukoulis and K.M. Ho, "Defect structures in metallic photonic crystals", Appl. Phys. Lett. **69**, 3797 (1996)

[38] A. Kao, K.A. McIntosh, O.B. McMahon, R. Atkins and S. Verghese, "Calculated and measured transmittance of metallodielectric photonic crystals incorporating flat metal elements", Appl. Phys. Lett. **73**, 145 (1998)

[39] C. Jin, B. Cheng, B. Man, D. Zhang, S. Ban, B. Sun, L. Li, X. Zhang and Z. Zhang, "Two-dimensional metallodielectric photonic crystal with a large band gap", Appl. Phys. Lett. **75**, 1201 (1999)

[40] M. M. Sigalas, R. Biswas, K.M. Ho, C.M. Soukoulis and D.D. Crouch, "Waveguides in three-dimensional metallic photonic band-gap materials", Phys. Rev. B **60**, 4426, (1999)

[41] A. J. Ward, J.B. Pendry and W.J. Stewart, "Photonic dispersion surfaces", J. Phys.: Condens. Matter **7**, 2217 (1995)

[42] V. Kuzmiak, A.A. Maradudin and F. Pincemin, "Photonic band structures of two-dimensional systems containing metallic components", Phys. Rev. B **50**, 16835, (1994)

[43] T. Ito and K. Ssakoda, "Photonic bands of metallic systems. II. Features of surface plasmon polaritons", Phys. Rev. B **64**, 045117, (2001)

[44] D.F. Sievenpiper, M.E. Sickmiller, E. Yablonovitch, "3D wire mesh photonic crystals", Phys. Rev. Lett. **76**, 2480, (1996)

[45] J.S. McCalmont, M. Sigalas, G. Tuttle, K.M. Ho, C.M. Soukoulis, "A layer-by-layer metallic photonic band-gap structure", Appl. Phys. Lett. **68**, 2759 (1996)

[46] A Moroz, "Three-dimensional complete photonic-band-gap structure in the visible", Phys. Rev. Lett. **83**, 5274, (1999)

[47] F. Gadot, A. de Lustrac, J.M. Lourtioz, T. Brillat, A. Ammouche and E. Akmansoy, "High-transmission defect modes in two-dimensional metallic photonic crystals", J. Appl Phys. **85**, 8499 (1999).

[48] S. He, M. Popov, M. Qiu and C. Simovski, "An explicit method for the analysis of guided waves in a line defect channel in a photonic crystal", Microwave Opt. Techn. Lett. **25**, 236 (2000).

[49] D. Sievenpiper, Z. Lijun, R.F.J. Broas, N.G. Alexopolous and E. Yablonovitch, "High-impedance electromagnetic surfaces with a forbidden frequency band", IEEE Trans. Microwave Theory **47**, 2059 (1999).

[50] S. He, M. Popov, M. Qiu and C. Simovski, "The influence of the dielectric-air interface on the radiation pattern of an antenna in a metallic photonic bandgap structure in a dielectric host medium", Microwave Opt. Techn. Lett. **26**, 367 (2000).

[51] C.T. Chan, W.Y. Zhang, Z.L. Wang, X.Y. Lei, D. Zheng, W.Y. Tam and P. Sheng, "Photonic band gaps from metallo-dielectric spheres", Physica B **279**, 150 (2000).

[52] W.Y. Zhang, X.Y. Lei, Z.L. Wang, D. Zheng, W.Y. Tam, C.T. Chan and P. Sheng "Robust photonic band gap from tunable scatterers", Phys. Rev. Lett. **84**, 2853 (2000).

[53] T.W. Ebbesen, H.J. Lezec, H.F. Ghaemi, T. Thio and P.A. Wolff, "Extraordinary optical transmission through sub-wavelength hole arrays", Nature **391**, 667 (1998).

[54] S.C. Kitson, W.L. Barnes and J.R. Sambles, "Full Photonic Band Gap for Surface Modes in the Visible", Phys. Rev. Lett. **77**, 2670 (1996).

[55] T. Klar, M. Perner, S. Grosse, G. von Plessen, W. Spirkl and J. Feldmann, "Surface-Plasmon Resonances in Single Metallic Nanoparticles", Phys. Rev. Lett. **80**, 4249 (1998).

[56] H.R. Stuart, and D.G. Hall, "Absorption enhancement in silicon-on-insulator waveguides using metal island films", Appl. Phys. Lett. **69**, 2327 (1996).

[57] G. Sauer, G. Brehm, S. Schneider, K. Nielsch, R. B. Wehrspohn, J. Choi, H. Hofmeister, U. Gösele, "Highly ordered monocrystalline silver nanowire arrays", J. Appl. Phys. **91**, 3243 (2002)

[58] J. Choi, G. Sauer, K. Nielsch, R.B. Wehrspohn, U. Gösele, "Hexagonally Arranged Monodisperse Silver Nanowires with Adjustable Diameter and High Aspect Ratio" Chem. Mater. **15**, 776, (2003)

[59] K. Nielsch, R. B. Wehrspohn, S. F. Fischer, H. Kronmüller, J. Barthel, J. Kirschner, T. Schweinboeck, D. Weiss, U. Gösele, "High Density Hexagonal Nickel Nanowire Arrays with 65 and 100 nm-Periods", MRS Symp. Proc. **705**, Y9.3.1 (2002)

[60] K. Nielsch, R. B. Wehrspohn, J. Barthel, J. Kirschner, U. Gösele, T. Schweinboeck, D. Weiss, S. F. Fischer, H. Kronmüller, "High-density nickel nanowire array" J. Magn. Mater. Magn. **249**, 234 (2002)

Chapter 2

Optical Properties of Metals

This chapter will give a short introduction into the linear optical properties of metal nanostructures. The precise knowledge of these properties will be fundamentally important when dealing with more complex optical phenomena in the metallo-dielectric structures. The dielectric function and the bulk properties of metals are discussed. In addition to the Drude dielectric function, Drude-Lorentz dielectric function will be presented.

2.1 Optics of metals

Metals occupy a significant fraction of the periodic table. Despite of high reflection, metals are still an attractive material in optics. It is not surprising that a lot of research was devoted to understand and to use their optical properties.

As a first approximation, metal can be considered to be an isotropic medium of dielectric constant ε, permeability μ, and conductivity σ. Using the material equations for electric displacement field $\vec{D} = \varepsilon\vec{E}$, for magnetic flux density $\vec{B} = \mu\vec{H}$, and for the current density $\vec{J} = \sigma\vec{E}$ Maxwell's equations take the form [1]:

$$\nabla \times \vec{E} + \mu\frac{\partial \vec{H}}{\partial t} = 0, \tag{2.1}$$

$$\nabla \times \vec{H} - \varepsilon\frac{\partial \vec{E}}{\partial t} = \sigma\vec{E}, \tag{2.2}$$

$$\nabla \cdot \vec{E} = \frac{\rho}{\varepsilon}, \text{ and} \tag{2.3}$$

$$\nabla \cdot \vec{H} = 0. \tag{2.4}$$

Here $\vec{E}$ is the electric field, $\vec{H}$ is the magnetic field, μ is magnetic permeability, e is dielectric permittivity, σ is the conductivity and ρ is the charge density.

By considering monochromatic light $\vec{E} = \vec{E}_0 e^{-i\omega t}$, $\vec{H} = \vec{H}_0 e^{-i\omega t}$ and assuming the plane-wave solution, the wave equation for a metal can be written:

$$\nabla^2\vec{E} + \hat{k}^2\vec{E} = 0, \tag{2.5}$$

where

$$\hat{k}^2 = \omega^2 \mu \left(\varepsilon + i \frac{\sigma}{\omega} \right). \tag{2.6}$$

The complex dielectric constant is defined as:

$$\hat{\varepsilon} = \varepsilon + i \frac{\sigma(\omega)}{\omega} = \varepsilon_r + i\varepsilon_i \text{ with } \sigma(\omega) = \frac{\sigma_0}{1 - i\omega\Gamma}. \tag{2.7}$$

Here $\sigma(\omega)$ is AC conductivity, σ_0 is the conductivity measured with DC electric field and Γ is the damping constant.

In addition to the complex wave number $\hat{k}$ and a complex dielectric constant $\hat{\varepsilon}$, the complex refractive index $\hat{n}$ can also to be defined:

$$\hat{n} = n + i\kappa, \tag{2.8}$$

where n is the refractive index and κ is known as extinction coefficient.

Refractive index and dielectric constant are linked trough the following relations:

$$\hat{\varepsilon} = \hat{n}^2, \quad \varepsilon_r(\omega) = n^2 - \kappa^2 \text{ and } \quad \varepsilon_i(\omega) = 2n\kappa. \tag{2.9}$$

Now the plane wave equation can be rewritten, taking into account the complex wave vector:

$$\vec{E} = \vec{E}_0 \exp\left(\frac{-2\pi\kappa x}{\lambda} \right) \exp\left[\left(\frac{-2\pi n x}{\lambda} - i\omega t \right) \right]. \tag{2.10}$$

here, $\lambda = \dfrac{2\pi c}{\omega n}$ is the wavelength of the radiation in the medium with refractive index n. In the equation (2.10) the first exponential is real and quantifies the absorption of the wave, the second part is imaginary, corresponding to the oscillatory part of the wave. A value for penetration depth, δ, can now be defined as the distance into a material the light has travelled when it reaches a field strength $1/e$ of its initial strength, this is also known as the skin depth.

$$\delta = \frac{\lambda}{2\pi\kappa}. \tag{2.11}$$

δ is usually a small fraction of the wavelength, especially for large conductivities. For instance, at a frequency 100GHz, the skin depth of a copper conductor ($\delta \approx 5 \times 10^{7} \Omega^{-1} m^{-1}$) is smaller than $1\mu m$ [2].

2.2 Drude model

In the previous section it was assumed that a metal's conductivity, dielectric constant and magnetic permeability were all constants; in reality these properties are dependent on the frequency of the incident light. This can be accounted for by calculating the frequency response of the dielectric constant, while the other properties can be considered constant over the spectral region of interest.

The dielectric constant of a medium is purely dependent on how the charges within the material respond to an optical field. In metals, unlike in a

dielectric, not all the electrons are bound to the atoms. Some electrons move freely between atoms and are said to be "free" electrons. In the absence of an electromagnetic field the free electrons have random motion and they do not give rise to a current flow. When an electric field is applied, free electrons are engaged in a more orderly motion. This motion of electrons gives rise to a current flow, and effect of the collisions with stationary atoms enters to the picture as a damping force opposite in direction and proportional to velocity of the electrons.

The equation of motion of an electron with velocity $\vec{v}$ in a material can be written as [3, 4]:

$$m\frac{d\vec{v}}{dt} + m\vec{v}\Gamma = -e\vec{E}, \qquad (2.12)$$

where m and e are the mass and the charge of the electron, respectively, and Γ is the damping constant referred to unit mass. Denoting by N the electron density in the metal, the instantaneous current density can be expressed in the form: $\vec{j} = -Ne\vec{v}$. In the harmonic regime, equation (2.12) thus leads to the following relations:

$$\vec{j}(\omega) = \sigma(\omega)\vec{E} = \frac{Ne^2}{m(\Gamma - i\omega)}\vec{E}_0 = \frac{Ne^2(\Gamma + i\omega)}{m(\Gamma + i\omega)}\vec{E}_0. \qquad (2.13)$$

Using the expression of the conductivity $\sigma(\omega)$ given in equation (2.7) the following equation yields the effective dielectric permittivity of the metals, known as Drude model, and any material that this model is applicable to it is called Drude-like material:

$$\varepsilon(\omega) = \varepsilon_\infty - \frac{\omega_p^2}{\omega(\omega + i\Gamma)}, \tag{2.14}$$

where ε_∞ is a dielectric constant at infinite frequency (usually equal to 1) ω_p represents the plasma frequency of the electron gas , as given by the equation:

$$\omega_p^2 = \frac{Ne^2}{m\varepsilon_0}. \tag{2.15}$$

The real and imaginary of part of Equation (2.14) are thus

$$\varepsilon_r(\omega) = \varepsilon_\infty - \frac{\omega_p^2}{(\omega^2 + \Gamma^2)}, \tag{2.16}$$

and

$$\varepsilon_i(\omega) = \frac{\omega_p^2 \Gamma}{\omega(\omega^2 + \Gamma^2)}. \tag{2.17}$$

In the optical region of high frequencies ranging from the near-infrared to the visible and ultraviolet, the parameters $\omega_p \Gamma$ and ω are ordered in a different manner, so that the following relation typically holds true: $\omega_p \approx \omega > \Gamma$. The equation (2.16) clearly evidences the role of the plasma resonance in the metal. From this point two different situations can be observed separately.

In the infrared and visible regions, the optical frequency is usually significantly lower than the plasma frequency. Since the $(-\omega_p^2/\omega^2)$ term is

predominant in the equation (2.16), the permittivity of the metal is a negative real number with a large modulus compared to unity and the refractive index will be a purely imaginary number of large amplitude. In other terms, metals remain good reflectors in these regions.

In the deep ultraviolet region, the optical frequency reaches at loast larger order than the plasma frequency, and therefore $\omega > \omega_p > \Gamma$. Accordingly, the permittivity of the metal will be presented by a real positive number smaller than unity. The metal thus tends to behave as a weakly absorbing dielectric and exhibit a permittivity smaller than the permittivity of vacuum. In Figure 2.1 the Drude model has been used to calculate the real and imaginary parts of $\varepsilon(\omega)$ for silver.

a)   b)
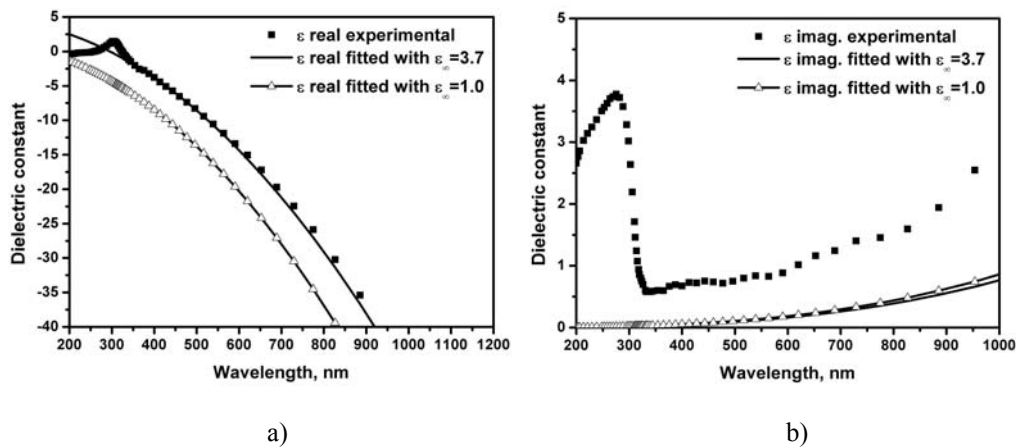
Figure 2.1. *(a)The real part of the dielectric function for silver. Experimental values from Palik et.al [5]. The theoretical values from Drude model using Eq. 2.16. (b) The imaginary part of dielectric function for silver. Experimental values from Palik et.al [5]. The theoretical values from Drude model using Equation 2.17.*

The parameters of $\omega_p = 9.2$ eV and $\Gamma = 0.016$eV were used to fit the experimental values from Ref. [5]. Qualitatively, the Drude model seems to work quite well,

although, some significant deviation is clearly observed for the imaginary part (Figure 2.1(b)).

This deviation is caused by the interband transitions which are neglected in this simple approach for obtaining the dielectric function of the metal. The influence of these interband transitions will be shortly discussed in the following section.

Table 2.1, taken from [6], list Drude free electron densities N and plasma frequencies for a number of common metals.

Table 2.1. Electron densities and plasma properties of some metals

Metal	N $(10^{28}m^{-3})$	$\omega_p/2\pi$ $(10^{15}\,Hz)$	λ_p (nm)
Ag	5.86	2.17	138
Al	18.1	3.82	79
Au	5.9	2.18	138
Cu	8.47	2.61	115

2.3 Influence of the interband transitions. Drude-Lorentz model

The Drude model implies that the only the plasma frequency should dictate the appearance of metals. This works for many metals. But does not explain why copper is red, gold is yellow and silver is colorless. In fact the appearance of these metals is characterized by an edge in the reflectance spectrum, similar to that predicted by the Drude model, but the problem is that all three
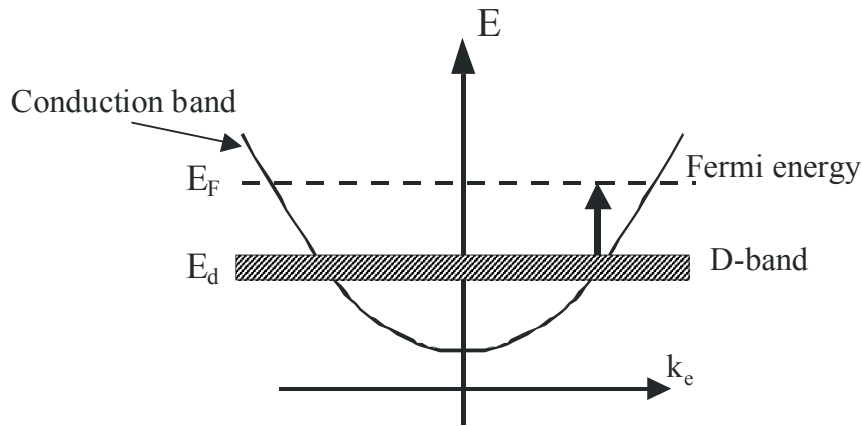
Figure 2.2. *Schematic example of the interband transitions*

metals have the same number of valence electrons, so the plasma frequency cannot in itself account for the colors of Cu, Ag and Au.

All three metals have filled D-shells [6]. The d-electron bands lie below the Fermi energy (Figure 2.2) of the conduction band. Transitions from the D-band to the empty states above the Fermi level can occur over a fairly narrow band of energies, around $\hbar\omega = E_F - E_d$ which can be modelled as an additional Lorentz oscillator. The combined effects of the free-electrons (Drude model) and the bound D-electrons (known as Lorentz model) influence the reflectance properties of the metal.

Therefore, in extension to the treatment of free conduction electrons, the complex dielectric function $\varepsilon(\omega)$ incorporating the interband transitions is given by [7]:

$$\varepsilon(\omega) = \varepsilon^{Drude}(\omega) + \varepsilon^{ib}(\omega).$$
(2.18)

a)   b)
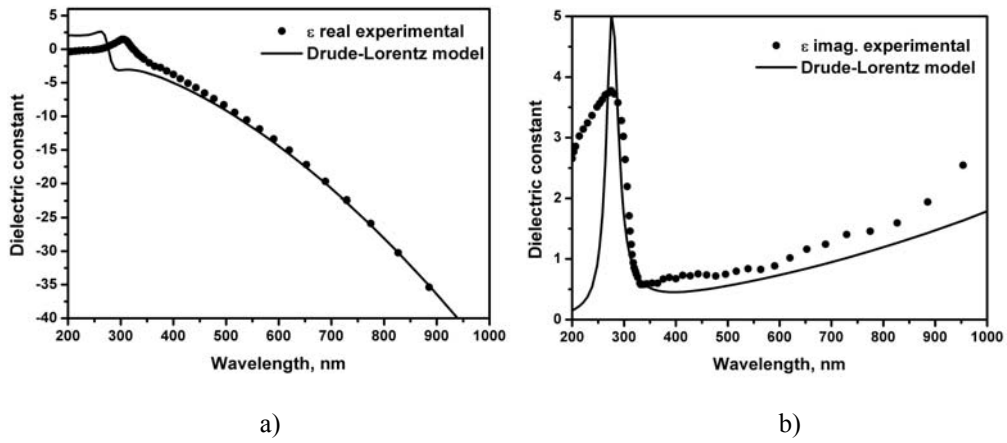
Figure 2.3. *(a)The real part of dielectric function for silver. Experimental values from Palik et.al [5]. The theoretical values from Drude-Lorentz model using Eq. 2.20 with three Lorentzian poles. (b) The real part of dielectric function for silver. Experimental values from Palik et.al [5].The theoretical values from Drude-Lorentz model using Eq. 2.20 with three Lorentzian poles [7].*

Here $\varepsilon^{ib}(\omega)$ denotes the contribution from the interband transitions. The analytical expression for the interband contributions can be derived, consisting of a sum of Lorentzian functions:

$$\varepsilon^{ib}(\omega) = \sum_{j}^{N} \frac{f_j}{\omega_j^2 - \omega^2 - i\omega\Gamma_j} , \qquad (2.19)$$

where f_j is known as oscillator strength.

Finally, the dielectric function of a metal can be written:

$$\varepsilon(\omega) = \varepsilon_{\infty} - \frac{\omega_p^2}{\omega^2 + i\omega\Gamma} + \sum_{j}^{N} \frac{f_j\omega_p^2}{\omega_j^2 - \omega^2 - i\omega\Gamma_j} . \qquad (2.20)$$

Here ε_∞ is a dielectric constant at infinite frequency, j is a number of oscillators with frequency ω_j.

The example of Drude-Lorentz model to fit the experimental results of silver is shown in Figure 2.3. Three Lorentzian poles from Ref. [7] were used in equation (2.20). This figure clearly demonstrates the better fitting over a wide range of wavelengths.

2.4 Surface plasmon polaritons

Many of the fundamental electronic properties of the solid state can be successfully described by single electrons moving in the periodic grating of atoms. Another approach is based on a plasma concept that assumes that free electrons of a metal are treated as an electron liquid of high density of about 10^{23} cm^{-3}, ignoring the lattice in a first approximation. From this approach, it follows that longitudinal density fluctuations, plasma oscillations, will propagate through the volume of the metal.

An important extension of the plasmon physics is the concept of "surface plasmons" (SP). Maxwell theory shows that electromagnetic surface waves can propagate along a metallic surface or on metallic films with a broad spectrum of eigenfrequencies from $\omega = 0$ up to $\omega = \omega_p/\sqrt{2}$ depending on the wavevector **k**. Their dispersion relation $\omega(\mathbf{k})$ lies to the right of the light line which means that the surface plasmon have a longer wavevector than light waves of the same energy $\hbar\omega$, propagating along the surface. Therefore they are called "nonradiative" surface plasmons, which describe fluctuations of the surface electron density. Their electromagnetic fields decay exponentially into the space

perpendicular to the surface and have their maximum in the surface, as is characteristic for surface waves. The excitation with light needs special light-plasmon couplers (grating couplers, prism couplers), since the dispersion relation lies to the right of the light line.

The electron charge oscillations on a metal boundary can perform coherent fluctuations which are called surface plasma oscillations [8, 9]. A schematic viev of such oscillations is shown in the left part of Figure 2.4.The longitudinal surface charge oscillations give rise to an electric field perpendicular to the interface which decays exponentially with distance (right part of Figure 2.4). This corresponds to an evanescent field above the surface with a decay length similar to that of the wavelength of light.
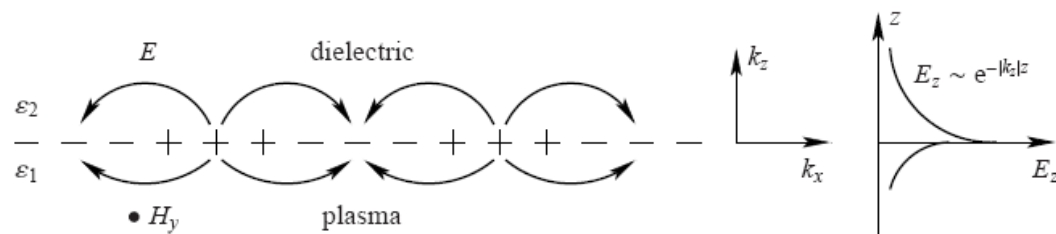
Figure 2.4. Shematic view of surface Plasmon polariton propagating on a surface in the x direction. The right panel displays the exponential decay of the field E_z.

The field distribution along the surface can be described by the following eexpression

$$E = E_0^{\pm} \exp\left[i\left(k_x x \pm k_z z - \omega t\right)\right], \tag{2.21}$$

with + for $z \geq 0$, − for $z \leq 0$. Here the evanescent decay of the fields in the z directio is caused by the imaginary wavevector k_z. The eigenfrequency ω of these

surface plasmon polaritons is directly connected with a complex wave vector $k_x = k'_x + ik''_x$ in the x direction. Theoretical calculations starting from Maxwell's equations with the assumption predict that the dispersion relation of surface plasmon polariton is then given by the equations [12]

$$k'_x = \frac{\omega}{c}\left(\frac{\varepsilon'_m \varepsilon_d}{\varepsilon'_m + \varepsilon_d}\right)^{1/2} \quad \text{and} \quad k''_x = \frac{\omega}{c}\left(\frac{\varepsilon'_m \varepsilon_d}{\varepsilon'_m + \varepsilon_d}\right)^{3/2}\frac{\varepsilon''_m}{2(\varepsilon'_m)^2}, \qquad (2.22)$$

where ε' and ε'' are real and imaginary parts of dielectric function of metal and ε_d is dielectric constant of the real, nonabsorptive dielectric material.
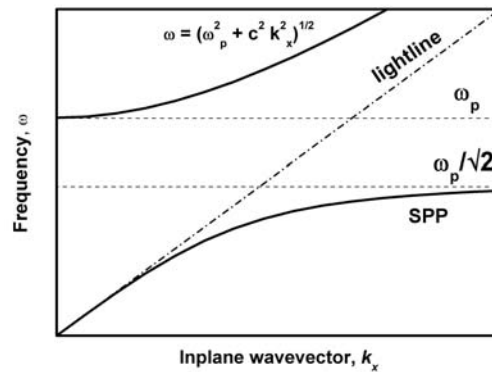
Figure 2.5. *The dispersion relation of a nonradiative surface plasmon polariton at a metañ-air interface. The dot-dashed line represents the air lightline (dispersion of light in air, $\omega = ck_x$). The dispersion of light in a free electron metal can be described by the relation $\omega = \sqrt{\omega_p^2 + c^2 k_x^2}$ and is plotted left to the lightline.*

The SPP dispersion relation, $\omega(k)$ plotted in Figure 2.5, shows that for small wave vectors the plasmon is close to that of the light line, but always to the right hand side. Therefore, the plasmon has similar properties to the optical field but always

has a greater momentum and is non-radiative. This increased momentum is associated with the binding of the mode to the surface. For larger wave vectors the surface plasmon dispersion tends towards a maximum value of $\omega_p/\sqrt{2}$.

Recent years have seen a strong revival of the interest in exploiting the properties of surface plasmon polaritons, motivated by the possibility they offer for realizing a strong spatial confinement of electromagnetic fields. Because SPs are surface-bound waves, light manipulation can be restricted to only two dimensions. This significantly simplifies the procedure, e.g. full band gaps are much easier to achieve in two dimensions. Two-dimensional SP photonic crystals exhibiting a plasmonic band-gap have been reported [10 -12]. Moreover, surface plasmon waveguiding in plasmonic crystals, enhanced optical transmission through nanosize holes, as well as light-controlled optical switching have been demonstrated [13, 14]. Many interesting "plasmon optical devices" were brought forward, for example waveguides [15, 16], mirrors [17], and a plasmon interferometer [18]. It is now widely expected that SPs will play an important role in future integrated nanooptical devices.

References

[1] M. Born and E. Wolf, *Principles of Optics (Cambridge University Press, 1999)*
[2] J.-M. Lourtioz, *Photonic crystals. Towards nanoscale photonic devices* (Springer, Berlin, 2005).

[3] C.F. Bohren and D.R. Huffman, *Absorption and Scattering of Light by Small Particles* (Wiley Interscience, New-York, 1983)

[4] U. Kreibig and M.D. Vollmer, *Optical Properties of Metal Clusters* (Springer, Berlin, 1995)

[5] E.D. Palik, *Handbook of Optical Constants of Solids* (Academic Orlando, Fla., 1985)

[6] M. Fox, *Optical Properties of Solids* (Oxford Master Series in Physics, 2002)

[7] A. D. Rakic, A. B. Djurisic, J. M. Elazar, and M. L. Majewski, "Optical Properties of Metallic Films for Vertical-Cavity Optoelectronic Devices", Appl. Opt. **37**, 5271 (1998)

[8] H. Raether, *Surface Plasmons on Smooth and Rough Surfaces and on Gratings* (Springer-Verlag, 1988).

[9] R. H. Ritchie, "Plasma Losses by Fast Electrons in Thin Films", Phys. Rev. **106,** 874 (1957).

[10] W. L. Barnes, T.W. Preist, S.C. Kitson, and J.R. Sambles, "Physical origin of photonic energy gaps in the propagation of surface plasmons on gratings", Phys. Rev. B **54**, 6227 (1996).

[11] S.I. Bozhevolnyi, J. Erland, K. Leosson, P.M.W. Skoglund, and J.M. Hvam, "Waveguiding in Surface Plasmon Polariton Band Gap Structures", Phys. Rev. Lett. **86**, 3008 (2001).

[12] L. Salomon, F. Grillot, F. de Fornel, and A.V. Zayats, "Near-field distribution of optical transmission of periodic subwavelength holes in a metal film", Phys. Rev. Lett. **86**, 1110 (2001).

[13] T.W. Ebbesen, H.J. Lezec, H.F. Ghaemi, T. Thio, and P.A. Wolff, "Extraordinary optical transmission through subwavelength hole arrays", Nature **391**, 667 (1998).

[14] I.I. Smolyaninov, A.V. Zayats, A. Stanishevsky, and C.C. Davis, "Optical control of photon tunneling through an array of nanometer-scale cylindrical channels", Phys. Rev. B **66**, 205414 (2002).

[15] J. –C. Weeber, J.R. Krenn, A. Dereux, B. Lamprecht, Y. Lacroute, and J.P. Goudonnet, "Near-field observation of surface plasmon polariton propagation on thin metal stripes", Phys. Rev. B **64**, 045411 (2001).

[16] C. Girard and R. Quidant, "Near-field optical transmittance of metal particle chain waveguides", Opt. Express **12**, 6141 (2004)

[17] S.I. Bozhevolnyi, F.A. Pudin, "Two-dimensional microoptics of surface plasmons", Phys. Rev. Lett. **78**, 2829 (1997).

[18] H. Ditlbacher, J.R. Krenn, G. Schider, A. Leitner, and F.R. Aussenegg, "Two-dimensional optics with surface plasmon polaritons", Appl. Phys. Lett. **81**, 1762 (2002).

Chapter 3

Numerical Methods

Theoretical calculations of photonic crystals are, in principle, exact, because Maxwell's equations are derived from first principles. Therefore, the power of computations is comparable to that of experiments in characterization of photonic crystals.

Fabrication processes of photonic crystals are expensive in general, especially in the optical and near-infrared regions of the spectrum. For this reason, it is important to start with a judicious design, taking into account fabrication tolerances. Such a design should be based on a rigorous modelling. Rules of thumb can provide only trends in photonic crystal properties, not exact numbers needed to embark into the fabrication.

The aim of this chapter is to present an overview of most common computational methods and modeling tools applicable to photonic crystals analysis and design.

Many numerical approaches have been proposed for the research of photonic band gap materials, for example, the transfer matrix method [1], scattering matrix method [2], plane wave expansion method [3], Finite difference time domain (FDTD) method [4], finite element method [5], etc. Among them, the plane wave expansion method and the FDTD method are the most popular numerical methods for photonic crystal analysis. The transfer matrix and the scattering matrix methods can be used to obtain the transmission spectrum for finite photonic crystals by calculating the respective matrices for each layer; the plane wave expansion method is a frequency domain method, and it can obtain the band structure and mode fields. FDTD is a time domain method, which can be used to study the dynamics of PBG devices. It was first introduced in PBG research just a few years ago and has been showing great promise to treat some complicated PBG structures, especially the dynamics of real PBG devices, which other methods are incapable of dealing with.

3.1 Plane-Wave Expansion Method

The plane wave expansion method (PWEM) consists in expanding the periodic functions in appropriate Fourier series and inserting the expansions into the wave equation [3]. The result is an infinite matrix-eigenvalue problem, which has to be truncated for numerical calculations. Through solving the eigenproblem one obtains the spectrum of eigenfrequencies (i.e. band structure) and expansion coefficients for the Bloch eigenmodes. PWEM has become the most popular method for analyzing photonic crystals.

Assuming that the electromagnetic filed has a harmonic time dependence $e^{i\omega t}$ the Maxwell curl equations in frequency domain can be written as:

$$\nabla \times \vec{E} = -i\omega\mu(\vec{r})\vec{H} \tag{3.1}$$

$$\nabla \times \vec{H} = i\omega\varepsilon(\vec{r})\vec{E}, \tag{3.2}$$

where $\vec{E}$ is the electric field, $\vec{H}$ is the magnetic field, ω is an angular frequency, $\mu(\vec{r})$ is magnetic permeability, and $\varepsilon(\vec{r})$ is dielectric, position dependent function of photonic crystal. Eliminating $\vec{E}$ the above equation can be further simplified to so-called "master equation":

$$\nabla \times \left(\frac{1}{\varepsilon(\vec{r})} \nabla \times \vec{H} \right) = \frac{\omega^2}{c^2} \vec{H}, \tag{3.3}$$

This is the eigenvalue equation where $c = 1/\sqrt{\mu_0 \varepsilon_0}$ is the speed of light in vacuum. Here the ε_0 and μ_0 are the permittivity and permeability of free space, respectively. Similar derivation can be obtained for $\vec{E}$ by eliminating $\vec{H}$. Because of the spatial periodicity of $\varepsilon(\vec{r})$ we can use the Bloch's theorem to expand the $\vec{H}$ field in the term of plane waves,

$$\vec{H}(\vec{r}) = \sum_{\vec{G}} \sum_{\lambda=1,2} h_{G,\lambda} \hat{e}_{\lambda} e^{i(\vec{k}+\vec{G})\cdot\vec{r}}, \tag{3.4}$$

where $\hat{e}_1$ and $\hat{e}_2$ are unit vectors chosen such that they are perpendicular to $\vec{k} + \vec{G}$ due to the transverse requirement (i.e. $\nabla \cdot \vec{H} = 0$). By substituting equation (3.4) into equation (3.3) we will obtain, after some algebra, the following expression

$$\left|\vec{k} + \vec{G}\right|\left|\vec{k} + \vec{G}'\right|\varepsilon^{-1}(\vec{G} - \vec{G}')\begin{pmatrix} \hat{e}_2 \cdot \hat{e}_2' & -\hat{e}_2 \cdot \hat{e}_1' \\ -\hat{e}_1 \cdot \hat{e}_2' & \hat{e}_1 \cdot \hat{e}_1' \end{pmatrix}\begin{pmatrix} \vec{h}_1' \\ \vec{h}_2' \end{pmatrix} = \frac{\omega^2}{c^2}\begin{pmatrix} \vec{h}_1 \\ \vec{h}_2 \end{pmatrix}, \qquad (3.5)$$

This is the standard eigenvalue problem that can be written in the matrix form

$$\begin{bmatrix} M_1 & M_2 \\ M_3 & M_4 \end{bmatrix}\begin{bmatrix} h_1(\vec{G}') \\ h_2(\vec{G}') \end{bmatrix} = \frac{\omega^2}{c^2}\begin{bmatrix} h_1(\vec{G}) \\ h_2(\vec{G}) \end{bmatrix}, \qquad (3.6)$$

For N plane waves used the will be a $2N$ linear equations.

The periodic dielectric function in the equation (3.3) can be expanded in a Fourier series of plane waves as follows:

$$\frac{1}{\varepsilon(\vec{r})} = \sum_{\vec{G}} \hat{\kappa}(\vec{G})e^{i\vec{G}\vec{r}}, \qquad (3.7)$$

where the Fourier coefficients $\hat{\kappa}(\vec{G})$ are obtained through an integration over the primitive unit cell.

For two-dimensional problem the simplification can be made. Assuming that dielectric function is invariant in the z direction the equation (3.5) is decomposed into TE (E_x, E_y, H_z) and TM (H_x, H_y, E_z) polarizations.

For TE polarization we will get the following expression:

$$\sum_{\vec{G}} \left(\vec{k} + \vec{G}\right) \cdot \left(\vec{k} + \vec{G}\right) \varepsilon^{-1}(\vec{G} - \vec{G}')h_G = \frac{\omega^2}{c^2} h_G , \tag{3.8}$$

and for TM polarization we will get:

$$\sum_{\vec{G}} \left|\vec{k} + \vec{G}\right| \varepsilon^{-1}(\vec{G} - \vec{G}')\left|\vec{k} + \vec{G}'\right|e_G = \frac{\omega^2}{c^2} e_G , \tag{3.9}$$

The above equations (3.8, 3.8) can be solved using standard matrix-diagonalization methods. For different wavevectors $\vec{k}$, one can obtain a series of eigenfrequencies ω, which compose the band structures of photonic crystals.

3.1.1 Drude model implementation for the Plane-Wave Expansion Method

In 1994 Maradudin et al. [4] proposed the extension of the PWEM. This extension allows modeling the dielectrics that depend on the frequency. In his paper Maradudin et al. used Drude model in the form $\varepsilon(\omega) = \varepsilon_\infty - \omega_p^2 / \omega^2$, where $\varepsilon_\infty = 1$ and the dielectric constant of background was air. In this subchapter we are extending the model of Maradudin in order to model metallic photonic crystals embedded into background with dielectric constant different from the air and with $\varepsilon_\infty \neq 1$. The procedure of implementation of Drude media into PWEM is similar to dielectric one, the only difference is frequency dependence dielectric

function. Only TM polarization (electric field parallel to the rods)will be considered since PWEM for TE polarization does not reproduce results correctly.

In the case of TM polarization the Maxwell curl equations for the three nonzero components (H_x, H_y, E_z) are

$$\frac{\partial \vec{H}_y(\vec{r})}{\partial x} - \frac{\partial \vec{H}_x(\vec{r})}{\partial y} = -i\frac{\omega}{c}\varepsilon(\vec{r})\vec{E}(\vec{r}), \tag{3.10}$$

$$\frac{\partial \vec{E}_z(\vec{r})}{\partial x} = -i\frac{\omega}{c}\vec{H}_y(\vec{r}), \tag{3.11}$$

$$\frac{\partial \vec{E}_z(\vec{r})}{\partial y} = i\frac{\omega}{c}\vec{H}_x(\vec{r}), \tag{3.12}$$

After arranging the above equations by eliminating H_x, H_y, we obtain the equation satisfied by E_z

$$\frac{1}{\varepsilon(\vec{r})}\left[\frac{\partial^2}{\partial x^2} + \frac{\partial^2}{\partial y^2}\right]\vec{E}_z(\vec{r}) + \frac{\omega^2}{c^2}\vec{E}_z(\vec{r}) = 0, \tag{3.13}$$

To solve the equation (3.13) we expand $\dfrac{1}{\varepsilon(\vec{r})}$ and $\vec{E}_z(\vec{r})$ according to

$$\frac{1}{\varepsilon(\vec{r})} = \sum_{\vec{G}} \hat{\kappa}(\vec{G})e^{i\vec{G}\vec{r}}, \tag{3.14}$$

$$\vec{E}_z(\vec{r}) = \sum_{\vec{G}} e_G e^{i(\vec{k}+\vec{G})\cdot\vec{r}}, \tag{3.15}$$

In general case of metal rods of arbitrary cross section, the Fourier coefficients $\kappa(\vec{G})$ are given by the following expressions:

$$\hat{\kappa}(\vec{G}) = \begin{cases} \dfrac{1}{\varepsilon_b} + \dfrac{f\omega^2(\varepsilon_b - \varepsilon_\infty) - f\omega_p^2}{\omega^2\varepsilon_b\varepsilon_\infty - \omega_p^2\varepsilon_b}, & \text{if } \vec{G} = 0 \\[4mm] \left(\dfrac{\omega^2(\varepsilon_b - \varepsilon_\infty) - \omega_p^2}{\omega^2\varepsilon_b\varepsilon_\infty - \omega_p^2\varepsilon_b}\right)\dfrac{1}{a_c}\int d^2 r e^{-i\vec{G}\cdot\vec{r}}, & \text{if } \vec{G} \neq 0 \end{cases}, \qquad (3.16)$$

where f is the filling fraction, i.e. the fraction of the total volume occupied by the rods. It is given by $f = a_r/a_c$, where a_r is the cross-sectional area of the rod and a_c is the unit cell area.

By substituting equations (3.14) and (3.15) into equation (3.13) we obtain the following equation for TM polarization:

$$\sum_{\vec{G}} \hat{\kappa}(\vec{G} - \vec{G}')\left|\vec{k} + \vec{G}'\right|^2 e_G = \frac{\omega^2}{c^2} e_G, \qquad (3.17)$$

The equation (3.17) has the form of a standard eigenvalue problem and can be solved by using diagonalization methods.

3.2 Finite-Difference Time-Domain Method

Very generally speaking, a FDTD-program consists of four fundamental building blocks: first, the spatial definition of the system with a distribution of dielectric or magnetic materials and the choice of a proper termination of the

calculation space, the boundary conditions. Second, the core algorithm that calculates the electromagnetic fields at each spatial discretisation point and timestep. Third, an exciting source of some kind and fourth, routines for data extraction, especially when not only the fields but also derived quantities like energy are of interest. The structures of the different building blocks are closely related to each other depending on the problem under consideration. E.g. the use of anisotropic materials requires a special form of the core algorithm, periodic (Bloch) boundaries require complex fields in all other building blocks and so on.

3.2.1 Finite-Difference Equations and the Yee Algorithm

Our aim is to solve the time dependent curl Maxwell equations:

$$\nabla \times \vec{E}(\vec{r},t) = -\frac{\partial \vec{H}(\vec{r},t)}{\partial t}, \tag{3.18}$$

$$\nabla \times \vec{H}(\vec{r},t) = \varepsilon(\vec{r})\frac{\partial \vec{E}(\vec{r},t)}{\partial t}. \tag{3.19}$$

Or in vector components:

$$\frac{\partial H_x(\vec{r},t)}{\partial t} = \frac{\partial E_y(\vec{r},t)}{\partial z} - \frac{\partial E_z(\vec{r},t)}{\partial y}, \tag{3.20}$$

$$\frac{\partial H_y(\vec{r},t)}{\partial t} = \frac{\partial E_z(\vec{r},t)}{\partial x} - \frac{\partial E_x(\vec{r},t)}{\partial z}, \tag{3.21}$$

$$\frac{\partial H_z(\vec{r},t)}{\partial t} = \frac{\partial E_x(\vec{r},t)}{\partial y} - \frac{\partial E_y(\vec{r},t)}{\partial x}, \tag{3.22}$$

$$\frac{\partial E_x(\vec{r},t)}{\partial t} = \frac{1}{\varepsilon(\vec{r})}\left(\frac{\partial H_z(\vec{r},t)}{\partial y} - \frac{\partial H_y(\vec{r},t)}{\partial z}\right), \tag{3.23}$$

$$\frac{\partial E_y(\vec{r},t)}{\partial t} = \frac{1}{\varepsilon(\vec{r})}\left(\frac{\partial H_x(\vec{r},t)}{\partial z} - \frac{\partial H_z(\vec{r},t)}{\partial x}\right), \tag{3.24}$$

$$\frac{\partial E_z(\vec{r},t)}{\partial t} = \frac{1}{\varepsilon(\vec{r})}\left(\frac{\partial H_y(\vec{r},t)}{\partial x} - \frac{\partial H_x(\vec{r},t)}{\partial y}\right). \tag{3.25}$$

Now we have to divide the continuous space and time into discrete grid cells and replace spatial and temporal derivatives by finite differences on this discrete mesh. We define the spatial grid as:

$$\vec{r} = (x,y,z) \rightarrow (i\Delta x, j\Delta y, k\Delta z), \tag{3.26}$$

for the general three dimensional case and the time dimension as

$$t \rightarrow n\Delta t, \tag{3.27}$$

Δx, Δy, Δz and Δt are the discretisation steps and i, j, k are the integer coordinates within the discrete mesh, and n is the timestep index. The vector components of the fields are therefore denoted as, e.g.

$$H_x(\vec{r},t) = H_x\big|_{i,j,k}^{n}. \tag{3.28}$$

The idea of Yee was to take advantage of the special nature of Maxwell's curl equations to improve accuracy by a factor of two by changing the spatial localization of the field components in the following way:

$$E_x[i\Delta x, j\Delta y, k\Delta z] \rightarrow E_x\left[\left(i+\frac{1}{2}\right)\Delta x, j\Delta y, k\Delta z\right], \tag{3.29}$$

$$E_y[i\Delta x, j\Delta y, k\Delta z] \rightarrow E_y\left[i\Delta x, \left(j+\frac{1}{2}\right)\Delta y, k\Delta z\right], \tag{3.30}$$

$$E_z[i\Delta x, j\Delta y, k\Delta z] \rightarrow E_z\left[i\Delta x, j\Delta y, \left(k+\frac{1}{2}\right)\Delta z\right], \tag{3.31}$$

$$H_x[i\Delta x, j\Delta y, k\Delta z] \rightarrow H_x\left[i\Delta x, \left(j+\frac{1}{2}\right)\Delta y, \left(k+\frac{1}{2}\right)\Delta z\right], \tag{3.32}$$

$$H_y[i\Delta x, j\Delta y, k\Delta z] \rightarrow H_y\left[\left(i+\frac{1}{2}\right)\Delta x, j\Delta y, \left(k+\frac{1}{2}\right)\Delta z\right], \tag{3.33}$$

$$H_z[i\Delta x, j\Delta y, k\Delta z] \rightarrow H_z\left[\left(i+\frac{1}{2}\right)\Delta x, \left(j+\frac{1}{2}\right)\Delta y, k\Delta z\right]. \tag{3.34}$$

In the curl expressions this means that the neighboring components that are needed to calculate the derivative are only 0.5 steps away and the linearization is

only done over a one step interval. As **E**-fields only depend on **H**-fields and vice versa, the same can be done in time, shifting **E**-fields $0.5\Delta t$ relative to the **H**-fields. The resulting equations are therefore:

$$
\frac{H_x\big|_{i,j+\frac{1}{2},k+\frac{1}{2}}^{n+\frac{1}{2}}}{\Delta t} = \frac{H_x\big|_{i,j+\frac{1}{2},k+\frac{1}{2}}^{n-\frac{1}{2}}}{\Delta t} + \frac{E_y\big|_{i,j+\frac{1}{2},k+1}^{n} - E_y\big|_{i,j+\frac{1}{2},k}^{n}}{\Delta z} - \frac{E_z\big|_{i,j+1,k+\frac{1}{2}}^{n} - E_y\big|_{i,j,k+\frac{1}{2}}^{n}}{\Delta y} \ ,
$$

$$(3.35)$$

$$
\frac{H_y\big|_{i+\frac{1}{2},j,k+\frac{1}{2}}^{n+\frac{1}{2}}}{\Delta t} = \frac{H_y\big|_{i+\frac{1}{2},j,k+\frac{1}{2}}^{n+\frac{1}{2}}}{\Delta t} + \frac{E_z\big|_{i+1,j,k+\frac{1}{2}}^{n} - E_z\big|_{i,j,k+\frac{1}{2}}^{n}}{\Delta x} - \frac{E_x\big|_{i+\frac{1}{2},j+1,k}^{n} - E_x\big|_{i+\frac{1}{2},j,k}^{n}}{\Delta z} \ ,
$$

$$(3.36)$$

$$
\frac{H_z\big|_{i+\frac{1}{2},j+\frac{1}{2},k}^{n+\frac{1}{2}}}{\Delta t} = \frac{H_z\big|_{i+\frac{1}{2},j+\frac{1}{2},k}^{n+\frac{1}{2}}}{\Delta t} + \frac{E_x\big|_{i+\frac{1}{2},j+1,k}^{n} - E_x\big|_{i+\frac{1}{2},j,k}^{n}}{\Delta y} - \frac{E_y\big|_{i+1,j+\frac{1}{2},k}^{n} - E_y\big|_{i,j+\frac{1}{2},k}^{n}}{\Delta x} \ ,
$$

$$(3.37)$$

for **H**-fields components and

$$
\frac{E_x\big|_{i+\frac{1}{2},j,k}^{n}}{\Delta t} = \frac{E_x\big|_{i+\frac{1}{2},j,k}^{n-1}}{\Delta t} + \frac{1}{\varepsilon\big|_{i+\frac{1}{2},j,k}} \cdot \left(\frac{H_z\big|_{i+\frac{1}{2},j+\frac{1}{2},k}^{n+\frac{1}{2}} - H_z\big|_{i+\frac{1}{2},j-\frac{1}{2},k}^{n+\frac{1}{2}}}{\Delta y} - \frac{H_y\big|_{i+\frac{1}{2},j,k+\frac{1}{2}}^{n+\frac{1}{2}} - H_y\big|_{i+\frac{1}{2},j,k-\frac{1}{2}}^{n+\frac{1}{2}}}{\Delta z} \right) ,
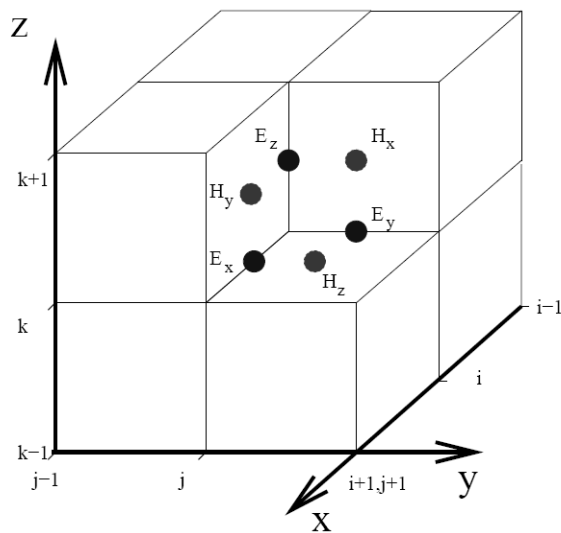$$

$$(3.38)$$

$$
\frac{E_y\Big|_{i,j+\frac{1}{2},k}^{n}}{\Delta t} = \frac{E_y\Big|_{i,j+\frac{1}{2},k}^{n-1}}{\Delta t} + \frac{1}{\varepsilon\Big|_{i,j+\frac{1}{2},k}} \cdot \left(\frac{H_x\Big|_{i,j+\frac{1}{2},k+\frac{1}{2}}^{n+\frac{1}{2}} - H_x\Big|_{i,j+\frac{1}{2},k-\frac{1}{2}}^{n+\frac{1}{2}}}{\Delta z} - \frac{H_z\Big|_{i+\frac{1}{2},j+\frac{1}{2},k}^{n+\frac{1}{2}} - H_z\Big|_{i-\frac{1}{2},j+\frac{1}{2},k}^{n+\frac{1}{2}}}{\Delta x} \right),
$$

$$
(3.39)
$$

$$
\frac{E_z\Big|_{i,j+\frac{1}{2},k}^{n}}{\Delta t} = \frac{E_z\Big|_{i,j+\frac{1}{2},k}^{n-1}}{\Delta t} + \frac{1}{\varepsilon\Big|_{i,j,k+\frac{1}{2}}} \cdot \left(\frac{H_y\Big|_{i+\frac{1}{2},j,k+\frac{1}{2}}^{n+\frac{1}{2}} - H_y\Big|_{i-\frac{1}{2},j,k-\frac{1}{2}}^{n+\frac{1}{2}}}{\Delta x} - \frac{H_x\Big|_{i,j+\frac{1}{2},k+\frac{1}{2}}^{n+\frac{1}{2}} - H_x\Big|_{i,j-\frac{1}{2},k+\frac{1}{2}}^{n+\frac{1}{2}}}{\Delta y} \right),
$$

$$
(3.40)
$$

for **E**-fields components. The arrangement of the shifted grids for each component is illustrated in Figure 3.1.

Figure 3.1. *Illustration of the spatial localization of the field components in a three dimensional Yee cell.*

3.2.2 Stability

Yee's algorithm is an explicit scheme, and to be stable, the size of the time step must be chosen in certain way. In fact, a well known rule [5] for stability of this scheme is

$$\Delta t \leq \frac{1}{c \sqrt{\left(\frac{1}{\Delta x}\right)^2 + \left(\frac{1}{\Delta y}\right)^2 + \left(\frac{1}{\Delta z}\right)^2}}. \qquad (3.41)$$

This is called the Courant condition. The c is the speed of light in vacuum. In order to understand this relationship the one-dimensional case is used here. A wave propagating in the vacuum covers the distance of a cell at a maximum speed c (the speed of light in a vacuum). In order to assure stability, Δt must be

$$\Delta t \leq \frac{\Delta x}{c}. \qquad (3.42)$$

This process can be characterised by a quantity S, where

$$S = \frac{\Delta t c}{\Delta x}, \qquad S \leq 1 \qquad (3.43)$$

This is called the Courant number. As has been already shown in [5], numerical instability is achieved if the minimum number of sampling points per wavelength

in the vacuum is ten, i.e. N_{vacuum} = 10. The number of sampling points in any medium is defined as N_λ. The latter is obtained as follows: the maximum speed of the waves propagating will depend on the dielectric constant of the media (ε), in fact the wavelength in the medium will be $\lambda_{medium} = \lambda_{vacuum}/\sqrt{\varepsilon}$, therefore the size of the spatial step in the medium must be $\Delta x = \lambda_{vacuum}/\sqrt{\varepsilon}\, N_{vacuum}$. Similarly the values of Δy and Δz can be calculated in this way. Once the spatial steps are calculated the next action is to compute the temporal step Δt, using equation (3.41).The accuracy of the discrete numerical scheme depends mainly on the discrete space and time steps. As a rule of thumb the smallest wavelength appearing in the calculations should be at least resolved with 12 numerical grid points.

3.2.3 Boundary Conditions

The computation space is divided into cells in the FDTD method and in every time step six new field values are being calculated at every cell. We can not extend the computation space to infinity, as this would require an infinite number of cells, which is impossible. In fact it is better to keep the computation space as small as possible. The smaller the computation space, the smaller the number of cells and the required CPU time to perform the calculations. When the computation space is truncated, it is going to have boundaries. Then, boundary conditions should be considered in the calculations. If the boundaries are chosen to be perfect electric conductors, it is sufficient to set the tangential electric field components at the boundary cells to zero in order to satisfy the PEC (perfect

electric conductor) boundary conditions. If the boundaries are chosen to be perfect magnetic conductors, it is sufficient to set the tangential magnetic field components at the boundary cells to zero in order to satisfy the PMC (perfect magnetic conductor) boundary conditions. But if the problem is to calculate scattering from a body in free space, then needed boundaries do not exist. So the solution is to set artificial boundaries such that the field will, as it propagates in free space, not reflect from them. In order to solve this problem, absorbing boundary conditions should be used.

Metallic Boundary Conditions

Metallic boundary conditions are a kind of Dirichlet boundary condition, where the values on the border of the simulation space are known. A metal surface with assumed perfect conductivity requires the transverse components of the electric field to be 0. This kind of boundary condition totally reflects electromagnetic waves, implying a phase shift of π on them. Only the electric field components along the border have to be set to 0 in the algorithm calculating the boundary values, and luckily these are the only ones which are accessed on the border by the core algorithm. The magnetic field positions outside do not have to be calculated as only the transverse electric field components on the border would rely on them but they are forced to be 0 anyway.

Bloch Boundary Conditions

For perfectly periodic systems (which means they are infinitely extended in the direction(s) of periodicity) we know from Bloch's theorem that

the field values at equivalent positions in different unit cells only differ by a phase factor. Numerically this has the consequence that we can describe the entire infinite system by just one unit cell and apply periodic boundaries that fulfill Bloch's theorem. We illustrate this for a one dimensional system extending in x-direction and bounded by $i=0$ and $i=i_{max}$. We know from the introduction of this section that we have to take special care of $E_y|_{i=0}$, $E_y|_{i=imax+1}$, $E_z|_{i=0}$ and $E_z|_{i=imax+1}$. If we assume a periodicity of length $i_{max}\Delta x$ we can relate the components at the boundaries by applying Bloch's theorem in the following way:

$$E_y\Big|_{i=0} = e^{+ik_x i_{\max}\Delta x} \cdot E_y\Big|_{i=i_{\max}}, \tag{3.44}$$

$$E_z\Big|_{i=0} = e^{+ik_x i_{\max}\Delta x} \cdot E_z\Big|_{i=i_{\max}}, \tag{3.45}$$

$$E_y\Big|_{i=i_{\max}+1} = e^{-ik_x i_{\max}\Delta x} \cdot E_y\Big|_{i=1}, \tag{3.46}$$

$$E_z\Big|_{i=i_{\max}+1} = e^{-ik_x i_{\max}\Delta x} \cdot E_z\Big|_{i=1}. \tag{3.47}$$

For the application of Bloch's theorem we have to introduce a wavevector k_x in the direction of periodicity. This is a parameter in the calculation and has to be given from the outside. The restriction to only one k-value is the price one has to pay for the benefit of limiting the computational domain to just one unit cell. Moreover, the phase factor in Bloch's theorem is complex, requiring complex electric and magnetic fields also. In practice this doubles the memory requirements of the calculation. The

generalization to three dimensions is straightforward but requires a wavevector with components in all space directions.

Mirror Boundary Conditions

Many structures possess mirror reflection symmetry with respect to a given symmetry plane, from which we can derive the mirror boundary conditions. One advantage of these mirror boundary conditions is that they can lead to reduction of the computational domain by a factor of 2 or even more. In particular, this can be very helpful for the 3D simulations, where limited computer memory often limits the size of structure that can be calculated. Also, the mirror boundary conditions can be used to resolve the degeneracy dictated by symmetry properties of the simulated structures.

Perfectly Matched Layers Boundary

In many cases it is desirable to simulate a structure embedded in infinitely extended free space because this is closest to most experimental situations. Numerically this means we have to define boundary conditions with the property that waves approaching the interfaces of the computational domain are completely absorbed without any spurious reflection back into the system. This has to be achieved for waves of arbitrary frequency and angle of incidence. There are several propositions in literature for addressing this task like Mur's boundary conditions [7] of first and second order or perfectly

matched layers (PML) invented by Berenger [8] in several variations. In this work we use the so-called convolution perfectly matched layers (CPML) boundary [9, 5]. The idea of PML boundaries is simple: we introduce a layer of a certain thickness *d* (in units of numerical discretisation points) consisting of an artificial conducting material that absorbs incoming waves. The absorbing layer is terminated by metallic boundaries that reflect the rests of the wave entirely and the wave is damped again on its way back. Only a vanishing part of the original amplitude reenters the calculation domain. The obvious difficulty that has to be solved is that for conventional absorbing materials there would be a partial reflection at the interface between the calculation volume and the absorbing material due to impedance mismatch. We have to choose the material properties therefore in a way that there is no impedance discontinuity for any frequency and angle of incidence.

3.2.4 The Drude Media in the FDTD

Electromagnetic simulation of dispersive media is vital in many applications and FDTD provides efficient means to model these media. The frequency dependence of material parameters causes dispersion and various methods have been used to model the frequency dependence of the material parameters in the FDTD method. The *recursive convolution* (RC) method [10, 11] and the *auxiliary differential equation* (ADE) method [12, 13] are the two most common approaches in this application.

The Recursive Convolution Method

Generally the constitutive relations for complex media are given in the frequency domain. As an example (with $e^{i\omega t}$ time harmonic convention)

$$\vec{D}(\omega) = \varepsilon_0 \varepsilon(\omega)\vec{E}(\omega),$$ (3.48)

$$\vec{B}(\omega) = \mu_0 \mu \vec{H}(\omega),$$ (3.49)

with constant permeability and frequency dependent complex permittivity. In order to construct the FDTD updating equations, time domain forms of the constitutive relations are needed together with Maxwell's curl equations. The product in Equation (3.48) will turn into a convolution as

$$\vec{D}(t) = \varepsilon_0 \varepsilon_\infty \vec{E}(t) + \varepsilon_0 \int_{\tau=0}^{t} \vec{E}(t-\tau')\chi_e(\tau')d\tau',$$ (3.50)

where ε_∞ is permittivity at infinite frequency and χ_e is electric susceptibility. The Equation (3.50) can be written in the discrete form as:

$$\vec{D}^n = \varepsilon_0 \varepsilon_\infty \vec{E}^n + \varepsilon_0 \sum_{m=0}^{n-1} \vec{E}^{n-m} \int_{m\Delta t}^{(m+1)\Delta t} \chi_e(\tau')d\tau'.$$ (3.51)

Where the continuous time function $\vec{E}$ is approximated by a constant value over each time step Δt. Using the definition $\chi_m = \int\limits_{m\Delta t}^{(m+1)\Delta t} \chi_e(\tau')d\tau'$ and $\Delta\chi_m = \chi_{m+1} - \chi_m$, the electric field component in the time discrete form can be written as

$$\vec{E}^{n+1} = \frac{\varepsilon_\infty}{\varepsilon_\infty + \chi_0}\vec{E}^n + \frac{1}{\varepsilon_\infty + \chi_0}\sum_{m=0}^{n-1}\vec{E}^{n-m}\Delta\chi_m - \frac{\Delta t}{\varepsilon_0(\varepsilon_\infty + \chi_0)}\nabla\times\vec{H}^{n+\frac{1}{2}}. \quad (3.52)$$

A new term ψ^n can be defined as

$$\psi^n = \sum_{m=0}^{n-1}\vec{E}^{n-m}\Delta\chi_m. \quad (3.53)$$

Where at this point the frequency dependent form of χ_e will be taken into account. Let χ_e be given by:

$$\chi_e(\omega) = -\frac{(\omega_p/\Gamma)}{1 + \omega/\Gamma}. \quad (3.54)$$

where ω_p is plasma frequency and Γ is the damping constant.

As for Drude media in the time domain χ_e will be:

$$\chi_e(t) = \frac{\omega_p^2}{v_c}\left(1 - e^{-t\Gamma}\right)U(t). \quad (3.55)$$

Then, after some manipulations ψ^n can be evaluated by a recursion relation called in [10] recursive accumulator. This is of the form

$$\psi^n = \vec{E}^n \Delta\chi_0 + e^{-\Delta t\Gamma}\psi^{n-1} . \qquad (3.56)$$

Equation (3.56) permits an efficient updating of the electric field without the need to explicitly evaluate the convolution sum embedded in Equation (3.51).

The Auxiliary Differential Equation (ADE) Method

The ADE method utilizes the time domain auxiliary differential equations linking the polarization and electric flux density [14, 15].

The goal of the ADE technique is to develop a simple time-stepping scheme for polarization current $\vec{J}_c$ which can be updated synchronously with the electric filed. A phasor polarization current is associated by

$$\breve{J}_c = i\omega\varepsilon_0 \left(\frac{\omega_p^2}{\omega^2 - i\omega\Gamma} \right) \breve{E} . \qquad (3.57)$$

After some manipulations we perform an inverse Fourier transform of each term of Equation (3.57) and integrating once with respect to time we obtain the following equation:

$$\frac{\partial \vec{J}_c}{\partial t} + \Gamma\vec{J}_c = \varepsilon_0 \omega_p^2 \vec{E} . \qquad (3.58)$$

Equation (3.58) is the required ADE for $\vec{J}_c$. This can be easily and accurately implemented in an FDTD code using semi-implicit scheme:

$$J_c^{n+1} = \frac{1 - \Gamma\Delta t/2}{1 + \Gamma\Delta t/2} J_c^n + \frac{\omega_p^2 \varepsilon_0 \Delta t/2}{1 + \Gamma\Delta t/2}\left(\vec{E}^{n+1} + \vec{E}^n\right). \quad (3.59)$$

Upon collecting like terms, we obtain the following explicit time-stepping relation for electric filed component:

$$\vec{E}^{n+1} = \frac{2\varepsilon_0\varepsilon_\infty - \Delta t\dfrac{\omega_p^2\varepsilon_0\Delta t/2}{1+\Gamma\Delta t/2}}{2\varepsilon_0\varepsilon_\infty + \Delta t\dfrac{\omega_p^2\varepsilon_0\Delta t/2}{1+\Gamma\Delta t/2}}\vec{E}^n + \frac{2\Delta t}{2\varepsilon_0\varepsilon_\infty + \Delta t\dfrac{\omega_p^2\varepsilon_0\Delta t/2}{1+\Gamma\Delta t/2}}\left(\nabla\times H^{n+\frac{1}{2}} - \frac{1}{2}\left[1 + \frac{1-\Gamma\Delta t/2}{1+\Gamma\Delta t/2}\right]J_c^n\right)$$

$$(3.60)$$

Thus the ADE-FDTD algorithm for modelling dispersive media with Drude model is a fully explicit procedure.

3.2.5 Advantage and Disadvantage

Advantages of FDTD:

1. FDTD uses no linear algebra. Being a fully explicit computation, FDTD avoids the difficulties with linear algebra.

2. FDTD is accurate and robust. The sources of error in FDTD calculations are well understood, and can be bounded to permit accurate models for a very large variety of electromagnetic wave interaction problems.

3. FDTD treats impulsive behavior naturally. A single FDTD simulation can provide either ultrawideband temporal waveforms or the sinusoidal steady state response at any frequency within the excitation spectrum.

4. FDTD treats nonlinear behavior naturally. Being a time domain technique, FDTD directly calculates the nonlinear response of an electromagnetic system.

5. FDTD is a systematic approach. With FDTD, specifying a new structure to be modeled is reduced to a problem of mesh generation rather than the potentially complex reformulation of an integral equation.

Disadvantages of FDTD:

The amount of computational resources required to simulate a particular problem. This is the major disadvantage of the FDTD method. In order to be confident you will get the right answer, 3D FDTD simulations must be large and slow. Large simulations come from the need to discretize at a fine spatial scale. Slow simulations come from a combination of simulation size (many grid points to be updated every timestep), the small timestep, and the need to run simulations for many optical cycles to attain high frequency resolution.

3.2.6 Methods for Photonic Band Structure Calculations

Order-N Method

To compute the eigenfrequencies the method called *Order-N* (also known as Ho method) (Chan et al. [16]) can be applied. The method is a combination of the

standard FDTD with complex fields and periodic boundary conditions (Equations (3.36- 3.39)). For the initial conditions a linear combination of a small number of plane waves $\vec{G}$ must be used:

$$\vec{H}(\vec{r}) = \sum_{\vec{G}} \left(\vec{v} \times (\vec{k} + \vec{G}) \right) \exp\left(i(\vec{k} + \vec{G}) \cdot \vec{r} \right). \tag{3.61}$$

This choice of initial condition will ensure that $\nabla \cdot \vec{H} = 0$ throughout the simulation. The $\vec{v}$ is a unit vector that controls the resulting polarization. For example, the $\vec{v} = (0,0,v_z)$ results in exciting the TM modes, while the choice of $\vec{v} = (v_x, v_y, 0)$ will excite the TE modes. In such a case we can selectively excite modes in 2D simulations.

The simulation is started with this setup and is run for a certain total simulation time T. Electromagnetic field components are recorded at several positions on the computational grid at every time step. These time series are Fourier transformed and the spectra are searched for peaks. The peaks that are still present in later times of the simulation belong to the eigenfrequencies of the periodic system. The necessity to predefine a certain wave vector to compute the periodic boundary condition in Equations (3.44)-(3.47) requires several simulation runs to cover enough points in reciprocal space for a band structure analysis.

The accuracy of the algorithm is limited by two factors, the length of the timestep Δt and the total simulation time T. Increasing the simulation time decreases the smallest detectable frequency as $\omega_{min} \sim 2\pi/T$ and similarly defining the frequency resolution. The time-step Δt is linked to the highest achieved frequency as $\omega_{max} \sim 2\pi/\Delta t$.

Virtual Dipole Method

Sakoda proposed the numerical method used to obtain band structures for photonic crystals is based on the approach developed on the FDTD method and the Green's function formalism [17]. In this method both electric and magnetic oscillating dipoles are embedded into the photonic crystal lattice.

We start from Maxwell's equations

$$\nabla \times \vec{E}(\vec{r},t) = -\frac{\partial}{\partial t}\left[\mu_0 \vec{H}(\vec{r},t) + \vec{P}_M(\vec{r},t)\right], \tag{3.62}$$

$$\nabla \times \vec{H}(\vec{r},t) = \frac{\partial}{\partial t}\left[\varepsilon_0 \varepsilon(\vec{r},\omega)\vec{E}(\vec{r},t) + \vec{P}_E(\vec{r},t)\right], \tag{3.63}$$

where $\vec{P}_M(\vec{r},t)$ and $\vec{P}_E(\vec{r},t)$ represent the polarization fields of the magnetic and electric virtual oscillating dipole, respectively. In the explicit form the polarisation fields can be expressed as

$$\vec{P}_E(\vec{r},t) = \vec{e}\,\delta(\vec{r}-\vec{r}_0)\exp(i\omega t), \tag{3.64}$$

$$\vec{P}_M(\vec{r},t) = \vec{h}\,\delta(\vec{r}-\vec{r}_0)\exp(i\omega t). \tag{3.65}$$

where $\vec{e}(\vec{r},t)$ and $\vec{h}(\vec{r},t)$ are the amplitudes of the electric and magnetic dipoles, $\vec{r}_0$ denotes their position within the photonic crystal and ω is the angular frequency of the oscillation; i refers to the imaginary unit and $\delta(\vec{r}-\vec{r}_0)$ denotes the Dirac delta function.

The electromagnetic energy density U emitted per unit time by the oscillating dipole placed at $\vec{r}_0$ within the photonic crystal lattice can be calculated by using the following expression [18]

$$U = \frac{1}{4}\left[\varepsilon(\vec{r},\omega)\cdot\vec{E}^2(\vec{r},t)+\vec{H}^2(\vec{r},t)\right]. \qquad (3.66)$$

The calculation procedure proceeds as follows: first, the wavevector is defined; second, the normal FDTD procedure is carrying out; third, the electromagnetic energy density is calculated from Equation (3.66) for the current angular frequency ω. After the finish of the calculation process one has the energy density distribution (U, ω) for all wavevectors. The resonance peaks of the energy density distribution (U, ω) give the eigenfrequencies. The eigenfrequencies can be obtained after sufficient cycles of oscillation of the dipole. Usually, 50 cycles are enough. Each cycle must be divided into 100-300 temporal points. The flow chart of the calculation process can be found in [19].

3.3 Other Numerical Methods

3.3.1 Finite Element Method (FEM)

The Finite Element Method (FEM or FE method) is a method originally developed for simulations in civil engineering. It is used for complex nonlinear analysis as well as static problems, e.g. for designing steel and concrete structures.

FEM is very well suited for calculations of photonic crystals due to its discretization method. FEM uses an unstructured mesh for representing the domain, which is broken down into many elements of simple shape and different size and orientation. A continuous domain is divided into a set of subdomains with a mesh consisting of triangles (Figure 3.2). Due to their different sizes these triangles match the form of the holes very well. The meshing grid, however, is not only limited to triangular shapes. Principally, it can have any given form, but for simplicity reasons it is advisable to use simple polygons. This kind of mesh brings up two main improvements with respect to e.g. a uniform Cartesian grid:

1) regions of arbitrary shape are represented better (no staircase approximation);

2) the FEM mesh can use locally a higher density of nodes in key regions that require it (e.g. narrow veins of high refractive index, typical in photonic crystals), without refining the discretization of the whole domain.

Moreover, since the discontinuous refractive index is handled in real space, FEM does not have the convergence problems of classical plane-wave method. Briefly, FEM goes as follows. Maxwell's equations are cast into a set of linear equations which approximate the field over an element: some interpolation function is chosen and its coefficients are computed for each element and stored as elemental matrices; these matrices are then assembled into global matrices that form an eigenvalue problem whose dimension depends on the number of elements. A detailed description of FEM technique applied to photonic crystals can be found in [6]. The eigenproblem matrices appearing in FEM are very sparse, leading to an algorithm complexity $O(N)$, where N is the number of degrees of freedom, proportional to the number of nodes. Despite this favorable scaling, FEM runs into trouble for large 3D domains, due to huge memory requirements. However,

FEM can be successfully applied for 2D finite-sized photonic crystals and 3D primitive-cell problems with Bloch boundary conditions.
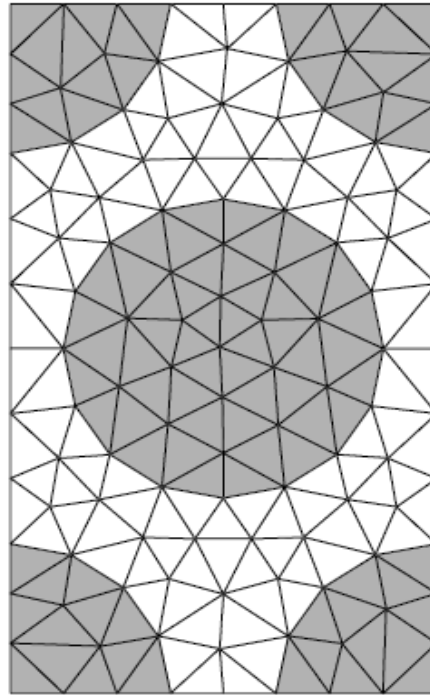
Figure 3.2. *The computational domain of the photonic crystal discretised with FEM mesh.*

3.3.2 Transfer Matrix Method (TMM)

This method has been introduced by Pendry and MacKinnon [1]. Instead of transforming to Fourier space, TMM is based on representing Maxwell's equations on a discrete lattice (Cartesian, in general) of real space points. The resulting discrete equations are recast into the form of a transfer matrix that connects the electric and magnetic fields in one layer of lattice points to those in

next layer. By taking products of transfer matrices one can find the fields at every point of the domain. But it is well-known that the multiplication of transfer matrices can suffer from serious numerical instabilities, due to exponentially growing terms. The solution to this problem is to divide the domain in "slices" thin enough so that these instabilities do not occur, then combine these slices using a stable recursion algorithm (e.g. scattering matrix). However, stability comes at the price of reduced speed, because the simple multiplication of sparse transfer matrices is replaced by a more involved recursion.

TMM yields the transmission spectrum directly (this can then be compared with experimental data) and Bloch wavevectors via the eigenvalues of the matrix. TMM uses a uniform Cartesian grid, but it can be better adapted by a coordinate transformation.

The original computer code developed by the group of John Pendry has been rewritten by Andrew Reynolds who added a graphical user interface, and is freely available under the name *"Translight"* [20].

3.3.3 Scattering Matrix Method (SMM)

The scattering matrix method (SMM) is used to analyze systems composed of a finite set of parallel circular cylinders [2]. In the SMM the source wave and the scattering objects are initially defined. The electromagnetic wave of light at an arbitrary position is subsequently calculated from the summation of two waves: the wave arriving directly from the source position and the wave that is scattered by other objects. Every scattered wave is represented in terms of cylindrical function expansion. The amplitude of each degree of cylindrical function, which

is excited by waves from source positions, is represented by the scattering matrix. The source position, the scattering matrix, and the scattered wave are related to each other in simultaneous equations, and the excited amplitudes are found by solving linear systems, immediately giving electromagnetic field distributions at arbitrary positions. The main limitations of the method are: it can be applied only to 2D photonic crystals; the objects must be isolated from each other and must be uniform; almost all calculations are restricted to objects with circular cross-section; and only static solutions of electromagnetic fields can be obtained.

3.3.4 Multiple Multipole Method (MMP)

The Multiple Multipole (MMP) method is a well established numerical technique for solving time-harmonic 2D scattering problems [21]. It belongs to the group of generalized multipole techniques. The unknown fields within individual domains are approximated by a set of expansion functions representing analytical solutions of Maxwell equations. Typical expansions for the field inside a domain are Bessel-type, whereas Hankel-type expansions are used outside. The system is solved by means of the least squares technique, which is numerically equivalent to an error minimization technique and is solved using orthogonal matrix triangulation. On the boundary points the errors are calculated as the mismatch of the analytical field description between the field inside and outside of the domain. This method involves a large number of multipoles, especially when the problem is not periodic, as it is the case with open structures. The setting of the multipoles and choosing their parameters is critical. The sizes of the structure are limited with the size of the overdetermined matrix. Therefore, this method is not applicable for simulations of large structures.

3.3.5 Korringa-Kohn-Rostoker Method (KKR method)

This method is adapted from Solid State Physics to calculate semiconductor electronic band structures. It was independently developed by Korringa [22] and Konh and Rostoker [23]. In the semiconductor case, the method begins with the integral form of the Schrödinger equation in terms of Green's functions. For photons the development is similar except for the complications brought about by the full vector character of electromagnetic fields. At some point in the calculations, it is assumed that vector field can be expanded, to a reasonable degree of accuracy, by a finite number of spherical harmonics.

The expansion of equations in terms of spherical harmonics is itself an advantage and a limitation at the same time. On the one hand, for systems made of spherical scatterers, the convergence of this method is very fast. Also, the discontinuities of the dielectric functions are accurately represented. On the other hand this method looses its effectiveness when scatterers are not spherical. For example, this method is ideal for colloidal crystals where ordered spheres are significantly apart from each other. However, for close packed arrangements where planes are much more interpenetrated or systems in which spheres are interpenetrated the spherical symmetry is lost. Another disadvantage is the lack of accuracy for high energy calculations.

A variation of this method called layer-KKR has been introduced to compute transmission and reflection spectra of finite (in the propagation direction) photonic crystals [24]

References

[1] J. B. Pendry and A. MacKinnon, "Calculation of photon dispersion relation", Phys. Rev. Lett. **69**, 2772 (1992).

[2] D. Felbacq et al., "Scattering by a random set of parallel cylinders," J. Opt. Soc. Am. A **11**, 2526 (1994)

[3] K. M. Leung, and M. Liu, "Photon band structures: the plane wave method", Phys. Rev. B. **41**, 10188 (1990).

[4] V. Kuzmiak, A.A. Maradudin, and F. Pinsemin, "Photonic band structures of two-dimensional systems containing metallic components", Phys. Rev. B **50**, 16835 (1994)

[5] A. Taflove ans S. Hagness, *Computational Electrodynamics. The finite-difference time-domain method* (Artech House, Boston, 2005).

[6] B.P. Hiett, *Photonic Crystal Modelling using Finite Element Analysis*, PhD Thesis, University of Southampton, Faculty of Engineering and Applied Science, 2002

[7] G. Mur, "Absorbing boundary conditions for the finite-difference approximation of the time-domain electromagnetic field equations", IEEE Trans. Electromagn. Compat. **23**, 377 (1981).

[8] J. P. Berenger, "A perfectly matched layer for the absorbtion of electromagnetic waves", J. Comput. Phys. **144**, 185 (1994).

[9] J. A. Roden and S. D. Gedeney, "Convolutional PML (CPML): An efficient FDTD implementation of the CFS-PML for arbitrary media", Microwave Opt. Technol. Lett. **27**, 334 (2000).

[10] K. Kunz and R. Luebbers, *The Finite Difference Time Domain method for Electromagnetics* (CRC Press, New York, 1993).

[11] A. Vial et al., "Improved analytical fit of gold dispersion: Application to the modeling of extinction spectra with a finite-difference time-domain method", Phys. Rev. B **71**, 085416, (2005)

[12] R. M. Joseph, et al., "Direct time integration of Maxwell's equations in linear dispersive media with absorption for scattering and propagation of femtosecond electromagnetic pulses", Opt. Lett. **16**, 1412- (1991)

[13] M. Okoniewski, and E. Okoniewska, "Drude dispersion in ADE FDTD revisited", Electron. Lett. **42**, 503, (2005).

[14] R. W. Ziolkowski and M. Tanaka, "Finite-difference time-domain modeling of dispersive-material photonic bandgap structures " J. Opt. Soc. Am. A **16**, 930 (1999)

[15] M. Han et al., "Model Dispersive Media in Finite-Difference Time-Domain Method With Complex-Conjugate Pole-Residue Pairs", IEEE Microw. Wireless Compon. Lett. **16**, 119 (2006).

[16] C. T. Chan, et al., "Order-N spectral method for electromagnetic waves", Phys. Rev. B **51**, 16635 (1995).

[17] K. Sakoda and J. Kawamata, "Novel approach to photonic bands with frequency-dependent dielectric constants" Opt. Express **3**, 12 (1998)

[18] J. D. Jackson, *Classical Electrodynamics* (John Wiley, New York, 1975).

[19] I. S. Maksymov, L. F. Marsal, M. A. Ustyantsev, and J. Pallarès, "Band structure calculation in two-dimensional Kerr non-linear photonic crystals", Opt. Commun. **248**, 469 (2005).

[20] A.L. Reynolds, Translight package, University of Glasgow (http://userweb.elec.gla.ac.uk/a/areynolds/). A. L. Reynolds . "Translight package", (2002).

[21] E. Moreno et al., "Band structure computations of metallic photonic crystals with the multiple multipole method", Phys. Rev. B **65**, 155120 (2002).

[22] J. Korringa, "On the calculation of the energy of a bloch wave in a metal", Physica **13**, 392 (1947).

[23] W. Kohn, and N. Rostoker, "Solution of the schrodinger equation in periodic lattices with an application to metallic lithium", Phys. Rev. **94**, 1111 (1954).

[24] A. Modinos et al., "Applications of the layer-KKR method to photonic crystals" Opt. Express **8**, 197 (2001).

Chapter 4

Effect of the Dielectric Background on Dispersion Characteristic of Metallo-Dielectric Photonic Crystals

In this chapter we theoretically study the effect of the dielectric background in two-dimensional metallo-dielectric photonic crystals. Two lattices we considered. The metallo-dielectric photonic crystal consists of a square lattice of circular metallic rods and triangular lattice with square rod. We calculate the photonic band structure by means of the plane wave method and the frequency-dependent finite-difference time-domain method. The transfer matrix method is used to obtain the reflectivity characteristics. Results show that the band structures shift toward lower frequencies and become flatter when the background dielectric constant increases. In addition, degeneracy can be broken and new gaps can be created in function of the dielectric background. For the case of square lattice we found that the relative band gap width $\Delta\omega/\omega_g$ grows with increasing background

dielectric constant and widths as large as 42.3 % and 13.8 % for the second and third band gaps can be achieved for $\varepsilon_b = 5$. We have investigated the origin of the new gap in these structures by studying the electric-field distribution at the band edges for the first five modes. For the triangular lattice we have found that the minimum background dielectric constant necessary to open an absolute photonic band gap is 1.6. The results show the possibility to achieve a relative band gap width larger than 10% for filling fractions away from the close packed condition for different backgrounds.

4.1. Introduction

Recently, great interest has been devoted to the study of two-dimensional metallo-dielectric photonic crystals (MDPCs) [1-5]. A MDPC is defined as a crystal such that a metallic material is periodically arranged in a dielectric background. Compared with dielectric photonic crystals MDPCs have some interesting properties. There is a cut-off frequency for TM polarization, i.e. there is a broad photonic band gap between zero frequency and the cut-off frequency. The inclusion of metallic components can enlarge the size of the gaps [6] and [7] and produce flat bands with very low group velocities related to the plasmon resonances can be achieved. Finally, these structures are interesting for different applications such as a practical filter [8-10], polarizer [11], or waveguide [12] and [13], in which the dimensions of metallic photonic crystals can be kept much smaller than the minimum dimensions needed for a typical dielectric photonic crystal. All these devices are based on metallic scatterers embedded into different dielectric substrates. From a practical point of view, metallic photonic crystals can be realized by electrochemical deposition of a Drude-like material into the holes

of a periodic structure of air holes in a dielectric [14] and [15].

Up to the present, a variety of numerical methods have been developed to study metallic and metallo-dielectric photonic crystals. For instance, Pendry et al. [16] calculated the transmission spectra by using the transfer matrix method (TMM). Kuzmiak et al. [17] used a modified plane wave method (PWM) to study two-dimensional photonic crystals composed of metallic cylinders with a dielectric constant of the Drude type metal. Nicorovici et al. [18] calculated band diagrams of two-dimensional arrays of perfectly conducting cylinders by a generalized Rayleigh identity method. Sakoda et al. [19] calculated the photonic bands of metallic systems by means of the numerical simulation of the dipole radiation based on the finite-difference time-domain method (FDTD). Later, Moreno et al. [20] the introduced multiple multipole method (MMP) to perform band structure computation of metallic photonic crystals. Arriaga et al. [21] calculated photonic band structures for idealized metals and other dispersive materials using an order-N scheme adapted to frequency-dependent dielectric functions. Recently, Takayma and Cada [22] reported theoretical results of metallic photonic crystals with circular rods embedded in anodic porous alumina. The calculations were performed using Translight package [23], which is based on the TMM. In most of the works dedicated to investigating metallic photonic crystals the background is usually air ($\varepsilon_b = 1$). The aim of the the present study is to investigate the effect of using different materials with different background dielectric constants on the photonic band structure and on the photonic bands of the MDPCs. We have used different methods: PWM and FDTD to determine the dispersion bands and TMM to determine the reflectivity characteristics. Only the E-polarization (TM modes) band gap is considered here since there is no band gap for the H-polarization (TE modes).

## 4.2 Method and Computational Model

The photonic crystal is composed of circular metallic rods in a square lattice with lattice constant a. The radius r of the rods is taken as $r = 0.472a$, which corresponds to a filling fraction of 70%. We have chosen this radius, because this structure shows the two largest band gaps for TM polarization and for air background [17]. The dielectric constant of the rods is given by the Drude model. In the simulation, ω_p has been fixed to $\omega_p a/2\pi c = 1.0$ in order to study only the influence of the background. The Drude dispersion relation is widely used to model the optical properties of the metals in the MDPCs [1, 19-22]. The value of the damping constant is kept deliberately small to $\gamma = 10^{-4}\omega_p$ because other authors [24] have demonstrated that the effect of such damping term is only to modify slightly the photonic band structure. Conversely, another work [25] shows that in some cases when the damping constant is big (as it happens for some metals) very strong effects can be observed, especially when flat bands related with plasmon resonances are considered. However, the study in this work focuses in the band gaps, which appear for the polarization where no flat bands are present. The dielectric constant of the background ε_b was varied from 1 (air) to 9 (alumina) and was frequency-independent. Although it is known that the dielectric constant of the possible materials suitable as background is not frequency-independent, we have taken it as constant as a first approximation because in the range of frequencies of practical interest the dielectric constant variation is reasonably small. The dispersion curves were calculated for three directions in the square two-dimensional Brillouin zone with highly symmetric points, Γ, X, M, whose coordinates are $(0, 0)$, $(\pi/a, 0)$, and $(\pi/a, \pi/a)$, respectively. The first

method for the computation of the photonic band structure is the plane wave method (PWM). The number of plane waves used in the expansion of the electromagnetic fields was 625. This number of plane waves is sufficient great to obtain a numerical error of less than 1% for the lowest 10 bands. The second method is the frequency-dependent finite-difference time-domain method ($(FD)^2TD$) [26-28] with Bloch's boundary conditions. All simulations were done using a spatial grid resolution 40×40 points per lattice constant, with 50 oscillation periods, and each period of oscillation was divided between 160 and 850 time steps, depending on the frequency range of interest. Finally, we calculated the reflectivity spectra of the studied metallo-dielectric photonic crystal using Translight package [23], which employs the transfer matrix method. From the calculated reflectance spectra, the band gaps of the studied structures can be obtained. The band gaps obtained by this method are used to check the results obtained with the PWM and the $(FD)^2TD$.

4.3 Results and discussion

Square lattice

Figure 4.1 (a) shows the photonic band structure for air background, $\varepsilon_b = 1$. The inset indicates the high symmetry points in the square lattice irreducible Brillouin zone and the structure under study. There are two band gaps – the large one between the zero frequency and the cut-off frequency defined by the first band (TM0-1) and a smaller one between the first and the second bands (TM1-2). The results obtained by $(FD)^2TD$ and PWM are in good agreement. These results are in good agreement with those obtained by Kuzmiak [17] and Sakoda [19], indicating that our implementation of these methods is correct. Figure 4.1 (b)
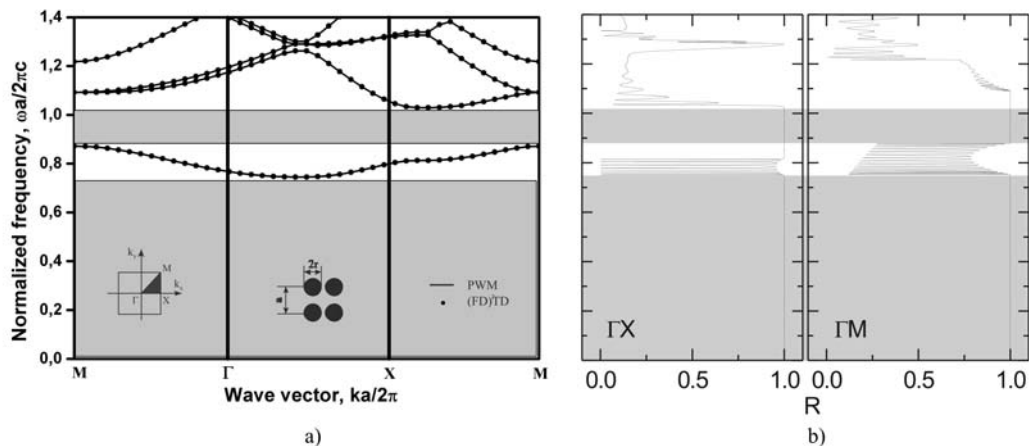
Figure 4.1. *a) Photonic band gap of metallic photonic crystal embedded in air (ε_b = 1). Ratio* r/a *= 0.472. Reflectivity spectra for the same photonic crystal for b) Γ-X direction and c) Γ-M direction. Shaded areas represent photonic band gaps.*

shows the reflectivity spectra obtained by TMM, for the two directions *ΓX* and *ΓM*. It can be seen that the same band gaps can be found as the intersection of the high-reflectivity regions.

Increasing the dielectric constant of the background leads to a different behavior of the photonic band structures. For instance, in Figure 4.2 (a), we show the photonic band structure for ε_b = 5. We can see that a new photonic band gap appears between the third and fourth bands (TM3-4). In addition, all photonic bands shift towards lower frequencies and consequently the cut-off moves to lower frequencies as well. Furthermore, the bands become flatter, which indicates that the group velocity associated to a band is lower. These results agree with those obtained by Takayma and Cada [22] and by Garcia et al. [29]. The results obtained with TMM indicate the same behavior (Figure 4.2 (b)). In order to explain this behavior we have examined how the field distribution of the
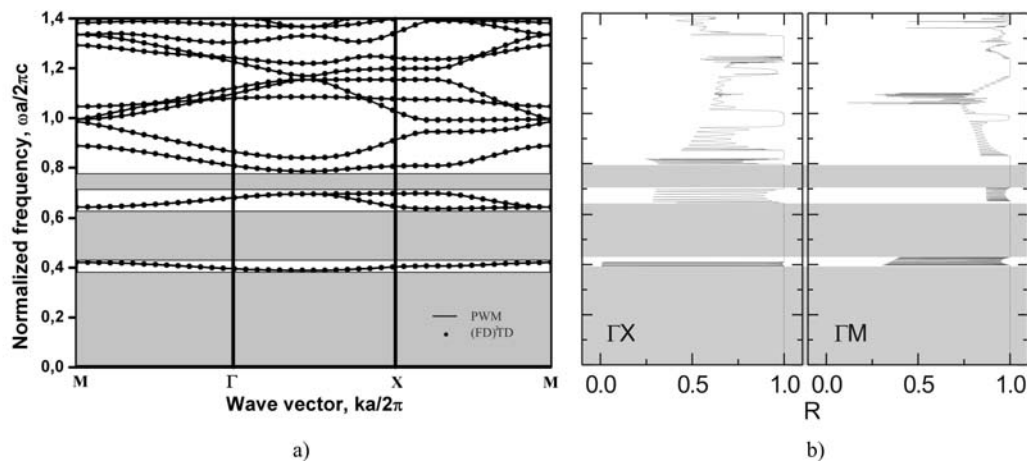
Figure 4.2. *a) Photonic band gap of metallic photonic crystal embedded in background with dielectric constant ε_b = 5. Ratio r/a = 0.472. The displacement of photonic bands is clearly observed. Reflectivity spectra for the same photonic crystal for b) Γ-X direction and c) Γ-M direction. Shaded areas represent photonic band gaps.*

eigenmodes at the Γ point changes when the background dielectric constant is increased. Figure 4.3 (a) and (b) show the modal electric field distribution (E_z) at the Γ point obtained using the PWM for the lowest five bands for ε_b = 1 and ε_b = 5, respectively. The maximum of each electric field is normalized to unity. For ε_b = 1, the first mode (Figure 4.3 (a), $\omega a/2\pi c$ = 0.75), which corresponds to the cut-off frequency. This mode is analogous to the dielectric mode in the dielectric photonic crystals because the electric field is concentrated in the dielectric region. The second mode (Figure 4.3 (a), $\omega a/2\pi c$ = 1.26) exhibits some amount of electric field within the metal region, in analogy to the air modes in dielectric photonic crystals. The third and fourth modes ($\omega a/2\pi c$ = 1.29) are degenerated and correspond to the distribution depicted in the third image of Figure 4.3 (a). We only show the field distribution for one of the modes, while the distribution for the other is the same but rotated by 90°. It is interesting to remark the difference

between these third and fourth modes and the other modes shown in Figure 4.3 (a). While the other modes show a four-fold symmetry with respect the two horizontal and vertical axes and the two diagonal axes, the third and fourth modes have only a two-fold symmetry with respect the diagonals. This difference, however, is compensated for by the fact that the two modes are degenerated at this point. Finally, the fourth image in Figure 4.3 (a) ($\omega a/2\pi c = 1.30$) corresponds to the fifth mode. The normalized frequencies corresponding to these modes are indicated together with the graphs. For $\varepsilon_b = 5$ (Figure 4.3 (b)) the same modes but with lower normalized frequencies can be observed. This decrease can be explained in terms of the variational principle: the increase of the background dielectric constant leads to a decrease of the frequency of the modes. This explains the shift of the bands toward the lower frequencies as well as the flattening of the bands. Furthermore, a change in the order of the modes can be realized: the fifth mode for $\varepsilon_b = 5$ ($\omega a/2\pi c = 0.84$) corresponds to the second mode for $\varepsilon_b = 1$ ($\omega a/2\pi c = 1.26$, 'air'-like mode), while the rest remain in the same order. This change in the order of the modes is produced by a smaller decrease of frequency for the 'air'-like mode. This effect can also be explained with the help of variational principle: since the electrical field is partially within the metal region, this mode is less sensitive to changes in the background dielectric constant. This smaller decrease in frequency for the 'air'-like mode makes possible the opening of the new band gap. Identifying the different modes with the five first bands in Figure 4.2 (a) it can be seen that the gap opens between the second and third (degenerated) bands ($\omega a/2\pi c = 0.69$) and the fourth band ($\omega a/2\pi c = 0.78$). For $\varepsilon_b = 1$ this new gap is not present because the band corresponding to the 'air'-like mode is in the region between the third, fourth and fifth bands, closing the gap.
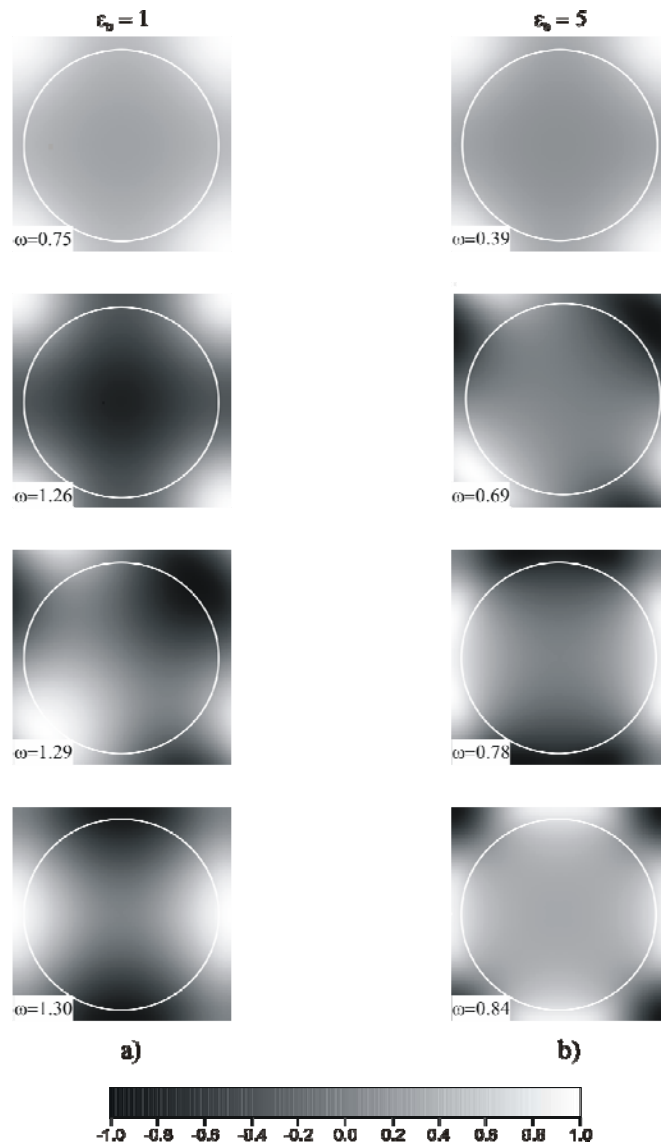
Figure 4.3. *Eigenmodes (at Γ point) of a square lattice of metallic circular cylinders for the lowest five photonic bands. The plotted field is E_z. The modes are labeled with the corresponding eigenfrequencies. a) Eigenmodes for $\varepsilon_b = 1$; b) Eigenmodes for $\varepsilon_b = 5$. The maximum of each electric field is normalized to unity.*
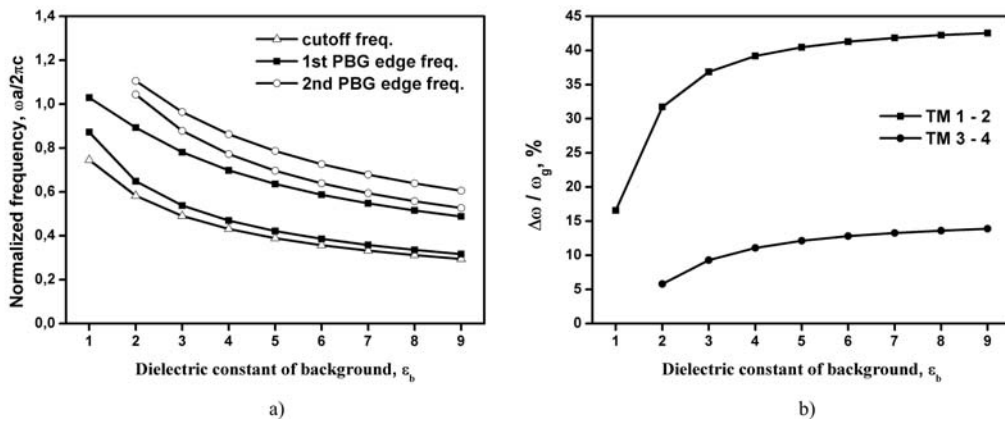
Figure 4.4. *a) Dependence of cutoff frequency, 1ˢᵗ, and 2ⁿᵈ PBG edge frequencies on the variation of dielectric constant of background. b) Dependence of 1ˢᵗ and 2ⁿᵈ PBG's on variation of dielectric constant of background.*

Figure 4.4 (a) shows the variation of the cut-off frequency and the PBG edge frequencies of the TM1-2 and TM3-4 band gaps as a function of the background dielectric constant. One can notice that the edge frequencies decrease with increasing background dielectric constant. The normalized frequency width of the gaps $\Delta\omega a/2\pi c$ tends to be a constant value as ε_b increases. For example, the TM1-2 gap for $\varepsilon_b = 3$, $\varepsilon_b = 6$ and $\varepsilon_b = 9$ is $\Delta\omega a/2\pi c = 0.24$, $\Delta\omega a/2\pi c = 0.20$ and $\Delta\omega a/2\pi c = 0.17$, respectively. Similarly, the TM3-4 gaps for the same ε_b are $\Delta\omega a/2\pi c = 0.09$, $\Delta\omega a/2\pi c = 0.09$ and $\Delta\omega a/2\pi c = 0.08$, respectively. The shrinking of the band structure with increasing background dielectric constant is clearly observed in this figure. The dependence of the relative band gap width $\Delta\omega/\omega_g$ on the background dielectric constant is shown in Figure 4.4 (b). The parameter ω_g denotes the frequency in the middle of the gap. We see that $\Delta\omega/\omega_g$ is increasing faster for smaller ε_b and tends to stabilize around $\Delta\omega/\omega_g \approx 42.3\%$ for TM1-2 and $\Delta\omega/\omega_g \approx 13.8\%$ for TM3-4 as $\varepsilon_b = 9$. This tendency can be explained from the

behavior of the bands seen in Figure 4.4 (a), where both $\Delta\omega$ and ω_g tend to a constant value.
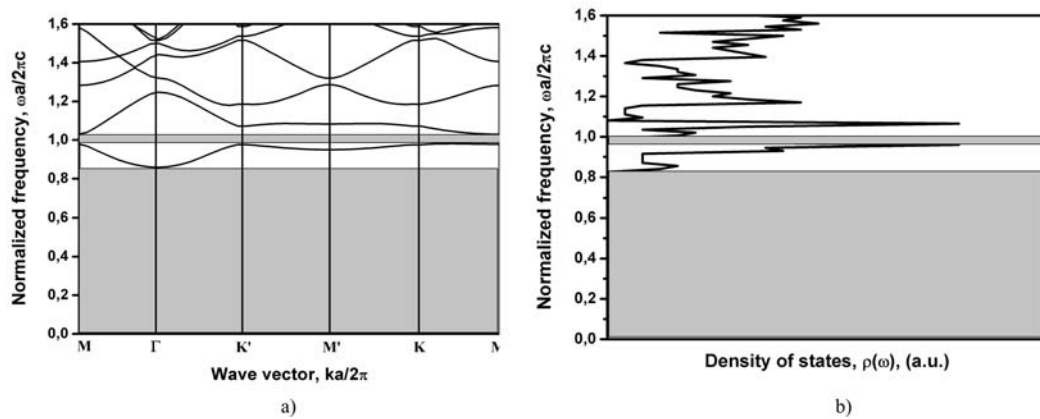
Triangular lattice

In all of our calculations the photonic crystal is composed of square metallic rods with side length d in a triangular lattice with lattice constant a. The structure under study is shown in the Figure 4.5 (a). Previous authors noted [30] that for the structure we are studying, 1/12 of the irreducible Brillouin zone is not sufficient to identify the absolute PBG because of the breakdown of the symmetry laws. For this reason we calculated the dispersion curves of the MDPCs along the M-Γ-K´-M´-K-M of the first Brillouin zone, as shown in the Figure 4.5 (b).

In a first step we have investigated the necessary conditions to have an absolute PBG (for all propagation directions and for TM polarization). After a series of band calculations for a wide range of filling fractions, we found that the dielectric constant of the background must be at least ε_b =1.6. This minimum value corresponds to a d/a=0.87 (the close-packed condition). For smaller filling fractions, the minimum necessary ε_b is even bigger. The band structure for d/a=0.87 is shown in Figure 4.6 (a). There are two band gaps – the large one
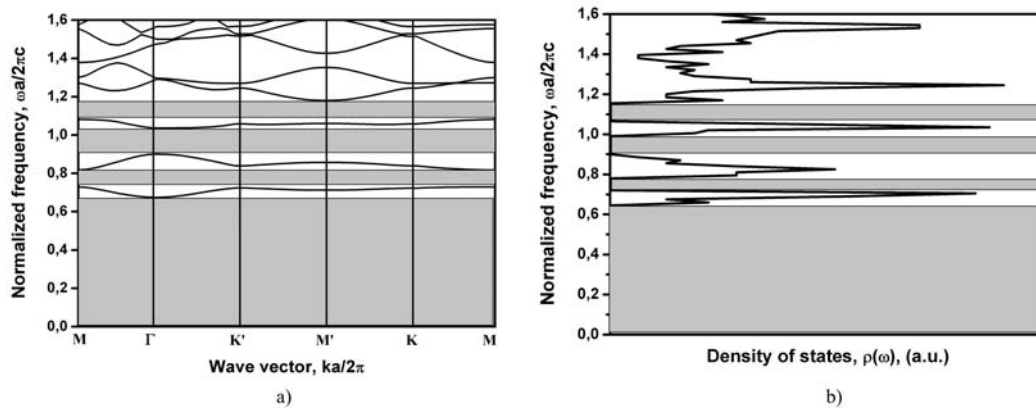

a)   b)
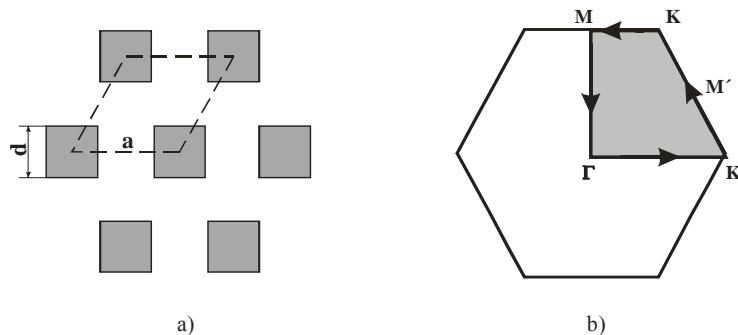
Figure 4.5. *a)structure under study; b) the first Brillouin zone.*

Figure 4.6. *Photonic band structure (a) and density of states (b) for a triangular lattice of metallic square rods in background with $\varepsilon_b = 1.6$. The ratio $d/a = 0.87$. Shaded areas represent photonic band gaps.*

between the zero frequency and the cutoff frequency defined by the first band (TM0-1) and a second one between the first and the second bands (TM1-2) with relative band gap width (the ratio of the band gap width to the mid gap frequency) $\Delta\omega/\omega_g.=4.58\%$. In Figure 4.6 (b) we show the density of states where the existence of the TM1-2 PBG can be observed as a frequency range with zero density of states.

In the next step, we extended our calculation to bigger ε_b. Figure 4.7 (a) shows the photonic band structure for $\varepsilon_b =4$. We see that increasing the dielectric constant of the background leads to changes in the photonic band structures. It is observed that $\Delta\omega/\omega_g$ of the TM1-2 PBG increases to 11% and that new PBGs appear between the second and third bands (TM2-3) and the third and fourth bands (TM3-4) with $\Delta\omega/\omega_g$ 13.8% and 9.5%, respectively. The existence of these gaps is confirmed in the density of states, as shown in Figure 4.7 (b). In addition, all the photonic bands shift towards lower frequencies and the bands become flatter.

Figure 4.7. *Photonic band structure (a) and density of states (b) for a triangular lattice of metallic square rods in background with dielectric $\varepsilon_b = 4$. The ratio $d/a = 0.87$. The appearance of new PBGs and the downshifting of the dispersion curves are observed. Shaded areas represent photonic band gaps.*

Figure 4.8 (a), (b), and (c) show the dependences of the relative band gap width ($\Delta\omega/\omega_g$) on the background dielectric constant for filling fractions 0.581, 0.72, and 0.866, respectively. It can be observed that the TM1-2 PBG does not appear for *f=0.58*. The $\Delta\omega/\omega_g$ are monotonically increasing with ε_b and tend to converge to an upper limit for higher values of ε_b. Furthermore, this upper limit is bigger for bigger filling fractions. It is worth noting that for bigger ε_b new PBGs appear at higher frequencies but their $\Delta\omega/\omega_g$ are too small to be considered in our investigation.
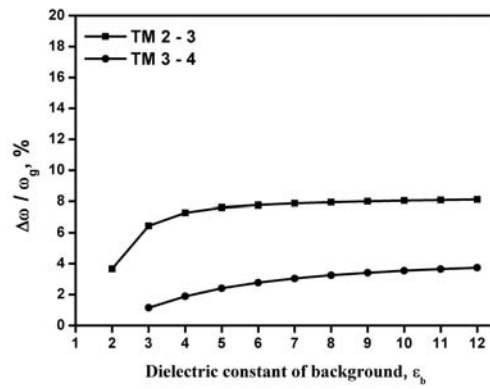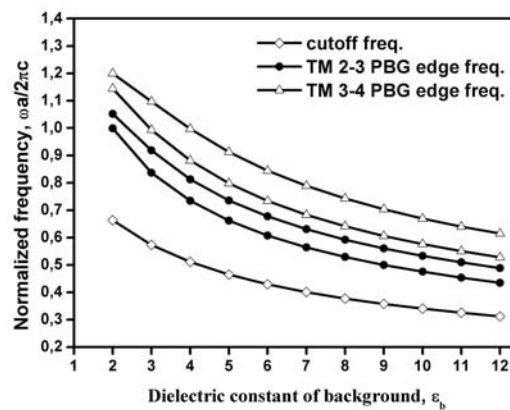
a)
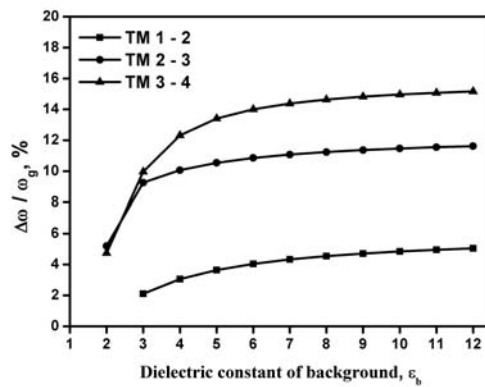
b)
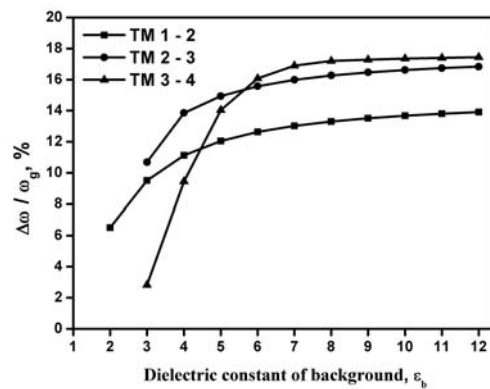
c)

Figure 4.8. *Relative size of the band gaps as a function of ε_b for filling factors 0.58 (a), 0.72 (b), and 0.87 (c)*

Figure 4.9. *Dependence of the cutoff frequency and of the TM2-3 and TM3-4 PBG edge frequencies as a function of ε_b. The filling factor is 0.72.*

Figure 4.9 shows the variation of the cutoff frequency and of the PBG edge frequencies of the TM2-3 and TM3-4 band gaps as a function of ε_b (for graphic clarity we do not include the results for the TM1-2 PBG in this figure, although they have the same behaviour as the depicted data) for d/a=0.79.

One can notice that the edge frequencies moves toward lower values with increasing background dielectric constant. The frequency width of the gaps $\Delta\omega$ tends to a constant value as ε_b increases. The shrinking of the band structure with increasing background dielectric constant is observed in this figure.

The dependence of the relative band gap width ($\Delta\omega/\omega_g$) on the filling fraction for ε_b =12 is plotted in Figure 4.10. It can be seen that $\Delta\omega/\omega_g$ is a monotonically increasing function of the filling fraction. It is interesting to note that the TM1-2 is the smaller band gap and that the relative width of the TM3-4 gap grows faster with the filling fraction than the relative width of the TM2-3 gap, and becomes the biggest at the close packed condition.
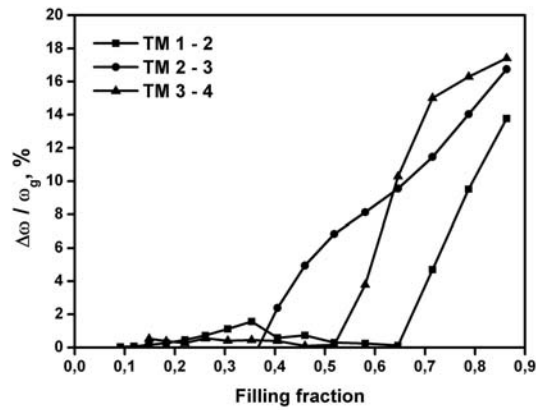
Figure 4.10. *Effect of the filling fraction on the relative width of the TM1-2, TM2-3 and TM3-4 band gaps at $\varepsilon_b=12$*

4.4 Conclusions

In conclusion, we have analyzed the effect of the variation of the background dielectric constant on the photonic band structure for a two-dimensional square lattice of circular metallic rods and triangular lattice wit square rods. The calculations are based on photonic band calculations using PWM and $(FD)^2TD$ methods and also on reflectivity spectra obtained with TMM. Increasing the background dielectric constant leads to the creation of a new gap, to the shift of the bands towards the low frequencies and to the flattening of the bands which means the reduction on the group velocity. We demonstrated that, for square lattice, increasing ε_b can be used to tailor the PBG frequencies to achieve a relative band gap as large as 42.3% for TM1-2 and 13.8% for TM3-4. By studying the field distributions of the first five bands at the Γ point and how they change with increasing background we have shown that the new band gap appears because some photonic bands have a larger shift to lower frequencies than others,

and this difference in the shift is explained by the different amount of electromagnetic energy within the metal region for the different bands.

We have shown that 2D metallodielectric photonic crystals consisting of a triangular lattice of square rods embedded into background materials with different dielectric constants can have absolute Photonic Band Gaps in TM polarization. We have found out that in order to have such a PBG the dielectric constant of the background must be at least 1.6. We have also shown that the PBG widths can be tuned by using background materials with different ε_b or by changing the filling fraction. In this way, relative band gaps larger than 10% can be achieved for filling fractions away from the close packed condition.

These results show that large relative band gap widths can be achieved by a careful selection of the background dielectric and of the metal composing the metallo-dielectric photonic crystal. Other works have suggested that the gaps can be enlarged or new gaps can be opened by using metallic rods with a geometry that breaks the crystal symmetry to obtain band splittings. Instead, in this work we propose another mechanism based on the increase of the background dielectric constant. Both mechanisms are complementary and could be used in conjunction to obtain photonic crystals with superior band gap widths.

References

[1] A. Moroz, "Three-Dimensional Complete Photonic-Band-gap Structures in the Visible", Phys. Rev. Lett. **83**, 5274 (1999)

[2] D. Sievenpiper, L. Zhang, R.F. Jimenez Broas, N.G. Alexopolous, and E. Yablonovitch, "High-impedance electromagnetic surfaces with a forbidden frequency band", IEEE Trans. Microwave Theory Tech. **47**, 2059 (1999)

[3] H.-Y. Sang, Z.-Y. Li, B.-Y- Gu, "Photonic states deep into the waveguide cutoff frequency of metallic mesh photonic crystal filters", Journal of Appl. Phys. **97**, 033102 (2005)

[4] J.-M. Lourtioz and A. De Lustrac, "Metallic photonic crystals", C.R. Physique **3**, 79 (2002).

[5] E. R. Brown and O.B. McMahon, "Large electromagnetic stop bands in metallodielectric photonic crystals", Appl. Phys. Lett. **67**, 2138 (1995)

[6] X. Zhang and Z.-Q. Zhang, "Creating a gap without symmetry breaking in two-dimensional photonic crystals", Phys. Rev. B **61**, 9847 (2000)

[7] A. Moroz, "Metallo-dielectric diamond and zinc-blende photonic crystals", Phys. Rev. B **66**, 115109 (2002)

[8] S. Gupta, G. Tuttle, M. Sigalas, K.-M. Ho, "Infrared filters using metallic photonic band gap structures on flexible substrates", Appl. Phys. Lett. **71**, 2412 (1997)

[9] J.A. Oswald, B.-I. Wu, K.A. McIntosh, L.J. Mahoney, and S. Verqhese, "Dual-band infrared metallodielectric photonic crystal filters", Appl. Phys. Lett. **77**, 2098 (2002)

[10] T. D. Drysdale, G. Mills, S. M. Ferguson, R.J. Blaikie, and D.R.S. Cumming, "Metallic tunable photonic crystal filter for terahertz frequencies", J. Vac. Sci. Technol. B **21**, 2878 (2003)

[11] F. Miyamaru, T. Kondo, T. Nagashima, and M. Hangyo, "Large polarization change in two-dimensional metallic photonic crystals in subterahertz region",

Appl. Phys. Lett. **82**, 2568 (2003)

[12] M. M. Sigalas, R. Biswas, K. M. Ho, C. M. Soukoulis, and D. D. Crouch, **"**Waveguides in three-dimensional metallic photonic band-gap materials**",** Phys. Rev. B **60**, 4426 (1999)

[13] J. Danglot, J. Carbonell, M. Fernandez, O. Vanbesien and D. Lippens, "Modal analysis of guiding structures patterned in a metallic photonic crystal", Appl. Phys. Lett. 73, 2712 (1998)

[14] J. Choi, G. Sauer, K. Nielsch, R.B. Wehrspohn, and U. Gösele, "Hexagonally Arranged Monodisperse Silver Nanowires with Adjustable Diameter and High Aspect Ratio", Chem. Mater. **15**, 776 (2003)

[15] K. Nielsch, R.B. Wehrspohn, S.F. Fischer, H. Kronmüller, J. Barthel, J. Kirschner, T. Schweinboeck, D. Weiss, and U. Gösele, "High Density Hexagonal Nickel Nanowire Arrays with 65 and 100 nm-Periods", MRS Symp. Proc. **705**, Y9.3.1 (2002)

[16] J. B. Pendry and A. MacKinnon, "Calculation of photon dispersion relations", Phys. Rev. Lett. **69**, 2772 (1992)

[17] V. Kuzmiak, A.A. Maradudin, and F. Pinsemin, "Photonic band structures of two-dimensional systems containing metallic components", Phys. Rev. B **50**, 16835 (1994)

[18] N.A. Nicorovici, R.C. McPhedran and L.C. Botten, "Photonic band gaps for arrays of perfectly conducting cylinders", Phys. Rev. E **52**, 1135 (1995).

[19] K. Sakoda, N. Kawai, T. Ito, A. Chutinan, S. Noda, T. Mitsuyu, and K. Hirao, "Photonic bands of metallic systems. I. Principle of calculation and accuracy", Phys. Rev. B **64**, 045116 (2001)

[20] E. Moreno, D. Erni, and C. Hafner, "Band structure computations of metallic photonic crystals with the multiple multipole method", Phys. Rev. B **65**, 155120 (2002)

[21] J. Arriaga, A. J. Ward and J. B. Pendry, "Order-N photonic band structures for metals and other dispersive materials", Phys. Rev. B **59**, 1874 (1999)

[22] O. Takayama and M. Cada, "Two-dimensional metallo-dielectric photonic crystals embedded in anodic porous alumina for optical wavelengths", Appl. Phys. Lett. **85**, 1311 (2004)

[23] A.L. Reynolds, Translight package, University of Glasgow (http://userweb.elec.gla. ac.uk/a/areynolds/).

[24] V. Kuzmiak, A.A. Maradudin, and F. Pinsemin, "Distribution of electromagnetic field and group velocities in two-dimensional periodic systems with dissipative metallic components", Phys. Rev. B **58**, 7230 (1998)

[25] Ch. Hafner, Cui Xudong and R. Vahldiek, "Metallic Photonic Crystals at Optical Frequencies", J. Comp. Theor. Nanosci. **2**, 240 (2005)

[26] K. Kunz and R. J. Luebbers, The Finite-Difference Time-Domain Method for Electromagnetics. Boca Raton, FL: CRC, 1993.

[27] A. Taflove, Susan Hagness Computational electrodynamics: The Finite-Difference Time-Domain Method, 2nd ed. Norwodd; MA: Artech House, 2000.

[28] K. Sakoda, Optical Properties of Photonic Crystals, Springer-Verlag, Berlin, 2001.

[29] N. Garcia, E. V. Ponizowskaya, Hao Zhu, John Q. Xiao, and A. Pons, "Wide photonic band gaps at the visible in metallic nanowire arrays embedded in a dielectric matrix", Appl. Phys. Lett. **82**, 3147 (2003)

[30] Noriko Kawai, Mitsuo Wada, and Kazuaki Sakoda, "Numerical Analysis of Localized Defect Modes in a Photonic Crystal: Two-Dimensional Triangular Lattice with Square Rods"Jpn. J. Appl. Phys. **37**, 4644 (1998)

Chapter 5

Influence of the Dielectric Background on the Quality Factors of Metallo-Dielectric Photonic Crystals

In this chapter the effect of varying the dielectric background on the quality factor of two-dimensional metallo-dielectric photonic crystals is theoretically studied. The studied metallo-dielectric photonic crystal consists of a square lattice of circular metallic rods embedded into a dielectric background with a defect rod on the center that creates resonant modes within the photonic band gap. The metal is modeled with the Drude dispersion relation. A combination of the finite-difference time-domain method together with a frequency filtering technique is used to estimate accurately the resonant frequencies and their quality factors. The results show that the quality factors increase with increasing background dielectric constant. If a dielectric

background material such as Silicon is used instead of air, an enhancement in the quality factor of up to 8 times can be achieved, depending on the resonant mode. We also show that, depending on the modes, there exists an optimal size for the defect rod that gives the maximum quality factor.

5.1 Introduction

Several studies on photonic crystals have shown that it is possible to create a localized electromagnetic mode (o group of modes) within the photonic band gap (PBG) by introducing a defect into the periodic structure [1]. A point defect behaves like a microcavity surrounded by reflecting walls and manifests an extremely sharp transmission peak in the photonic band gap. These structures have many potential applications such as optical filters [2], multiplexers [3], resonators with high quality factors [4] and low-threshold lasers [5]. A critical issue for developing of these applications is to obtain high quality factors (Q). The quality factor of a cavity is a measure of the energy loss per cycle versus the energy stored. Until now, most of the papers dealing with quality factors consider dielectric photonic crystals. Recently, there is a great interest in metallic and metallo-dielectric photonic crystals because of the high negative dielectric constants in the optical frequencies (forbidden PBG starting from zero frequency)[6], the possibility of wide PBG with small number of periods (more compact photonic integrated structures) [7-14] and the device based on the metallo-dielectric photonic crystals can be fabricated with low cost technologies. Another interesting property is that changing the dielectric constant of the background leads to creating new and wider band gaps [15,16]. In this context, a

few papers ware devoted to the study of quality factors of metallo-dielectric photonic crystal (MDPC) [17-20] and to our knowledge the effect of dielectric background in the quality effect for metallo-dielectric photonic crystals has not been yet studied.

In this chapter we present the influence of the variation of the background dielectric constant on the quality factors of metallo-dielectric photonic crystal. The combination of the finite-difference time-domain (FDTD) [21] method with a signal processing technique is used to accurately calculate the resonant frequencies and quality factors. We will also investigate the dependence of the resonant frequencies and of the quality factors with the defect radius.

In Section 5.2 we describe the structure under study and introduce the numerical method for the determination of the resonant modes. The method for evaluating the quality factor is discussed in detail. Then in section 5.3, we investigate and analyze the resonant frequencies and quality factors of the structure and their dependence with the background dielectric constant and defect size. Finally, in section 5.4 we briefly sum up our results and conclusions.

5.2 Method and Computational Model

We used the FDTD method combined with the auxiliary differential equations (ADE-FDTD) [19]. All FDTD simulations were done using a spatial grid resolution 40x40 points per unit cell, with $1 \cdot 10^5$ iterations to achieve convergence. PML boundary conditions [22] with 15 computational cells on all sides were used to absorb the outgoing waves.

Quality factor

Figure 5.1 (a) depicts the structure under study: the photonic crystal is composed of circular metallic rods in a square lattice with lattice constant a embedded in a
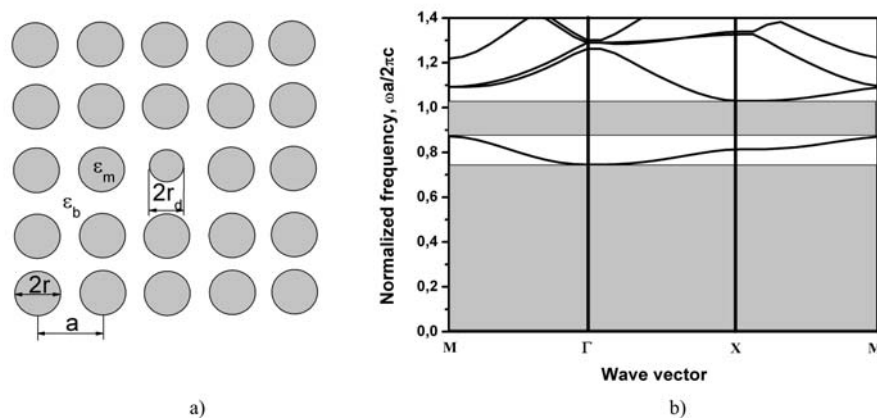
Figure 5.1. *a) The structure under study. The ε_m and ε_b are dielectric constants of metal and background, respectively. The center rod forms a defect with radius r_d. b) Photonic band diagram for TM polarization of metallo-dielectric photonic crystal with air background ($\varepsilon_b = 1$). Shaded area represents photonic band gap.*

dielectric background. The radius r of the rods is taken as $r = 0.472a$, which corresponds to a filling fraction of 70%. We have chosen this radius because this structure shows the two largest photonic band gaps (PBG) for TM polarization when the background is air. The simulation area consists of 5x5 metallic rods and the radius of the central rod r_d was varied from $0.05a$ to $0.4a$. We assume that the dielectric constant of the metallic rods can be described by the Drude model. In the simulation, ω_p has been fixed to $\omega_p a / 2\pi c = 1.0$ and $\gamma = 10^{-4} \omega_p$. It must be noted that the considered damping constant is kept deliberately small because, although other works [23, 24] have shown that quality factors are limited by losses, we focus on the background dielectric constant influence and thus, the study of the dependence on the losses is out of scope of this paper. The dispersion

Chapter 5

diagram of the photonic band structure for TM mode when $\varepsilon_b = 1$ is plotted in Figure 5.1(b).

The background dielectric constant ε_b was varied to simulate the use of different host materials from 1 (air) to 12 (silicon) and was taken as frequency-independent as a first approximation. We have done this because although it is known that the dielectric constants of the possible materials suitable as background are not frequency-independent, in the range of frequencies of practical interest the dielectric constant variation is reasonably small.

To obtain the resonant frequencies and quality factors (Q factors) of the defective photonic crystals, the structure under study is excited by a point pulse source placed in an asymmetric position. This permits to obtain all the resonant modes independently of their symmetry. The wavefront is a Gaussian modulated with a sinus function. The pulse is centered at a frequency $\omega a/2\pi c = 0.7$ and broad enough to cover the entire PBGs for the range of ε_b considered in this paper. The transmission spectrum of the photonic crystal is obtained as the ratio between the output and the input spectral intensities.

Once the resonant peaks are identified in the transmission spectrum and the resonant frequencies are estimated, there are several ways to compute the corresponding Q factors. The simplest method consists in calculating the ratio between the resonant frequency ω_0 and the full-width at half maximum (FWHM) $\Delta\omega$ of the intensity spectrum:

$$Q = \frac{\omega_0}{\Delta\omega}. \tag{5.1}$$

Quality factor
_____

However, this method leads to larger uncertainties when Q is high [1]. The second method consists of measuring the rate of exponential decay of the field amplitude at the resonant frequency for the given defect mode:

$$Q = -\left[\frac{\omega_0(N_1 - N_0)\Delta t}{2\ln E_1/E_0}\right], \qquad (5.2)$$

where ω_0 is the resonant frequency, Δt is the FDTD timestep, E_1 and E_0 are the amplitudes at the time steps N_1 and N_0, respectively [24].

We follow the second method combined with a signal processing technique to improve accuracy. First, we calculate the transmission spectrum of MDPC structure, and then we apply a narrow bandwidth Butterworth filter of the third order [25] centered at the resonant frequency to obtain the time-dependent field component corresponding only to the defect mode. To this end, the frequency range of the filter was chosen to cover only the frequency range of the defect mode. The resulting time-dependent field evolution shows an exponential decay of its amplitude. The logarithm of this amplitude is fitted to a straight line with slope m. With this, the Q factor can be calculated from the following expression:

$$Q = -\frac{\omega_0\Delta t}{2m}, \qquad (5.3)$$

where ω_0 is the resonant frequency, and Δt is the FDTD timestep.

5.3 Results and Discussion

Figures 5.2(a) and 5.2(b) show the calculated transmission spectra when $\varepsilon_b=1$ and $\varepsilon_b=9$ respectively for the ideal structure (without defect) and for two defects radiuses $r_d=0.2a$ and $r_d=0.3a$. The transmission peaks in the acoustic (first) and second PBGs corresponding to the resonant frequencies of the modes associated to the defects can be observed. For $\varepsilon_b =1$ (Figure 5.2(a)) when $r_d=0.2a$ the transmission spectrum contains four resonant modes: two in the acoustic bandgap A(1) and E(1) similar to those found in the [26] and two modes E(3) and B in the second bandgap. Their corresponding resonant frequencies are detailed in Table 5.1. Instead, for $r_d=0.3a$, up to six resonant modes can be observed: the same modes A(1), E(1), E(3) and B can be recognized but in addition, two modes can also be observed designated as A(2) and E(3). From Figure 5.2b we can see that for $\varepsilon_b=9$ the same corresponding modes can also be identified.
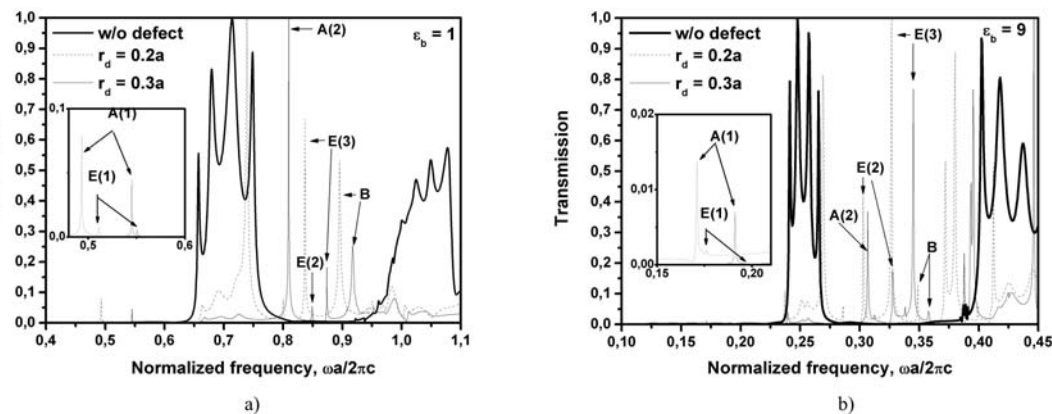
Figure 5.2. *Transmission spectrum of metallo-dielectric photonic crystal with defect rods of different radius and embedded into background: a) when $\varepsilon_b = 1$. b) when $\varepsilon_b = 9$. The numbers mark resonant frequencies under study. The insets show frequency region where acoustic modes appear.*

Table 5.1: Resonant frequencies for the modes observed in Figures 5.2(a) and 5.2(b).

| Mode designation | Normalized Frequency ($\omega a/2\pi c$) | | | |
| | $\varepsilon_b=1$ | | $\varepsilon_b=9$ | |
	$r_d=0.2a$	$r_d=0.3a$	$r_d=0.2a$	$r_d=0.3a$
A(1)	0.493	0.545	0.171	0.191
E(1)	0.511	0.551	0.176	0.192
A(2)	-	0.809	-	0.289
E(2)	-	0.849	0.303	0.328
E(3)	0.837	0.874	0.327	0.345
B	0.895	0.918	0.349	0.358

By comparing Figures 5.2(a) and 5.2(b) we can see that both the PBG frequencies and the resonant frequencies shift to lower values with increasing background dielectric constant while the relative band gap width increases, in agreement with [15, 16].

In order to recognize the corresponding modes at the different ε_b and defect radius, and to designate the modes we have studied the symmetry of the electric field profile distribution around the defect rod. Figure 5.3 shows the electric field profiles for the six modes recognizable for $\varepsilon_b=1$ and $r_d=0.3a$. The maximum of each electric field is normalized to unity. The modes are designated according to their symmetry in the C_{4v} point group, as it is done in other works such as Ref. [27]. The number in the parentheses are given in the order of increasing resonant frequency, for the modes of the same symmetry. Thus, the A modes correspond to
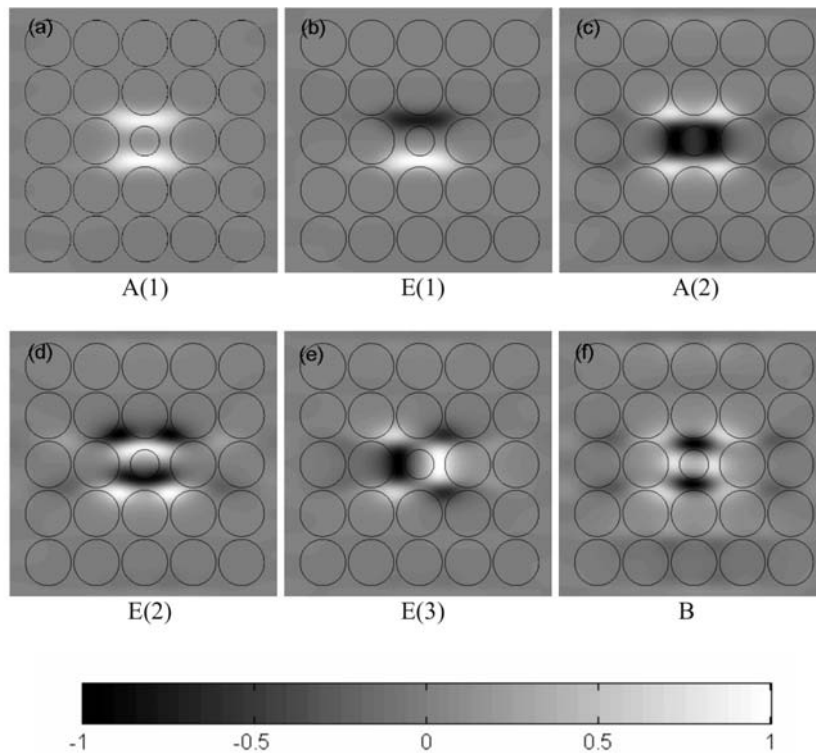
Figure 5.3. *Electric field profiles for the defect modes of the studied structure for $\varepsilon_b=1$ and $r_d=0.3a$. The maximum of each electric field is normalized to unity. The E-modes are doubly degenerated and only one of the profiles is shown, while the other is the equivalent rotated $90°$.*

monopoles, the E modes to dipoles and the B mode is a quadrupole. It has to be noted that the E modes are degenerated, however here only one of them is depicted, while the other would be equivalent but rotated 90º.

In order to confirm the tendency of the PBG frequencies and of the resonant frequencies to decrease observed in Figure 5.2, Figure 5.4 shows the behavior of the PBG edges and of the resonant frequencies of modes A(1), E(1), E(3) and B as a function of the background dielectric constant for $r_d=0.2a$. It is also worth noting that the resonant frequencies approach the lower PBG edge frequencies (dielectric-like band) for bigger ε_b.
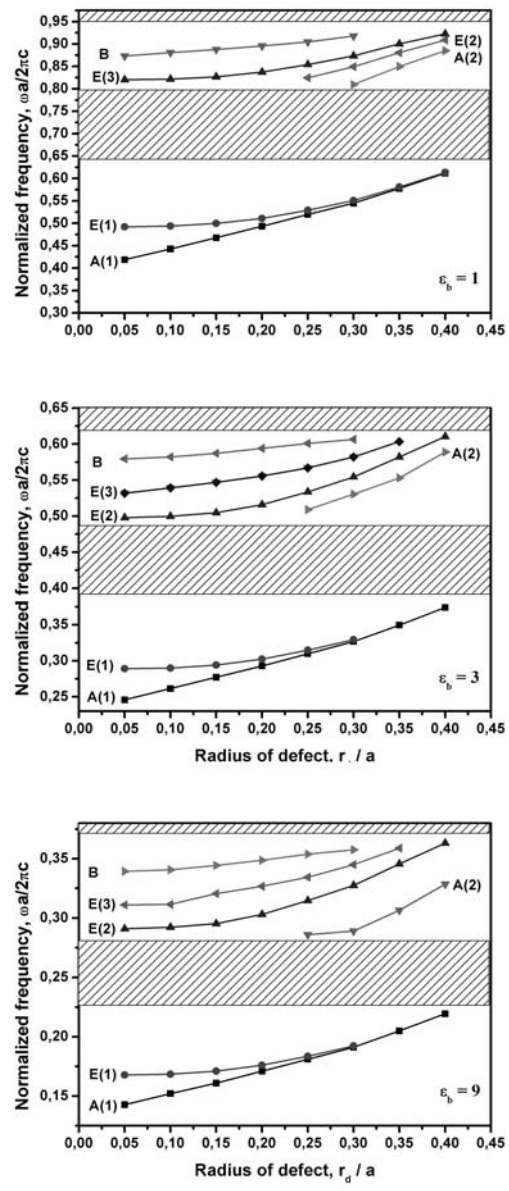
Quality factor
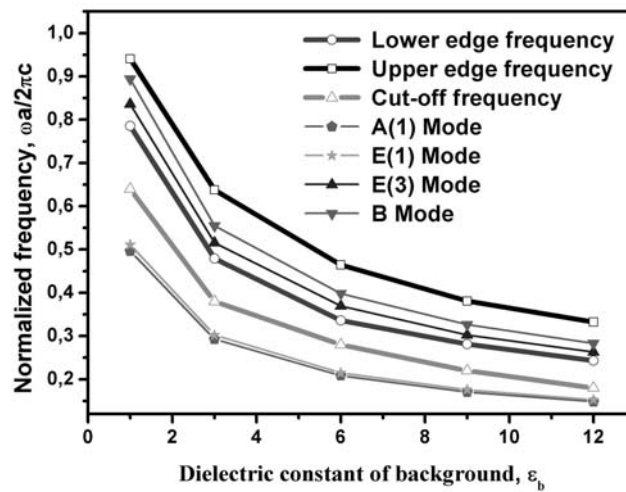
Figure 5.4. *Plot of the edge frequencies of PBG and resonant frequencies as a function of dielectric constant of background ε_b when $r_d = 0.2a$.*

Figure 5.5 shows the dependence of the resonant frequencies with the defect radius r_d for $\varepsilon_b = 1$, $\varepsilon_b = 3$, and $\varepsilon_b = 9$. A general trend of the resonant frequency of all the modes to increase with increasing defect radius can be observed. Furthermore, as a consequence of the shrinking of the band diagram of the photonic crystal with increasing ε_b, the frequency differences between the three modes for a given ε_b also decrease with increasing ε_b. Nevertheless, the relative position between the modes and the range of r_d where the modes exist within the PBG are independent of the background dielectric constant. This can be explained on the basis of the field profile distributions of the modes. Since the resonant frequency depends on the complexity of the field profile (e.g.: the number of nodes) and this is independent of the background dielectric constant and of the defect radius, their relative positions are also independent of these parameters.

Figure 5.5. The dependence of the resonant frequencies as a function of defect radius r_d for three different dielectric constants of background ε_b. Note different range of frequencies.
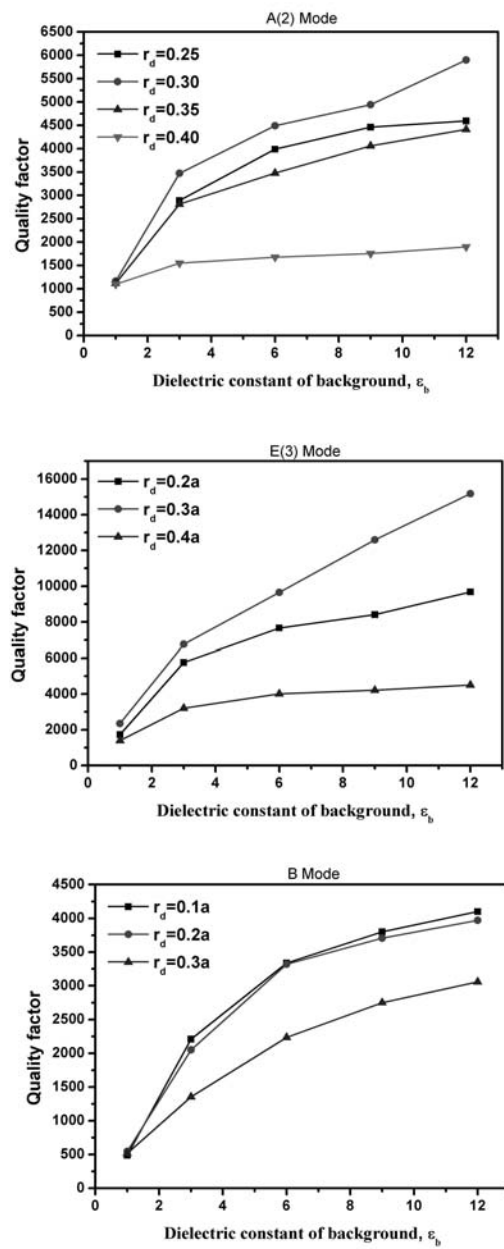
Quality factor

The modes in the acoustic PBG, A(1) and E(1), exist for all the range of considered r_d, and for increasing defect radius, their resonant frequencies converge. This can also be explained on the view of the field profile: as it can be seen in Figure 3, the field profiles of the modes A(1) and E(1) are very similar except for the relative phase between the two lobes. The resonant frequency depends on the absolute value of the field but not on their relative phase. For increasing defect radius, the absolute value of the field profile of the two modes become more similar, leading to the observed convergence. The modes in the second bandgap, A(2), E(2), E(3) and B exist within a limited range of r_d, and they disappear as their corresponding resonant frequency penetrates in the allowed band. In the following we will see how the Q factors of the defect resonant frequencies depend on the radius of defect and on the background dielectric constant. Figure 5.6 shows the dependence of the calculated Q factors for different defect radius with the background dielectric constant and for the modes A(2), E(3), and B. It can be observed that the Q factors increase with increasing background dielectric constant, with a bigger increase rate until $\varepsilon_b=6$ and then tending to stabilize for bigger ε_b. For instance, for the mode E(3) at $\varepsilon_b =12$, the Q factors reach 9680, 15180 and 4500 for $r_d =0.20a$, $r_d=0.30a$, $r_d=0.40a$, respectively. This increase in the Q factor is very similar to the increase in relative PBG width reported in [15, 16]. It is also worth noting that the Q factors for $\varepsilon_b =1$ for the modes E(3) and B are nearly of the same magnitude and are practically independent of the defect radius r_d. For example, for mode E(3), the Q factors are 1724, 2348, 1398 for $r_d=0.20a$, $r_d=0.30a$, $r_d=0.40a$, respectively. Mode B shows a behavior similar to mode E(3) with the difference that the bigger Q corresponds to the defect radius $r_d=0.10a$. For the mode A(2), the dependence with ε_b is similar with a maximum attained Q of 5900.

Figure 5.6. *The quality factor as a function of dielectric constant of background ε_b for different radiuses of defect rods for A(2) Mode, E(3) Mode and B Mode.*

Quality factor

Figure 5.7 shows the calculated Q factors as a function of r_d for different background dielectric constants. From this figure it can be observed that for mode E(3) the Q factors show a maximum for a given r_d and that this maximum is higher for bigger ε_b. Instead, the behavior for mode B is quite different: the Q factors maintain nearly constant values in the radius range $0.0 \leq r_d \leq 0.2a$ and then slowly decrease, with a bigger decrease rate for bigger ε_b. Finally, the behavior for mode A(2) is very similar to mode E(3) with a maximum of Q at r_d=0.30a, except for ε_b =1 where maximum appears at r_d=0.30a.

5.4 Conclusions

We have studied the influence of the background dielectric constant on the resonant frequencies and quality factors of two-dimensional metallo-dielectric photonic crystals with defect sites. We have also analyzed the dependence of these resonant frequencies and Q factors with the defect radius.

We have found that, as it happens with the Photonic Band Gap edge frequencies, the resonant frequencies shift to lower values with increasing background dielectric constant, and that the relative position of the resonant frequencies within the PBG is not affected by the change in the host material.

We have seen that, in general, the Q factor increases with increasing background dielectric constant, and that Q values as large as 15180, 4027, and 5900, for the modes E(3), B, and A(2) respectively can be achieved. Thus, high Q values can be obtained using host materials with bigger ε_b.
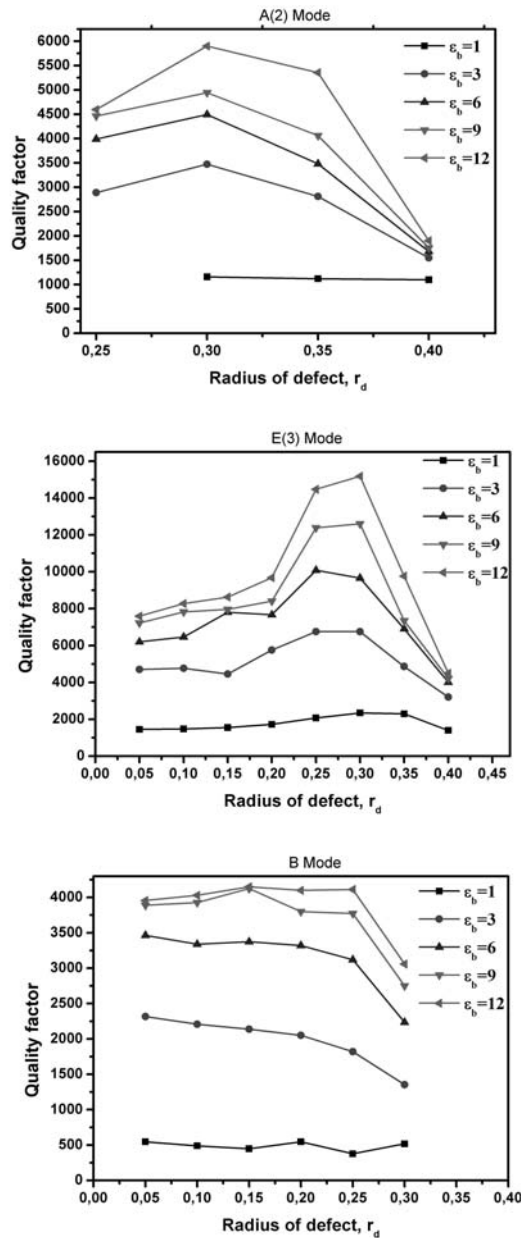
Figure 5.7. *The quality factor as a function of defect radius r_d different dielectric constant of background for A(2) Mode, E(3) Mode and B Mode.*

Quality factor

We have also found that the quality factor can be tuned also by changing the defect radius, although the behavior of the Q with r_d is different for the different modes considered. For the mode E(3), a maximum can be observed at a given r_d, and the maximum is more evident for bigger ε_b. Instead, for the mode B, the Q shows practically constant values for all the range of r_d, with a decrease at large r_d, more marked for the big ε_b. Finally, for the mode A(2) a maximum can also be identified within the range of r_d considered, although for air background the behavior is quite different: the Q increases linearly with r_d.

We have shown that high Q factors can be obtained by using resonant structures based on metallo-dielectric photonic crystals with a defect on one of the lattice positions. This opens a wide field of application, since the Q factors demonstrated in this work can be further enlarged by the consideration of more complex defects, as other authors have proposed for all-dielectric photonic crystals. One possibility would be considering two defects at two neighbor lattice points, and adequately shifting the defects from the lattice point.

References

[1] P.R. Villeneuve, S. Fan, and J.D. Joannopoulos, "Microcavities in photonic crystals: Mode symmetry, tunability, and coupling efficiency", Phys. Rev. B **54**, 7837 (1996)

[2] Z. Xu, J. Wang, Q. He, L. Cao, P. Su, and G. Jin, "Optical filter based on contra-directional waveguide coupling in a 2D photonic crystal with square lattice of dielectric rods", Opt. Express **13**, 5608 (2005)

[3] M. Koshiba, "Wavelength division multiplexing and demultiplexing with photonic crystal waveguide couplers", J. Lightwave Technol., vol. **19**, pp. 1970 (2001)

[4] Y. Akahane, T. Asano, B. -S. Song, and S. Noda, "Fine-tuned high-Q photonic-crystal nanocavity", Opt. Express **13**, 1202 (2005)

[5] M. Loncar, T. Yoshie, A. Scherer, P. Gogna, and Y. Qiu, "Low-threshold photonic crystal laser", Appl. Phys. Lett. **81**, 2680 (2002)

[6] V. Kuzmiak, A.A. Maradudin, and F. Pinsemin, "Photonic band structures of two-dimensional systems containing metallic components", Phys. Rev. B **50**, 16835 (1994)

[7] C. Xudong, C. Hafner, and R. Vahldieck, "Design of ultra-compact metallo-dielectric photonic crystal filters", Opt. Express **13**, 6175 (2005)

[8] J.A. Oswald, B.-I. Wu, K.A. McIntosh, L.J. Mahoney, and S. Verqhese, "Dual-band infrared metallodielectric photonic crystal filters", Appl. Phys. Lett. **77**, 2098 (2002)

[9] T. D. Drysdale, G. Mills, S. M. Ferguson, R.J. Blaikie, and D.R.S. Cumming, "Metallic tunable photonic crystal filter for terahertz frequencies", J. Vac. Sci. Technol. B **21**, 2878 (2003)

[10] F. Miyamaru, T. Kondo, T. Nagashima, and M. Hangyo, "Large polarization change in two-dimensional metallic photonic crystals in subterahertz region", Appl. Phys. Lett. **82**, 2568 (2003)

[11] M. M. Sigalas, R. Biswas, K. M. Ho, C. M. Soukoulis, and D. D. Crouch, "Waveguides in three-dimensional metallic photonic band-gap materials", Phys. Rev. B **60**, 4426 (1999)

[12] J. Danglot, J. Carbonell, M. Fernandez, O. Vanbesien, and D. Lippens, "Modal analysis of guiding structures patterned in a metallic photonic crystal", Appl. Phys. Lett. **73**, 2712 (1998)

[13] V. F. Rodríguez-Esquerre, M. Koshiba, H. E. Hernández-Figeroa, and C. E. Rubio-Mercedes, "Power splitters for waveguides composed by ultralow refractive index metallic nanostructures", Appl. Phys. Lett. **87**, 091101 (2005)

[14] N. J. Florous, K. Saitoh, and M. Koshiba, "Three-color photonic crystal demultiplexer based on ultralow-refractive-index metamaterial technology", Opt. Lett. **30**, 2736 (2005)

[15] M. A. Ustyantsev, L. F. Marsal, J. Ferré-Borrull, and J. Pallarès, "Effect of the dielectric background on dispersion characteristics of metallo-dielectric photonic crystals", Opt. Commun. **260**, 583 (2006)

[16] H. van der Lem and A. Moroz, "Towards two-dimensional complete photonic bandgap structures below infrared wavelengths", J. Opt. A: Pure Appl. Opt. **2**, 395 (2000)

[17] E. Ozbay, B. Temelkuran, M. Sigalas, G. Tuttle, C.M. Soukoulis, and K. M. Ho, "Defect structures in metallic photonic crystals", Appl. Phys. Lett. **69**, 3797 (1996)

[18] F. Gadot, A. de Lustrac, J. -M. Lourtioz, T. Brillat, A. Ammouche, E. Akmansoy, "High-transmission defect modes in two-dimensional metallic photonic crystals", J. Appl. Phys. **85**, 8499 (1999)

[19] T. Ochiai and J. Sánchez-Dehesa, "Localized defect modes in finite metallic two-dimensional photonic crystals", Phys. Rev. B **65**, 245111 (2001)

135

[20] O. Takayama and M. Cada, "Two-dimensional metallo-dielectric photonic crystals embedded in anodic porous alumina for optical wavelengths", Appl. Phys. Lett. **85**, 1311 (2004)

[21] A. Taflove Computational electrodynamics: The Finite-Difference Time-Domain Method, 3rd ed. Norwodd; MA: Artech House, 2005.

[22] J.A. Roden, and S.D. Gedney, "Convolution PML (CPML): An efficient FDTD implementation of the CFS-PML for arbitrary media", Microw. Opt. Technol. Lett. **27**, 334 (2000)

[23] T. Ueta, K. Ohtaka, N. Hawai, and K. Sakoda, "Limits on quality factors of localized defect modes in photonic crystals due to dielectric loss", J. Appl. Phys. **84**, 6299 (1998)

[24] S. Foteinopoulou, C.M. Soukoulis, "Theoretical investigation of one-dimensional cavities in two-dimensional photonic crystals", IEEE J. Quantum Electron. **38**, 844 (2002)

[25] W.M. Robertson, G. Arjavalingam, R.D. Meade, K.D. Brommer, A.M. Rappe, and J.D. Joanopoulos, "Measurement of photonic band structure in a two-dimensional periodic dielectric array", Phys. Rev. Lett. **68**, 2023 (1992)

[26] S. Guo and S. Albin, "Numerical techniques for excitation and analysis of defect modes in photonic crystals", Opt. Express **11**, 1080 (2003)

Quality factor

Chapter 6

Losses Influence on the Quality Factors of Silver Metallo-Dielectric Photonic Crystals

In chapter 5 the influence of the dielectric background on quality factors of metallo-dielectric photonic crystals has been studied by FDTD method. The metal was treated as a Drude lossless model and the plasma frequency was chosen arbitrary. However, in order to model the realistic metals, the plasma frequency and the damping constant, that is responsible for losses, must be taken into account, especially at optical frequencies.

In this chapter we model silver metallo-dielectric photonic crystal at optical frequencies by the FDTD method. The Drude model with parameters fit to empirical data was used. The results show that the primary factor of the quality factors degradation are due to the losses introduced by metals at the optical frequencies.

6.1 Theoretical methods

It is a known fact that the Drude model in the form $\varepsilon(\omega) = \varepsilon_\infty - \omega_p^2/(\omega^2 + i\omega\Gamma)$ when $\varepsilon_\infty = 1$ does not provide an accurate representation of the experimental dielectric constant data for silver over a wide frequency range [1]. However, we can determine, from Drude model, what ε_∞, ω_p, and Γ fit better the experimental dielectric constant data for a specific frequency range.

In order to determine the best set of parameters we define the objective function Φ as in [2]:

$$\Phi = \sum_{\omega_j} \text{Re}\left[\varepsilon_{\exp}(\omega_j) - \varepsilon_D(\omega_j)\right]^2 + \text{Im}\left[\varepsilon_{\exp}(\omega_j) - \varepsilon_D(\omega_j)\right]^2 , \qquad (6.1)$$

where ω_j are discrete values of the frequency $\omega = 2\pi/\lambda$ for which permittivity is calculated, $\varepsilon_{\exp}$ are the experimental values taken from Palik et al. [3], and ε_D stands for permittivity of the Drude model. The minimization of objective function Φ is performed by using the simulated annealing method [4], and with controlling parameters introduced by Corana et al. [5]. Following this procedure we tried to fit the Drude model for the range between 300 nm and 900 nm.

Figure 6.1 shows the real and imaginary part of experimental values of silver and fitted Drude model with parameters $\varepsilon_\infty = 3.7$, $\omega_p = 1.35 \cdot 10^{16}$ rad/sec, and $\Gamma, = 27.13 \cdot 10^{12}$ rad/sec. We see that these parameters adequately fit experimental results for the optical range from ultraviolet to midinfrared. Moreover these

parameters are in good agreement with parameters reported earlier in the literature [6-8].
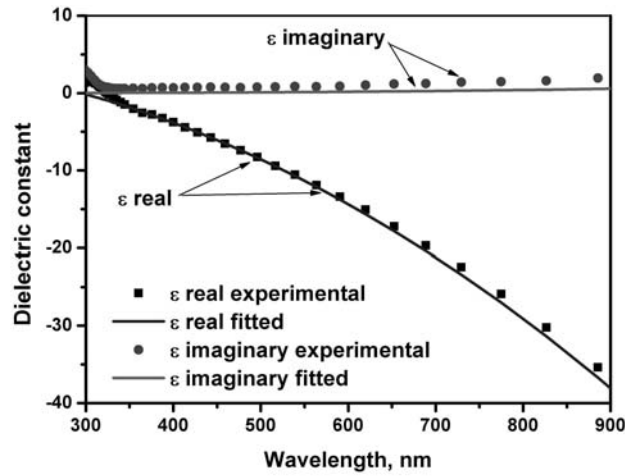
Figure 6.1. *Fitting the real (ε_r) and imaginary (ε_i) parts of the dielectric function of Drude mode for silver to experimental data [3]. Fitted silver parameters: $\varepsilon_\infty = 3.7$, $\omega_p = 1.35$ x 10^{16} rad/sec, and $\Gamma = 27.13$ x 10^{12} rad/sec.*

Figure 6.2 depicts the structure under study: the silver metallo-dielectric photonic crystal is composed of 5x5 circular metallic rods with radius $r = 142$ nm in a square lattice with lattice constant $a = 300$ nm embedded into background with dielectric constant ε_b. The metallic rods are described by the Drude model. The background dielectric constant was varied from 1 to 5. These values were chosen in order to keep our results of the calculations of the defect modes in the range between 300 nm and 900 nm, since, as was shown in chapter 5, the frequencies are downshifted with increasing ε_b. The defect was formed by varying the radius of the center rod r_d from $0.0a$ to $0.4a$
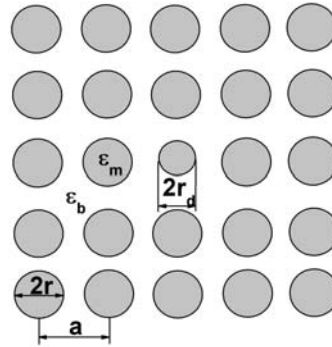
Figure 6.2. *The structure under study. The ε_m and ε_b are dielectric constants of metal and background, respectively. The defect is formed by changing the radius of the center rod r_d.*

As a computational tool, we used the FDTD method combined with the auxiliary differential equations (ADE-FDTD) [9], described in detail in chapter 3. All FDTD simulations were done using a spatial grid resolution 40x40 points per unit cell, with 2^{16} iterations to achieve convergence. The temporal step size Δt is chosen to satisfy the Courant stability condition $\Delta t = 1/\sqrt{c\left(\Delta x^{-2} + \Delta y^{-2}\right)}$. Here c is the light velocity in vacuum, and Δx and Δy are the spatial steps along x and y directions, respectively. The convolution perfectly matched layers (CPML) boundary conditions [10] with 15 cells on all sides were used to absorb the outgoing waves. Moreover, the CPML were placed one lattice constant apart from the photonic crystal in order to minimize the influence of the reflected waves. The structure under study is excited by an initial field distribution similar to that used in the Ref. [11]. The transmission spectrum of the photonic crystal is obtained as the ratio between the output and the input spectral intensities. The field distributions of the defect modes are obtained by a Fourier transform of transient fields. The method to calculate the quality factors is the same as was used in chapter 5.

6.2 Results and Discussion

Figure 6.3 shows the calculated transmission spectra for silver metallo-dielectric photonic crystal when $\varepsilon_b=1$ and for defect structure with $r_d = 0.0a$. We can see the four resonant modes appear when the defect is present. Two modes are in the acoustic gap (TM 0-1) and two defect modes are in the first band gap (TM 1-2). These modes are monopole, dipole, 2nd order monopole and quadrupole. The corresponding field distributions for these modes are shown in the Figure 6.4. In terms of the symmetry group the monopole mode corresponds to A(1) mode, the dipole is E(1) mode, the 2nd order monopole is A(2) mode and quadrupole is E(2) mode.
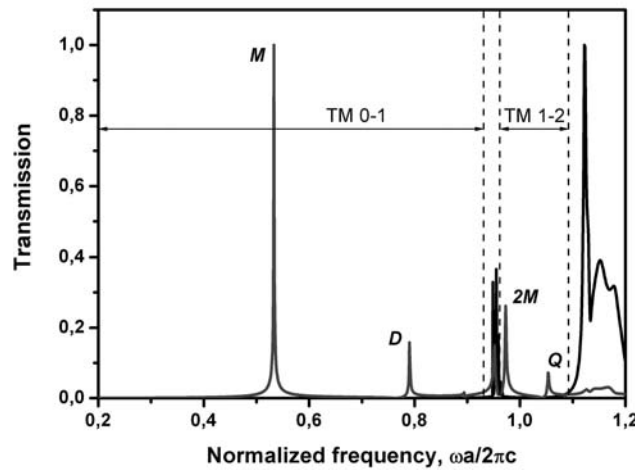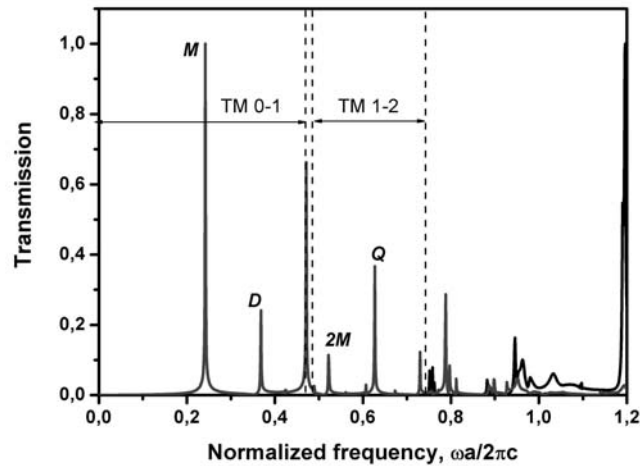

Figure 6.3. Transmission spectrum of silver metallo-dielectric photonic crystal with $\varepsilon_b = 1$ and defect $r_d = 0.0a$. The letters show the defect modes: M-monopole, D-dipole, 2M-2nd order monopole and Q-quadrupole. The vertical dashed lines mark edges of photonic band gaps.
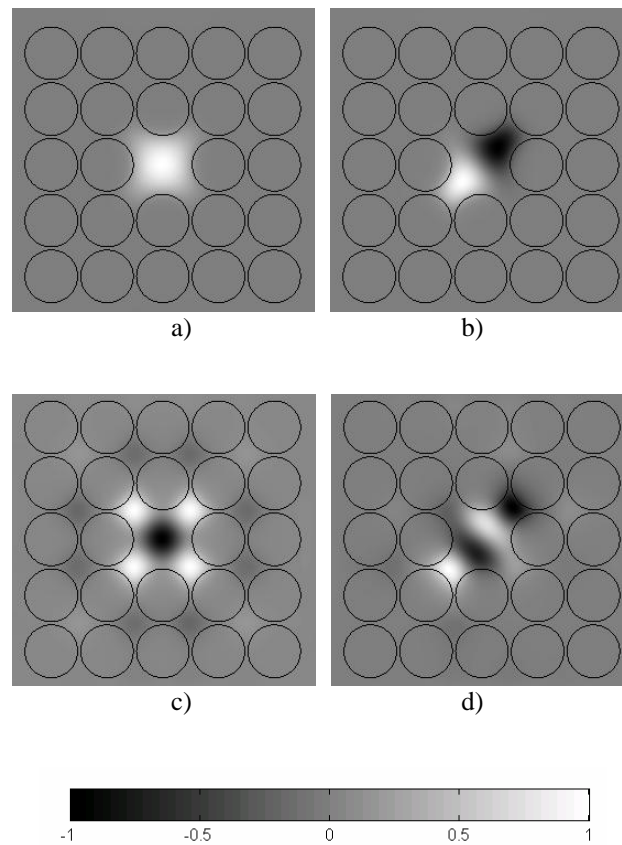
Figure 6.4. *Electric field profiles for the defect modes of the studied structure for $\varepsilon_b=1$ and $r_d=0.0a$. The maximum of each electric field is normalized to unity. a)monopole mode; b)dipole mode; c) 2nd order monopole mode; d) quadrupole mode.*

As was shown previously [12, 13] increasing ε_b leads to shifting frequencies to lower values and to creating new gaps. Figure 6.5 shows the calculated transmission spectra for $\varepsilon_b=5$ and $r_d = 0.0a$. We see that transmission spectra together with defect modes are redshifted. Also, the new band gap between 0.76 and 0.94 (in the units of $\omega a/2\pi c$) appears. Moreover, due to defect introduced into the photonic crystal, we can see two resonance modes at 0.79 and

0.8 (in the units of $\omega a/2\pi c$). But to make comparative study we will take into account only the modes corresponding to that when $\varepsilon_b=1$.


Figure 6.5. *Transmission spectrum of silver metallo-dielectric photonic crystal with* ε_b = 5 *and defect* r_d = 0.0a. *The letters correspond to that of Figure 6.3.*

In Figure 6.6 (a) and (b) we show the dependence of the resonant frequencies with the defect radius r_d for ε_b =1, and ε_b =5. A general trend of the resonant frequency of all the modes to increase with increasing defect radius can be observed. Furthermore, as a consequence of the shrinking of the band diagram of the photonic crystal with increasing ε_b, the frequency differences between the modes for a given ε_b also decrease with increasing ε_b.

The monopole and dipole modes in the TM 0-1 gap and 2nd order monopole mode in the TM 1-2 gap exist for all range of r_d while the quadrupole mode exists only for r_d from 0.0a to 0.3a.
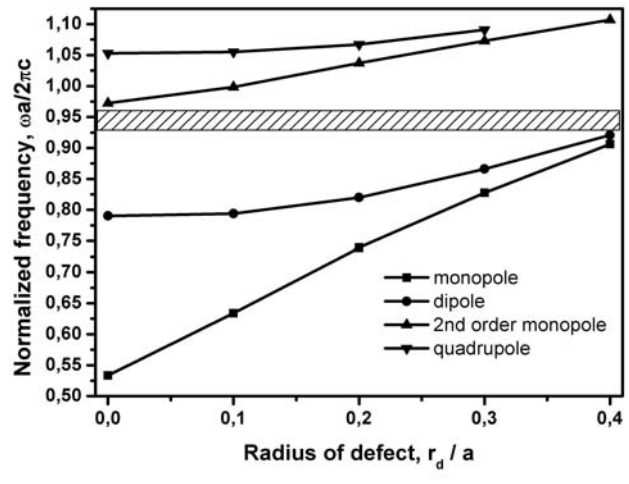
a)
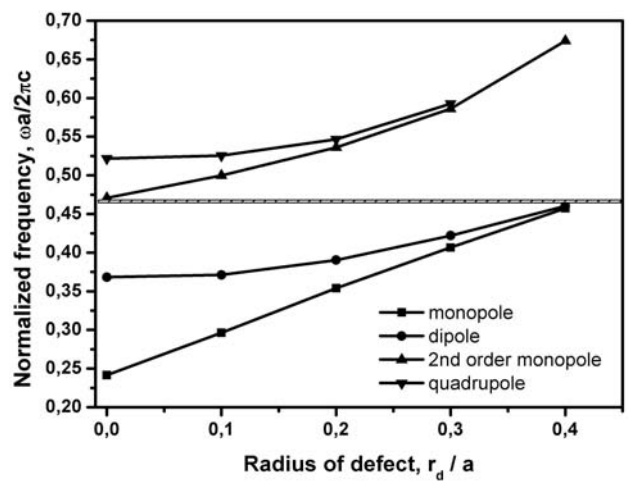
b)

Figure 6.6. *Plot of the resonance frequencies of defect mode for different ε_b as a function of radius of defect r_d. a) $\varepsilon_b = 1$; b) $\varepsilon_b = 5$. The hatched areas represent the boundaries of the photonic band gaps.*

In the following we will see how the quality factors are affected by varying the the ε_b. In Figure 6.7 we show the quality factors as a function of the ε_b. From this figure three different cases can be observed. The quality factors of monopole

mode monotonically decrease with increasing ε_b while the quality factors of dipole mode have higher values at $\varepsilon_b = 2$ and the quality factors of 2nd order monopole and of the quadrupole reach their maximum at $\varepsilon_b = 3$. Moreover, for dipole mode the quality factors are rapidly decrease when $\varepsilon_b = 2$ while the quality factors of 2nd order monopole and of the quadrupole decay more slowly.

a)   b)

c)   d)
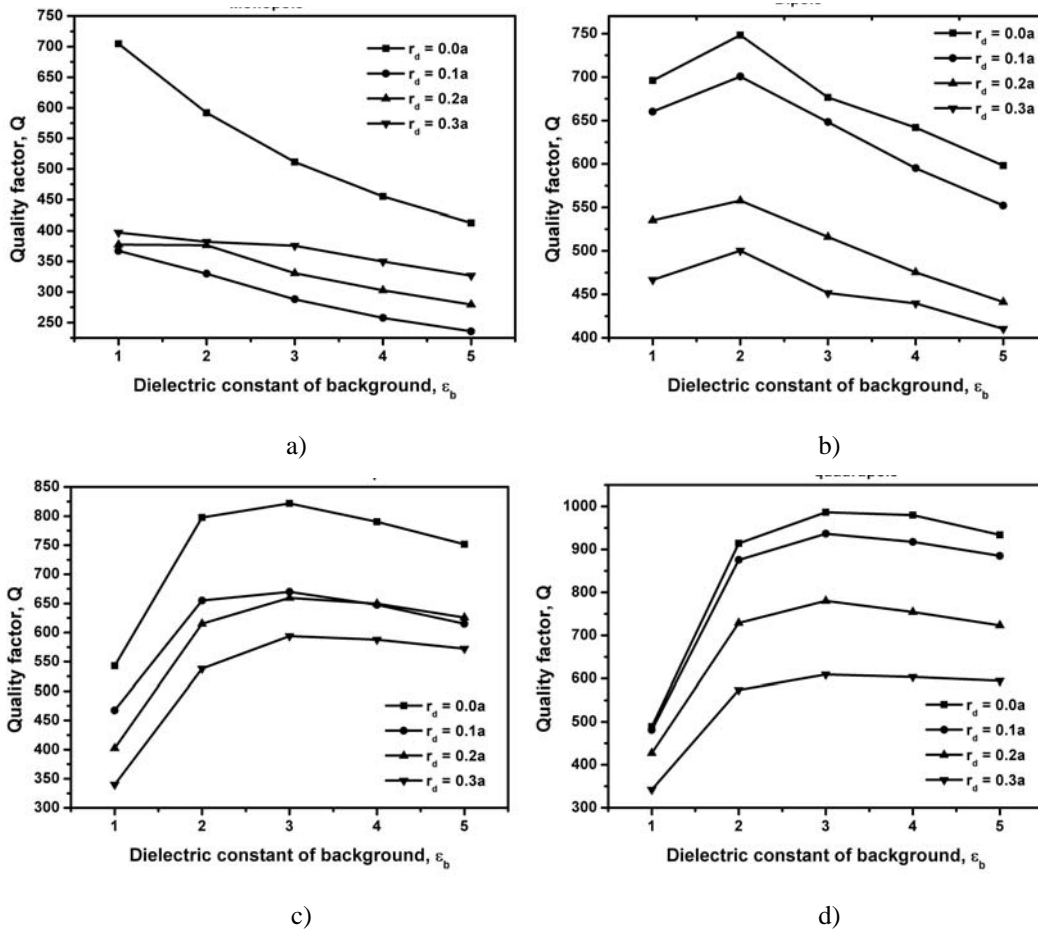
Figure 6.7. *The quality factor as a function of dielectric constant of background ε_b for different radiuses of defect. a) monopole; b) dipole; c) 2nd order monopole; d) quadrupole.*

Furthermore, the highest values of the quality factors are obtained for cavity defect, irrespectively of the mode.

In order to clarify the influence of losses we calculated the quality factors for different damping constants Γ.
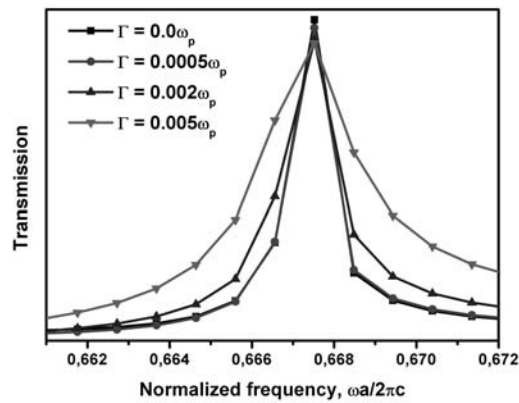
a)
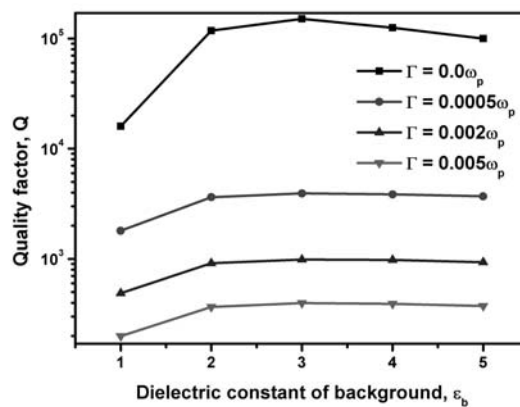
b)

Figure 6.8. a)Transmission for quadrupole mode as a function of Γ for $\varepsilon_b=3$ and $r_d =0.0a$. b)The quality factors of quadrupole mode as a function of dielectric constant of background ε_b for different Γ with $r_d =0.0a$.

It was shown in [14] that quality factors are strongly depended on full width at half maximum (FWHM). To illustrate this in Figure 6.8 (a), we plot the transmission of quadrupole mode for different Γ. We can see that the spectral position of defect mode is not affected by the Γ, only the spectral width is increased with increasing the Γ. If we use the definition of the quality factor in form $Q = \dfrac{\omega_d}{\Delta\omega}$ then it is clear that bigger $\Delta\omega$ will lead to smaller quality factors. The quality factors as function of the dielectric constants of background for different cases of Γ are shown in Figure 6.8 (b). We can see from this figure that the quality factors are greatly affected by Γ. In Figure 6.9 we plot the quality factors as function of Γ for quadrupole mode for $r_d = 0.0a$ and $r_d = 0.3a$ with $\varepsilon_b = 3$.
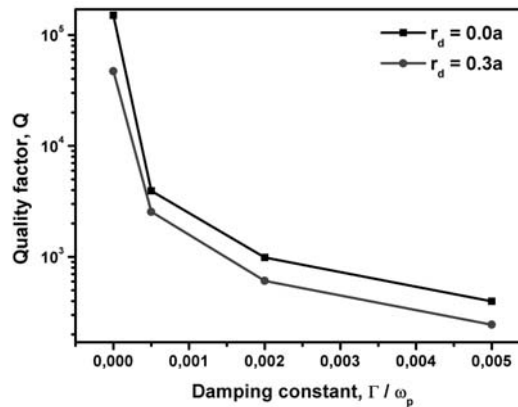

Figure 6.9. *The quality factors as a function of Γ/ω_p for two different radiuses at $\varepsilon_b=3$.*

6.3 Conclusions

We have studied the influence of the background dielectric constant on the resonant frequencies and quality factors of two-dimensional silver metallo-dielectric photonic crystals cavity. We used fitted parameters of Drude model to

adequately describe the frequency-dependent dielectric constant of silver from 300 nm to 900 nm.

We have shown that the quality factors of different modes of silver metallo-dielectric photonic crystals behave different. The quality factors of monopole mode are monotonically decreasing function of the ε_b. However, the quality factors of dipole reach their maximum for $\varepsilon_b = 2$, and for the 2nd order monopole and quadrupole the maximum quality factors found for $\varepsilon_b = 3$. Further increasing of dielectric constant of background leads to decreasing in the quality factors. Also, we have shown how the quality factors are affected by losses introduced by metals at optical frequencies.

References

[1] A. D. Rakic, A. B. Djurisic, J. M. Elazar, and M. L. Majewski, "Optical Properties of Metallic Films for Vertical-Cavity Optoelectronic Devices", Appl. Opt. **37**, 5271-5283 (1998)

[2] A. Vial et al., "Improved analytical fit of gold dispersion: Application to the modeling of extinction spectra with a finite-difference time-domain method", Phys. Rev. B **71**, 085416, (2005)

[3] E.D. Palik, *Handbook of Optical Constants of Solids* (Academic Orlando, Fla., 1985)

[4] S. Kirpatrick, C.D. Gelatt, M.P. Vecchi, "Optimization by simulated annealing", Science, **220**, 671 (1983)

[5] A. Corana, M. Marchesi, C. Martini, and S. Ridella, "Minimizing multimodal functions of continuous variables with the simulated annealing algorithm", ACM Trans. on Math. Software, vol. **13**, p. 262 (1987)

[6] S.K. Gray, and T. Kupka, "Propagation of light in metallic nanowire arrays: Finite-difference time-domain study of silver cylinders", Phys. Rev. B. **68**, 045415 (2003)

[7] N.J. Florous, K. Saitoh, and M. Koshiba, "Theoretical investigation of photonic crystal waveguide splitters incorporating ultralow refractive index metallic nanowires", IEEE Photonics Technol. Lett. **17**, 2313 (2005)

[8] W. Saj, "FDTD simulations of 2D Plasmon waveguide on silver nanorods in hexagonal lattice", Opt. Express **13**, 4818 (2005)

[9] A. Taflove Computational electrodynamics: The Finite-Difference Time-Domain Method, 3rd ed. Norwodd; MA: Artech House, 2005.

[10] J.A. Roden, and S.D. Gedney, "Convolution PML (CPML): An efficient FDTD implementation of the CFS-PML for arbitrary media", Microw. Opt. Technol. Lett. **27**, 334 (2000)

[11] M. Qiu and S. He, "Numerical method for computing defect modes in the two-dimensional photonic crystals with dielectric or metallic inclusions", Phys. Rev. B. **61**, 12871 (2000)

[12] M. A. Ustyantsev, L. F. Marsal, J. Ferré-Borrull, and J. Pallarès, "Effect of the dielectric background on dispersion characteristics of metallo-dielectric photonic crystals", Opt. Commun. **260**, 583 (2006)

[13] H. van der Lem and A. Moroz, "Towards two-dimensional complete photonic bandgap structures below infrared wavelengths", J. Opt. A: Pure Appl. Opt. **2**, 395 (2000)

[14] T. Ueta, K. Ohtaka, N. Hawai, and K. Sakoda, "Limits on quality factors of localized defect modes in photonic crystals due to the dielectric loss", J. Appl. Phys **84**, 6289 (1998)

Chapter 7

Summary and conclusions

The work presented in this dissertation has dealt with the following subjects:

- development of the PWEM and FDTD-based numerical approaches for analysing dispersion characteristics of metallo-dielectric photonic crystals;

- analysis of the influence of dielectric background on photonic band gaps and quality factors of two-dimensional metallo-dielectric structures;

- analysis of the influence of dielectric background on quality factor when real parameters of metals are considered.

Since, dispersion characteristics of photonic crystals are of great importance, the main attention has been paid to the numerical methods of analysis For this purpose, a modification of plan-wave expansion and finite-difference

time-domain methods have been developed. The basics of the developed approach have been outlined in Chapter 3.

In Chapter 4, the modified method has been verified and used to calculate dispersion characteristics of metallo-dielectric photonic crystals as a function of dielectric constant of background. The investigation of these structures has allowed to gain understanding of how the optical properties of such structures can be modified and how one can make use of it in designing optical devices.

In what follows, in Chapter 5, an influence of dielectric constant of background on quality factors of metallo-dielectric photonic crystals has been presented and analysed. In particular, an enhancement of quality factors has been achieved when silicon was used as a template.

Chapter 6 shows how the quality factors are affected when the parameters of real metal are taken into account. It was shown that absorption is the critical parameter that limits the quality factor in metallo-dielectric photonic crystals.

Future work

There are many possibilities for the future work to extend results presented in this thesis. Some of them are outlined below.

As was demonstrated in chapter 4 the changing of dielectric background leads to the increasing of the existing band gaps and creation of new one. As we know the refractive index of nonlinear materials depends on the intensity of the input signal. It will be possible to use these nonlinear materials as the background media for metallo-dielectric photonic crystals. In this way the size, creation and position of the photonic band gaps can be controlled in dynamical fashion.

The other prominent area of metallic nanoparticles is the using surface plasmon-polaritons to enhance electromagnetic fields at metal-dielectric interfaces and to guide light in subdiffraction length scale.

The major drawback of metals is their losses, especially at optical frequencies. It would be possible to use dielectrics with gain to compensate the loss of the metal. To study the physics of problem mentioned above the tools for the analysis must be developed. In particular, the FDTD code developed in chapter 3 can be modified to include models of gain dielectrics and/or nonlinear models.

Regarding to the devices based on photonic crystals the optimal design of geometry can be obtained through combination of numerical method (such as FDTD and PWEM) with one of the optimization techniques (such as simulated annealing or genetic algorithms).

Publications related to the thesis

Referred journals:

1. Band structure calculation in two-dimensional Kerr-nonlinear photonic crystals
I.S. Maksymov, L.F. Marsal, M.A. Ustyantsev, J. Pallares
Optics Communications, Volume 248, Issues 4-6, 15 April 2005, Pages 469-477

2. Effect of the dielectric background on dispersion characteristics of metallo-dielectric photonic crystals
M.A. Ustyantsev, L.F. Marsal, J. Ferre-Borrull, J. Pallares,
Optics Communications, Volume 260, Issue 2, 16 April 2006, Pages 583-587

3. Influence of the dielectric background on the quality factors of metallo-dielectric photonic crystals
M.A. Ustyantsev, L.F. Marsal, J.Ferre-Borrull, J. Pallares (submitted to Optics Communications)

Conferences:

1. Influence of the background dielectric constant on the band structure of metallo-dielectric photonic crystals
M.A. Ustyantsev, L.F. Marsal, J. Ferre-Borrull, J. Pallares
Electron Devices, 2005 Spanish Conference on 2-4 Feb., 2005 Page(s):311 – 314

2. Photonic Band Gaps in Metallo-Dielectric Photonic Crystals with Real Metals in a Porous Silicon Matrix
M.A. Ustyantsev, L.F. Marsal, J. Ferre-Borrull, J. Pallares
Workshop on Nanoelectronics and Photonics Systems, 27-28 June**,** 2005, pp. 71-74

3. Investigation of photonic band gaps in triangular lattices of metallic square rods in dielectric background
M.A. Ustyantsev, L.F. Marsal, J. Ferre-Borrull, J. Pallares
Transparent Optical Networks, 2005, Proceedings of 2005 7th International Conference Volume 2, 3-7 July 2005 Page(s):315 - 318 Vol. 2

4. Numerical analysis of absorptive two-dimensional metallo-dielectric photonic crystal
J. Ferre-Borrull, L.F. Marsal, M.A Ustyantsev, J. Pallares
Proceedings of SPIE - Volume 5840, Photonic Materials, Devices, and Applications, July 2005, pp. 44-53

5. **Effect of the Dielectric Background on the Quality Factors of Silver Metallo-Dielectric Photonic Crystals**
M.A. Ustyantsev, L.F. Marsal, J.Ferre-Borrull, J. Pallares
Electron Devices, 2007 Spanish Conference

157